MODELLING OF SURFACE MORPHOLOGIES IN DISORDERED ORGANIC SEMICONDUCTORS USING FRACTAL METHODS

KONG YEO LEE

THESIS SUBMITTED IN FULFILMENT OF THE
REQUIREMENTS FOR THE DEGREE OF
DOCTOR OF PHILOSOPHY

FACULTY OF SCIENCE
UNIVERSITY OF MALAYA
KUALA LUMPUR

2017

University of Malaya

UNIVERSITY OF MALAYA
ORIGINAL LITERARY WORK DECLARATION

Name of Candidate: **KONG YEO LEE** (I.C/Passport No:)

Registration/Matric No: **SHC110063**

Name of Degree: **DOCTOR OF PHILOSOPHY (EXCEPT MATHEMATICS & SCIENCE PHILOSOPHY)**

Title of Project Paper/Research Report/Dissertation/Thesis ("this Work"):

MODELLING OF SURFACE MORPHOLOGIES IN DISORDERED ORGANIC SEMICONDUCTORS USING FRACTAL METHODS

Field of Study: **PHYSICS**

I do solemnly and sincerely declare that:

(1) I am the sole author/writer of this Work;
(2) This Work is original;
(3) Any use of any work in which copyright exists was done by way of fair dealing and for permitted purposes and any excerpt or extract from, or reference to or reproduction of any copyright work has been disclosed expressly and sufficiently and the title of the Work and its authorship have been acknowledged in this Work;
(4) I do not have any actual knowledge nor do I ought reasonably to know that the making of this work constitutes an infringement of any copyright work;
(5) I hereby assign all and every rights in the copyright to this Work to the University of Malaya ("UM"), who henceforth shall be owner of the copyright in this Work and that any reproduction or use in any form or by any means whatsoever is prohibited without the written consent of UM having been first had and obtained;
(6) I am fully aware that if in the course of making this Work I have infringed any copyright whether intentionally or otherwise, I may be subject to legal action or any other action as may be determined by UM.

University of Malaya

Candidate's Signature Date:

Subscribed and solemnly declared before,

Witness's Signature Date:

Name: **PROF. DR. SITHI VINAYAKAM MUNIANDY**

Designation: **PROFESSOR**

ABSTRACT

Organic semiconductor structures have been studied extensively mainly in attempts to improve charge transfer rate at the organic thin film interfaces. Enhancement on carriers transport and performance, integration of heterostructures and composite materials, and improving life-span of the devices are among the major focuses. Surface morphologies are often investigated to characterize various interface processes including charge transfer and surface contact between layers in thin films. The total effective interface area and root mean square (rms) of surface height fluctuations are among the common parameters that often used to corroborate device performance upon modifying surface properties. In this study, three different but complementary approaches are used to characterize geometrical features of microstructure morphologies in disordered organic nickel tetrasulfonated phthalocyanine (NiTsPc) films, namely the power spectral density analysis, variogram method based on generalized Cauchy process model and grayscale fractal box counting approach. The objectives of this research work are (i) to investigate geometrical features of microstructure morphologies in disordered organics solar cell by using fractal methods, (ii) to relate fractal parameters with carrier transport properties, and (iii) to study and quantify device performance based on microstructure morphological features. It is shown that each of these approaches offers certain perspective about the complex morphologies often found in disordered thin films and thus joint interpretations of these approaches offer better characterizations of the surface properties, filling the gap left by others. The morphologies are also interpreted in the context of percolation network supported by the photocurrent density measurements. Higher electric conductivity is observed for thin films with higher fractal dimension but also enhanced when there exists spatially correlated morphologies in the form of network and this has enhanced charge transport at interfaces.

University of Malaya

ABSTRAK

Struktur semikonduktor organik telah dikaji secara meluas dalam usaha meningkatkan kadar pemindahan cas pada peringkat antaramuka filem nipis organik. Kajian untuk mempertingkatkan angkutan cas dan prestasi, integrasi heterostruktur dan bahan-bahan komposit, dan memanjangkan jangka hayat peranti adalah antara fokus utama. Morfologi permukaan sering digunakan untuk mencirikan pelbagai proses yang berlaku antaramuka termasuk pemindahan cas dan luas permukaan yang berhubung antara lapisan filem nipis. Perkiraan jumlah keluasan berkesan antara muka dan punca purata kuasa dua yang menganggarkan fluktuasi ketinggian permukaan adalah antara parameter yang sering digunakan untuk menyokong prestasi peranti apabila mengubahsuai sifat-sifat permukaannya. Dalam kajian ini, tiga kaedah yang berbeza tetapi saling melengkapi telah digunakan untuk geometri morfologi mikrostruktur bagi filem organik nikel phthalocyanine tetrasulfonated (NiTsPc) yang bercelaru, iaitu analisis ketumpatan spektrum kuasa (KSK), kaedah variogram berdasarkan model proses Cauchy teritlak (PCT) dan pembilangan kotak fraktal skala kelabu. Objektif kajian ini adalah untuk (i) menyiasat ciri-ciri geometri morfologi mikrostruktur dalam sel solar organik yang bercelaru dengan menggunakan kaedah fraktal, (ii) mengaitkan parameter fraktal dengan ciri angkutan pembawa, dan (iii) mengkaji dan mengukur prestasi peranti berdasarkan morfologi yang berstruktur mikro. Keputusan analisis telah menunjukkan bahawa setiap kaedah ini menawarkan perspektif tertentu tentang morfologi kompleks yang sering dijumpai dalam filem nipis bercelaru dan tafsiran bersama itu menawarkan pencirian sifat permukaan yang lebih baik dan memenuhi ruang yang tertinggal. Pengaliran cas yang lebih tinggi telah ditemui bagi filem nipis yang berdimensi fraktal lebih tinggi tetapi juga ditingkatkan apabila wujudnya morfologi terkolerasi sebahagian dalam bentuk rangkaian dan ini telah meningkatkan pengaliran cas di muka perantaraan.

University of Malaya

ACKNOWLEDGEMENT

First and above all, I thank God Almighty for granting me health and wisdom to complete this research successfully.

I would like to express my sincere gratitude to my research supervisor, Prof. Dr. Sithi Vinayakam Muniandy, for providing me support, valuable advice, insightful comments and guidance throughout this study. His vision and enthusiasm for science had inspired me and it was my privilege and honor to work under his supervision. I am grateful to my co-supervisor, Associate Prof. Dr. Khaulah @ Che Som Binti Sulaiman, for her advices, encouragement and valuable experience on the material preparation for this study. I thank Mr. Muhamad Saipul Fakir for his technical assistance on the laboratory work and AFM images preparation, and also his kind answers to my general questions during our discussions. I also appreciate the financial support from Malaysia Ministry of Higher Education for funding three years of MyBrain scholarship for my PhD study.

Last but not least, I would like to thank my late grandfather who first taught me writing, back to my kindergarten time. I thank my parents, husband and daughters for their love and understanding for supporting me spiritually throughout the writing of this thesis and research publications.

University of Malaya

TABLE OF CONTENTS

CHAPTER 1: INTRODUCTION

CHAPTER 2: MATERIAL SURFACE MORPHOLOGIES

University of Malaya

CHAPTER 3: METHODOLOGY

CHAPTER 4: ANALYSIS AND RESULT

CHAPTER 5: DISCUSSION AND CONCLUSION

LIST OF PUBLICATIONS

APPENDIX

University of Malaya

LIST OF FIGURES

University of Malaya

University of Malaya

University of Malaya

University of Malaya

LIST OF TABLES

University of Malaya

LIST OF ABBREVIATION

AFM	Atomic Force Microscopy
Alq3	Tris(8-hydroxyquinolinato)aluminium
BCM	Box Counting Method
BHJ	Bulk Heterojunction
BIR	Beam Induced Roughness
CMOS	Complementary Metal-Oxide-Semiconductor
DCM	Differential Box Counting Method
FBM	Fractional Brownian Motion
FGN	Fractional Gaussian Noise
GCP	Generalized Cauchy Process
HarFa	Harmonic and Fractal Image Analyzer
HOMO	Highest Occupied Molecular Orbital
ITO	Indium Tin Oxide
J_{sc}	Short-circuit-current density
LRD	Long Range Dependence
LUMO	Lowest Unoccupied Molecular Orbital
MBCM	Modified Box Counting Method
MDMO-PPV	Poly-[2-(3,7-dimethyloctyloxy)-5-methyloxy]-para-phenylene-vinylene
MOSFET	Metal-Oxide-Semiconductor Field Effect Transistor
NiTsPc	Nickel (II) phthalocyanine tetrasulfonic acid tetrasodium salt
NOMC	N-doped ordered mesoporous carbon
OFET	Organic Field Effect Transistor
OLED	Organic Light Emitting Diode
OPVC	Organic Photovoltaic Cells
OSC	Organic Solar Cells
P3HT	poly(3-hexylthiophene-2,5-diyl)
PC60BM	Fullerene ([6,6]-phenyl C60-butyric acid methyl ester)
PCBM	1-(3-methoxycarbonyl) propyl-1-phenyl [6,6]C_{61}
PDCTA	Perylene-3,4,9,10-tetracarboxylic dianhydride
PEDOT:PSS	Poly(3,4-ethylenedioxythiophene) polystyrene sulfonate
PEDOTNDIF	Naphthalenediimide (NDI)-based conjugated polymer
PL	Photoluminescence
POEM	Electric Potential Mapping by Thickness Variation
PSD	Power Spectral Density
PTB7-Th	Poly[4,8-bis(5-(2-ethylhexyl)thiophen-2-yl)benzo[1,2-b;4,5-b']dithiophene-2,6-diyl-alt-(4-(2-ethylhexyl)-3-fluorothieno[3,4-b]thiophene-)-2-carboxylate-2-6-diyl])
PV	Photovoltaic
RMS	Root Mean Square
SEM	Scanning Electron Microscopy
SIMS	Secondary Ion Mass Spectrometry
TOF	Time-Of-Flight

University of Malaya

LIST OF APPENDICES

University of Malaya

CHAPTER 1: INTRODUCTION

1.1 Organic and Inorganic Semiconductor

There are increasing efforts being invested for organic semiconductors as it tends to be competitive in replacing certain inorganic semiconductors (Servaites, et. al., 2011; Qian et. al., 2013; Xue et al., 2015). Studies on enhancing carriers transport and performance, integration of heterostructures and composite materials, and improving life-span of the devices are among the major focuses. Discoveries of organic molecules that respond sensitively to physical and chemical changes have encouraged the usage of the organic semiconductors for bio-sensing applications. There are also increased possibilities to create new organic semiconducting devices, which can be sensitized to X-ray radiation based on the composite materials (Blakesley et al., 2007).

The fabrication process for inorganic devices is complicated and costly because the organic devices can be produced and manufactured easily at large scale. Thus organic devices would be a best choice especially for some bulk sensing systems. Besides, some inorganic devices such as sensors can only function at higher temperature which limits the possibility of application in many areas. While on the other hand, a thin layer of organic compounds can be fabricated onto the structure of sensors to overcome this problem. The sensitivity and selectivity of the organic sensors can be customized by modifying the chemical structure depends on the application field and it might be applicable to diodes and transistors too (Goetz et al., 2009).

One of the examples of organic semiconductors for the display and lighting applications is the organic light-emitting devices (OLEDs) due to their increased efficiency and compatibility with high throughput manufacturing reason (Erickson & Holmes, 2010). Overall, the demand for OLED displays has increased tremendously in

University of Malaya

recent years compared to liquid-crystal displays because it has better brightness, colors, contrast, temperature stability, viewing angle, and faster response time (Jeong & Han, 2016). The heterogeneous single layers of emissive and charge-transport materials in OLEDs might become the great interest among the manufacturers because of its simple fabrication even though it has lower efficiency than the multi-layers structure OLEDs (Kasap & Capper, 2006). There are more recent developments and research demands in OLED architecture to improve the quantum efficiency by using a graded hetero-junction. For instance, the development of organic multi-layer structures in OLEDs has improved the efficiency of light-emission by achieving adequate number of charge carriers of opposite sign and further lowered the operating voltage (Xue et al., 2015).

On the other hand, organic field effect transistors (OFETs) are widely used as a sensor in electrolytes and invitro biosensing applications to avoid unwanted electrochemical reactions (Goetz et al., 2009). The OFETs can achieve similar characteristics to the inorganic field transistors with mobilities around 1 cm^2/Vs and on/off ratio greater than 10^6 (Kasap, 2006). However, it has high vulnerability to noise effects due to the large ratio between driving voltage and modulated current, which need to be taken into consideration.

In some applications, the chemical sensors made of organic compounds could possess higher sensitivity than the inorganic electronics. It had been used as the touching sensors for robots by Takao Someya in University of Tokyo (Someya et al., 2004). As compared to the silicon sensors that last for months and years, the organic sensors might be degraded within short period (about few days) due to the instability to the sensor's transistors. Moreover, the organic sensors will be the priority choice as the operating voltage could be lower from 40 volts to 10 volts (Collins, 2004).

On the other hand, due to the global warming issues and the shortage of non-renewable energy sources (e.g., petroleum and coal), the world is desperately looking

University of Malaya

for an alternate energy sources to replace the conventional power generation. In the recent years, the renewable energy from the Sun is one of the alternative energy sources as the demand for the electrical energy increases. Among the renewable energies, photovoltaics (PV) is one of the popular energy sources that has been used considerably for the last decade (Cabrera-Tobar et al., 2016). Inorganic solar cells have efficiently convert this energy source to electrical power and widely sold in the market. For the first few years of invention, the photovoltaic solar cell was more expensive than the other energy sources. The recent research to add in the organic compounds into the photovoltaic solar cells has made the production and manufacturing of large scale organic photovoltaic solar cells possible at lower cost.

Organic photovoltaic cells show promise as energy conversion devices because it is flexible, thinner and lighter than the inorganic solar cell. For example, organic photovoltaics (OPVs) have been gaining attention because of its lower fabrication cost for large area arrays, easy integration of heterostructures and composite materials, and also induced the possibility of using flexible substrate in organic photovoltaic devices (Jung et al., 2014; Xiong et al., 2015). The use of disordered interfaces in organic solar cell architectures can significantly increase the occurrence of fast charge transfer rate at the interfaces and hence achieve higher quantum efficiency (Vilmercati et al., 2009).

Overall, the organic semiconductors tends to be competitive in replacing certain inorganic semiconductors due to its leading advantages but its drawbacks need to be taken into consideration too. One of the limitations to be considered for organic semiconductor is the limited lifespan of the organic materials due to the instabilities against oxidation and reduction. The device degrades and having poor performance over time which always due to the re-crystallization and temperature variations. The presence of impurities also affect the performance of organic materials in semiconductors include

University of Malaya

the exciton diffusion length, charge separation and charge collection, and charge transport and mobility.

Therefore, intensive researches have been carried out to study the characteristics of organic semiconductors, from its material microstructure to interfacial morphologies. In general, there are two types of morphologies that have been extensively studied for organic semiconductor, namely ordered and disordered organic semiconductors. Ordered organics semiconductor consists of inorganic microstructures mixed with organic semiconductor and having different microstructure pattern with disordered organics semiconductor, as shown in Figure 1. The ordered morphology can be precisely controlled and can have more charge collection efficiency as compared to the disordered pattern (Williams et al., 2008). With ordered geometry, exciton dissociation can be facilitated and the mobility of charge carriers is much higher as compared to disordered geometry interface. If the channels are straight and perpendicular to the substrate, the charge carriers can also be easily transported to their respective electrode.

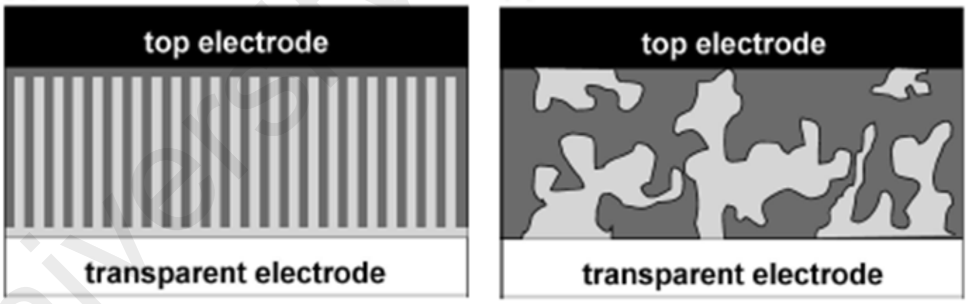

Figure 1.1: Ordered and disordered microstructures (Hoppe, 2004).

However, disordered microstructure does not produce straight channels for this purpose. In such amorphous active layer, even though the polymer chain packing is disrupted with the irregular and complex pattern, the total interface area between donor and acceptor materials has been increased for more carriers to facilitate across the

University of Malaya

electrodes. Consequently, the study of the active layer morphology crucially reveals the charge transport phenomenon in order to enhance the overall device performance.

Therefore, a detailed study is carried out in this research to investigate and overcome the mentioned limitations for disordered microstructure of an organic photovoltaic cell. The morphology of the active layer has been studied extensively to visualize the charge mobility phenomenon across the interface in order to improve the overall device performance.

1.2 Problem Statements

In organic photovoltaic cells, the excitons (electrons and holes) are firmly bound to each other and only dissociate at interfaces such as electrodes and the interface of donor-acceptor organic compound to produce charge flow (Norton, 2009). A continuous percolation pathway will ensure higher electron transfer to the electrodes without being trapped in the half way or recombine at the donor-acceptor interface (Moulé, 2010) which appears to be one of the factors to characterize the overall performance of a photovoltaic device. In order to create such a percolation pathway, incorporation of conduction nanowires into bulk heterojunction and electrode materials has shown significant improvement in the performance of solar cells (Ben Dkhil et al., 2012). The fiber alignment and its geometry of connectivity need to be studied and characterized for further improvement.

In bulk heterojunction solar cell, the electron donors and acceptors are mixed together, forming disordered microstructure which do not produce straight channels for carriers to the interface. The polymer chain packing is disrupted with the irregular and complex pattern. Even though the total conduction are between donor-acceptor has increased, the disordered microstructures might cause mass of recombination failure to facilitate the carriers across the interface.

University of Malaya

However, Vilmercati (2009) suggested that the use of disordered interfaces in OBSC or OPVC architectures can significantly increase the occurrence of fast charge transfer rate at the interfaces and hence achieve higher quantum efficiency. More efforts are needed to understand the disordered microstructure architecture of organic solar cells in order to achieve higher quantum efficiency. This is because the geometry and structures of the surfaces play crucial role in its performance and reaction rate (Lee & Lee, 1995). The study of disordered microstructure morphology of organic materials is crucially important in order to understand the amorphous structural order on a super-molecular scale, concerned with dimensions equal or less than 10^{-9} meters. It reveals important information of the materials properties such as charge carrier mobility, optical absorption and mechanical quality. Therefore, the morphology of the disordered organic solar cell needs to be extensively studied to investigate the charge mobility across the interface.

University of Malaya

1.3 Objectives

Texture analysis and fractal methods provide 2D descriptors that are good descriptors of surface roughness and heterogeneity. The calculation of fractal dimensions and other related parameters are useful as quantitative morphological and developmental descriptors. The greater the morphologic complexity of an object, the higher its fractal dimension.

Thus the main objectives of this study are:

i) to investigate geometrical features of microstructure morphologies in disordered organics solar cell by using fractal methods,
ii) to relate fractal parameters with carrier transport properties,
iii) to study and quantify device performance based on microstructure morphological features.

1.4 Thesis outline

This thesis is written to demonstrate the importance of disordered microstructure morphology study and the importance of power spectral density (PSD) and Generalized Cauchy process (GCP) models for studying surface morphologies of organic thin film. The chapters are structured to provide a clear literature review on the ordered and disordered organic semiconductors and the use of fractal parameters to quantify the charge transport properties.

Chapter 2 reviews on the surface texture characterization of disordered microstructure morphologies. Material microstructure and interfacial morphologies are described in this section. Literature review has been done on the charge transport study in amorphous microstructure morphology by fractal methods. Fractal theory and its application has been further explained to provide the initial idea of applying multi-dimensional descriptors for surface roughness and texture heterogeneity. Other conventional surface modelling has been briefly discussed as well. Surface analysis and the characterization of a solar cell are explained in the last part of the chapter.

Chapter 3 explains the material preparation in this study and the process of image acquisition and pre-processing details. Besides, the methodology of PSD and GCP models, box counting method, fractal spectrum and percolation theory have been explained. The dual-fractal parameters (GCP) is related for the first time to charge transport properties by measuring the short-circuit current density (J_{sc}) of the OPV with surface treatment.

Chapter 4 discusses the results from the modelling techniques in details. The application of Fourier based power spectral density (PSD) and the dual parameter stochastic surface model (GCP) are demonstrated for describing complex surface morphologies. The results from the application of fractal spectrum and the percolation theory have also been described in this section.

University of Malaya

Chapter 5 discusses the possible limitations of the models used in this study, concludes the work and suggests the possible future work on the approaches.

University of Malaya

CHAPTER 2: MATERIAL SURFACE MORPHOLOGIES

In this chapter, the basic concepts of organic semiconductor involving monocrystalline, polycrystalline and amorphous materials has been reviewed. The surface image texture characterization of disordered microstructure morphologies has been focussed especially on the material microstructure and interfacial morphologies. Literature review has been done on the charge transport study in amorphous microstructure morphology by using fractal methods. In this section, fractal theory and its application has been further explained to provide the initial idea of applying multi-dimensional descriptors for surface roughness and texture heterogeneity. Besides, other conventional surface modelling has been briefly discussed as well. Surface analysis and the characterization of a solar cell are explained in the last part of the chapter, which includes the general review on the root-mean-squared (RMS) height fluctuation, power spectral density (PSD), semivariograms, and fractal box-counting methods.

University of Malaya

2.1 Review of Basic Concepts of Organic Semiconductor

The geometry and structures of the surfaces play crucial role in its performance and reaction rate. The microstructure morphology (also called as nano-morphology) of organic materials is a study of structural order on a super-molecular scale, concerned with dimensions in the order of 10^{-9} meters or less. Morphologies of the surfaces play crucial roles in the system performance, particularly related to interfacial contact and transport properties (Lee & Lee, 1995). It reveals important information of the materials properties such as charge carrier mobility, optical absorption and mechanical quality.

The study of material properties such as mechanical, heat capacity, and electrical conduction are important for various applications. The states of matter are solid, liquid, gas and plasma. Each state of matter is characterized by its structural arrangement and resistance to change of shape or volume. The arrangement of atoms in solids are tightly bound to each other, and the atoms may be arranged in a regular geometric pattern (crystalline and polycrystalline) or irregular structure (non-crystalline).

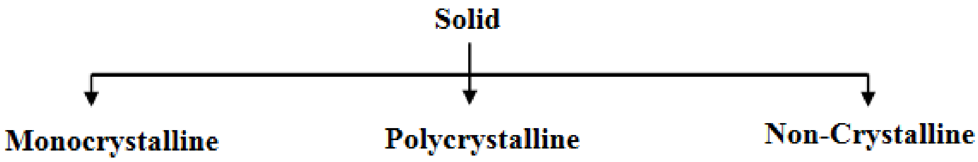

In solid, the particle (atoms, molecules or ions) may be arranged in an ordered repeating pattern, are known as crystals. A monocrystalline or single crystal has no grain boundaries in its crystal lattice, with continuous unbroken structural arrangement (e.g. diamond). Polycrystalline (or semicrystalline) is made of many crystallites (single crystals) of varying size and orientation (metals, ceramics, rocks, etc). A non-cystalline solid consists of disordered structure of short range interconnected particles, such as glass and polymers.

2.1.1 Monocrystalline versus Polycrystalline Materials

In a monocrystalline solid, the particles (atoms, molecules, or ions) are packed in a highly ordered, symmetrical and repeating pattern, as shown in Figure 2.1. Production of high strength material from monocrystalline is possible due to the absence of grain boundaries which lower the chances of deformation under temperature treatment. In semiconductor industry, large scale of single crystals of silicon is produced for its efficient quantum mechanical properties. Examples of single crystals are rock salt, quartz, diamond, sapphire, etc.

University of Malaya

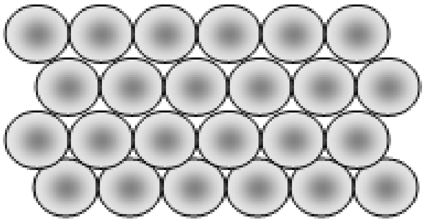

Figure 2.1: The two-dimensional particle arrangement in a monocrystalline solid.

A polycrystalline solid consists of many crystallites (single crystals) of varying size and orientation. The crystallites can be arranged in random orientation with preferred structure direction (Qian et al., 2013), as shown in Figure 2.2. Different orientations of crystallites meet at an interface called grain boundaries, which playing crucial role in material deformation (or creep). In the field of semiconductor, polycrystalline silicon is used as a raw material by the solar photovoltaic cells and electronics such as metal-oxide-semiconductor field-effect transistor (MOSFET) and complementary metal-oxide-semiconductor (CMOS).

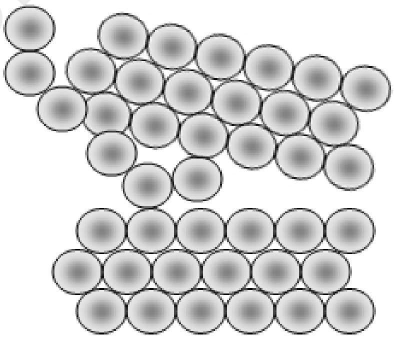

Figure 2.2: The two-dimensional particle arrangement in a polycrystalline solid.

For example, ordered organic semiconductor consists of inorganic microstructures mixed with organic semiconductor and having different microstructure pattern with disordered organics semiconductor. The ordered morphology can be precisely controlled and can have more charge collection efficiency as compared to the disordered

University of Malaya

pattern (Williams et al., 2008). For example, the organic photovoltaic cell (OPVC) is designed to be ordered microstructure so that its surface can easily facilitate exciton dissociation and charge transfer.

With ordered geometry, the mobility of charge carriers is higher as compared to disordered geometry interface. If the channels are straight and perpendicular to the substrate, the charge carriers can also be easily transported to their respective electrode. Another example has been shown in Figure 2.3, the microstructure of metal-free N-doped ordered mesoporous carbon materials (NOMC) which displayed outstanding electro-catalytic activity in the oxygen reduction reaction, achieving a remarkably enhanced kinetic current density (Sheng et al., 2015).

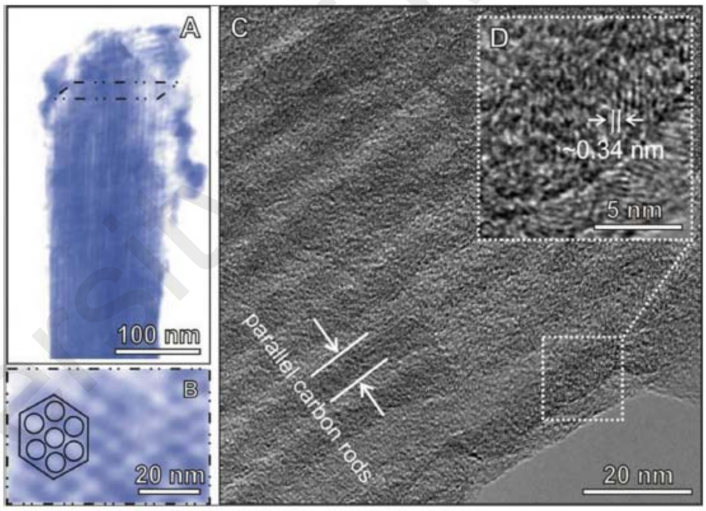

Figure 2.3: The microstructure of metal-free N-doped ordered mesoporous carbon materials (NOMC) with indication of the position of the parallel carbon rods and of the graphitic layers (Sheng et al., 2015).

2.1.2 Amorphous & Disordered Materials

Amorphous solids do not have long range order in the atomic arrangement. The particles are interconnected in random and disordered pattern. Amorphous polymer is one of the disordered materials that has long-chained molecules in its structure. The

University of Malaya

other examples of amorphous solids are glass, plastic, and organic thin films, with the atomic structure shown in Figure 2.4. The disordered structure has dangling bonds between particles which may effects anomalous electrical behavior.

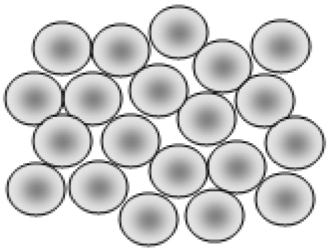

Figure 2.4: The two-dimensional particle arrangement in an amorphous solid.

There are two types of amorphous solids that have been widely produced in the solar photovoltaic cells now, namely amorphous silicon (inorganic) and amorphous organic materials. Amorphous silicon is generally known as hydrogenated amorphous silicon (a-Si:H), which can be produced at large scale with lower production cost as compared to crystalline silicon (c-Si). The atomic arrangement of a-Si is three dimensional atomic structure without long range order.

A-Si can be deposited on a wide range of substrates and it absorbs more energy than a c-Si. However, the overall efficiency of an amorphous silicon thin film is lower than a c-Si thin film. Research and investments have been continuously carried out on a-Si to improve its quantum mechanical properties as it requires less materials and inexpensive for production.

For amorphous organic materials, it does not possess any crystalline structure. As shown in Figure 2.5, carbon nanotubes have atomic structural pattern of tangled mass with long chained molecules. The irregularity and complex pattern of the polymer chain arrangement is disrupted in disordered microstructure.

University of Malaya

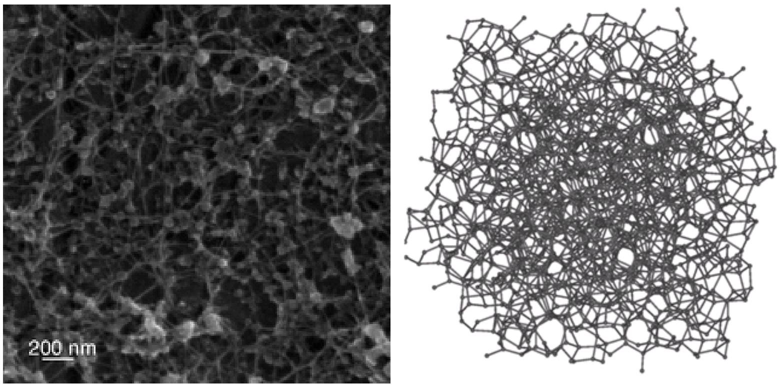

Figure 2.5: The irregularity and complex pattern of the carbon nanotubes chain arrangement (Geest et al., 2010).

As mentioned earlier, the use of amorphous interfaces in organic solar cell architectures can significantly increase the occurrence of fast charge transfer rate (CT) at the interfaces and hence achieve higher quantum efficiency. In recent years, there are plenty of researches on the application of amorphous organic materials in semiconductor industry, such as PC60BM fullerene ([6,6]-phenyl C60-butyric acid methyl ester) (Dang et al., 2013), P3HT (poly(3-hexylthiophene-2,5-diyl)) or PS (polystyrene) (Simonetti & Giraudet, 2014), PEDOTNDIF (naphthalenediimide (NDI)-based conjugated polymer) with neat C_{70} (Yasuda & Kuwabara, 2015), and recently synthesized PTB7-Th (Poly[4,8-bis(5-(2-ethylhexyl)thiophen-2-yl)benzo[1,2-b;4,5-b']dithiophene-2,6-diyl-alt-(4-(2-ethylhexyl)-3-fluorothieno[3,4-b]thiophene-)-2-carboxylate-2-6-diyl]) (He et al., 2015), and many more.

As shown in Figure 2.6, the bilayer hybrid solar cell is fabricated by depositing conjugated polymer on the top of an inorganic semiconductor layer (Malek et al., 2013). Lack of conduction area between donor-accepter has caused very low power conversion efficiency and the conjugated polymers have short exciton diffusion lengths. The layer thickness should also be in the same range with the diffusion length to increase the diffusion of most excitons to the interface and break up into carriers.

University of Malaya

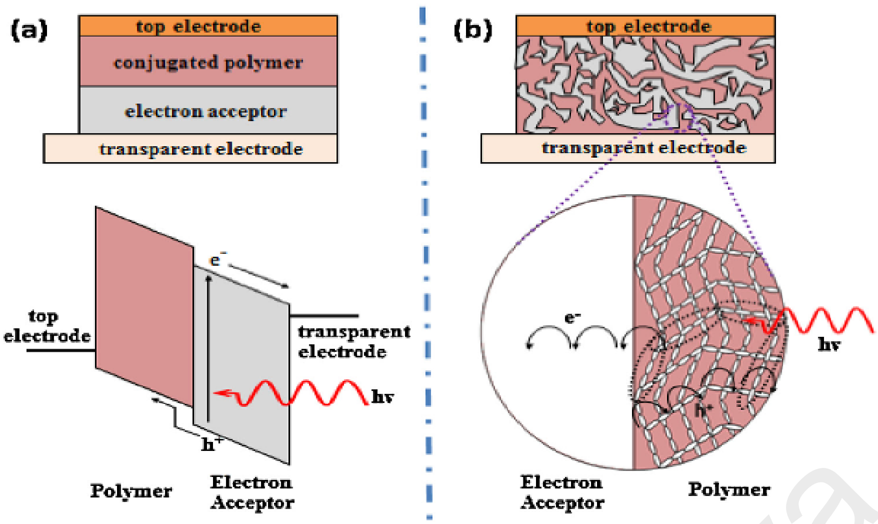

Figure 2.6: The device configurations for (a) bilayer hybrid solar cell and (b) bulk heterojunction hybrid solar cell (Malek et al., 2013).

The excitons dissociation occurs at the interface of donor-acceptor organic compound, producing free electrons and holes as charge carriers. These charge carriers should be transported and collected at the electrodes to ensure the generation of photocurrent. Moreover, charge transport phenomenon in disordered organic photovoltaic cells are affected by the presence of impurities that influence the mechanical properties such as the exciton diffusion length (Garcia-Belmonte, 2003), rapid charge separation and collection as well as charge mobility rate. Even though the total conduction are between donor-acceptor has increased, the disordered microstructures might cause mass of recombination failure to facilitate the carriers across the interface. Therefore, a continuous percolation pathway that assures higher electrons and holes transfer to the electrodes without been trapped in the half way or recombine at the donor-acceptor interface (Cen et al., 2012; Grover et al., 2012), which appears to be one of the factors to characterize the overall performance of a photovoltaic device.

To determine the performance of a photovoltaic device, the magnitude of the photocurrent generated in the module is crucially important. Studies have been done to

University of Malaya

combine the percolation model with other methods to quantify the diffusivity such as molecular trajectory algorithm and blind-ant rules (Cen et al., 2012) and bimodal Gaussian density of states (Yimer et al., 2009). At the same time, research has also been done by using different models to evaluate precisely the characteristics of a current-voltage curve without spending high computation cost. For instance, guest-host systems to predict the *J-V* behavior has been adopted by Jakobsson et al. (Jakobsson et al., 2009). However, there is a possibility to obtain falsify evaluation of the current-voltage (*J-V*) graphs due to the parasitic contribution from injection or extraction barriers (Widmer et al., 2013). It was suggested that a model-free method, namely electric potential mapping by thickness variation (POEM) can be used to investigate the charge mobility leading to the prediction of *J-V* data.

Besides, recent studies have shown that fractal methods and percolation theory can be applied to analyze the charge mobility in an organic material (Vakhshouri et al., 2013; Evans et al., 2016), but the significant influence of a fractal-percolative network that affects the charge transport in an organic thin film need to be further understood (Grover et al., 2012). In present study, fractal surface modelling methods are adopted to characterize the surface properties in disordered thin films.

2.2 Material Microstructures and Interfacial Morphologies

Organic photovoltaic cell (OPVC) and organic based solar cell (OBSC) architectures have been studied extensively to significantly improve charge transfer rate at the organic thin film interfaces (Kwon et al. 2011). It has been greatly adopted in inorganic photovoltaic because of its lower fabrication cost for large area arrays, easy integration of heterostructures and composite materials, and also induced the possibility of using flexible substrate in OPVC. Higher quantum efficiency has been achieved in OPVC materials by structured designs of the interfaces and electrodes to enhance charge

University of Malaya

transfer. The morphology study of the active layer is to describe the geometry and structures of the surfaces that reveal its performance and reaction rate. Morphologies are fundamentally important in revealing all the four main processes in OPVC materials, namely photon absorption (Freitas et al, 2012), exciton diffusion (Vogel et al., 2006), charge separation (Brinker & Dunphy, 2006) as well as charge carrier transport and collection (Ruderer & Müller-Buschbaum, 2011).

One of the drawbacks needs to be considered for OPVC is the limitation of lifespan of the organic materials due to the instabilities against oxidation and reduction. The device degrades and having poor performance over time which always due to the re-crystallization and temperature variations. The presence of impurities also affect the performance of organic materials in OPVC include the exciton diffusion length; charge separation and charge collection; and charge transport and mobility. These properties can affect the overall power conversion efficiency of a OPVC, which can be quantified by measuring the short circuit current or photocurrent density (J_{sc}) and the open circuit voltage (V_{oc}) of the solar cell (Manor et al., 2011). The architectures of bilayer heterojunction and bulk heterojunction of a photovoltaic cell are shown in Figure 2.7.

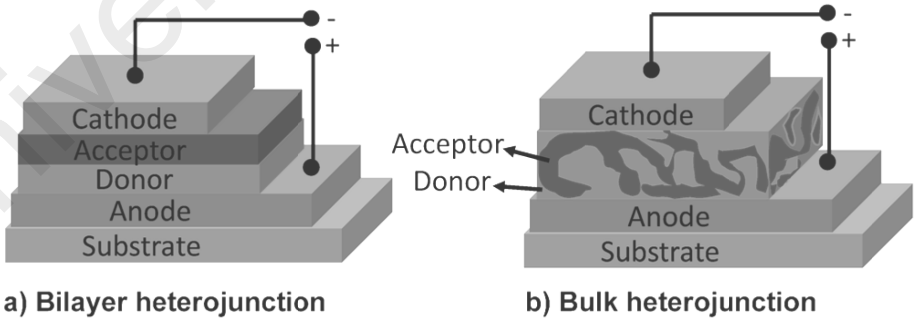

Figure 2.7: (a) Bilayer heterojunction, (b) bulk heterojunction of a photovoltaic cell architecture (Kumaresan et al., 2014).

Firstly, the excitons are created through light harvesting. Part of the excitons diffuse across the donor layer and reach donor-acceptor interface in a bilayer heterojunction OPVC. The excitons (electrons and holes) are firmly bound to each other and only

University of Malaya

dissociate at interfaces such as electrodes and the interface of donor-acceptor organic compound to produce charge flow. When the potential energy difference of the electronic states of donor-acceptor materials is large enough, it facilitate the electrons in the excitons (of the donor materials) to the acceptor layer. This is called charge separation, whereby the separated charges partly diffuse to the acceptor layer (electrons) and some transfer back to their origin donor layer (holes).

Finally, charges are collected when these charges diffuse to their respective electrodes. However, the density of the charge flow is limited by the thickness of the active layer. The diffusion length of the charge in OPVC is short (in the orders of magnitude of 10 nm) as compared to the silicon inorganic solar cell materials, where the charge's diffusion length is around 100 µm. Therefore, thinner active layer (film) tends to increase the amount of charge flow as compared to a thicker one.

At the same time, the interface distance between donor and acceptor materials should be relatively small to avoid the excitons with small diffusion length to decay back to the ground state. To accomplish this smaller interface distance, bulk heterojunction films (BHJ) have been designed by using spin coating method to fabricate the donor-acceptor materials simultaneously onto the module. The charge collection is relatively higher with smaller domain size of donor-acceptor materials been implemented. Nevertheless, smaller domain size of donor-acceptor materials possibly result in quality degradation of the device, which should be taken into consideration. In this way, amorphous materials are another option in OPVC active layer.

Vapour deposition method has been used to produce an ordered microstructure on organic solar cell, while spin coating method is used to improve the crystalline annealing for BHJ (Li et al., 2007). For amorphous interface, spin coating is often applied. As mentioned earlier, the use of amorphous/disordered interfaces in OPVC architectures can significantly increase the occurrence of fast charge transfer rate (CT)

University of Malaya

at the interfaces and hence achieve higher quantum efficiency (Servaites et al., 2011). These blended films of donor-acceptor materials have shorten the exciton hopping or diffusion length, which effectively enhance the overall charge transport across the electrodes. Recently, there are plenty of research work focusing on the improvement of diffusion length of the organic materials in OPVC (Yambem, et al., 2012; Vakhshouri et al., 2013).

As shown in Figure 2.8, in amorphous active layer, even though the polymer chain packing is disrupted with the irregular and complex pattern, the total interface area between donor and acceptor materials has been increased for more carriers to facilitate across the electrodes. However, the power efficiency is remaining smaller as compared to ordered crystalline. Due to the quantum mechanical nature of the charge transport, its depends on the subsequent probability function, whereby the transport process is commonly referred to as hopping transport or random walk. In the next section, the material surface modelling to show profound connection between the probability distribution of random walks on disordered network will be discussed.

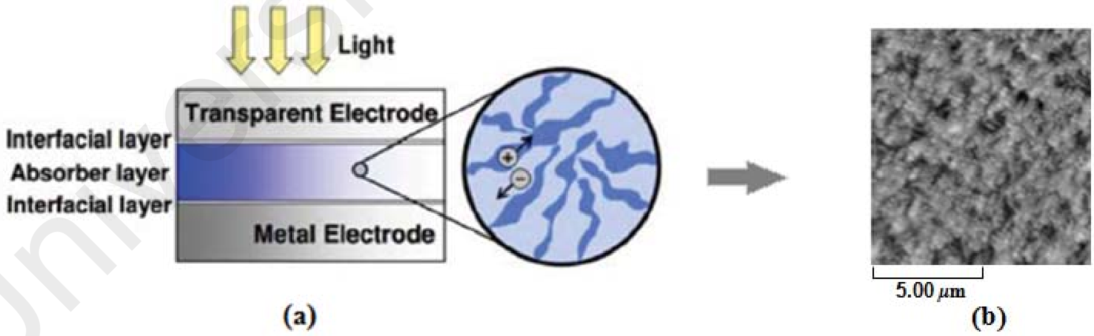

Figure 2.8: (a) Bulk heterojunction of solar cell with amorphous active layer, (b) morphological image of the amorphous layer (Servaites et al., 2011).

Consequently, the study of the active layer morphology crucially reveals the charge transport phenomenon in order to enhance the overall device performance. Surface morphologies of active layer interfaces provide useful information in carrier transport dynamics. The charge transport properties can be examined by numerous techniques,

University of Malaya

such as time-of-flight (TOF) and space charge limited current techniques, which are used to characterize "bulk" conduction properties of organic films, and percolation model which is also widely used to describe the transport mechanism dynamics.

Studies of thin film morphologies can reveal useful information on various surface features that may contribute directly or indirectly towards enhancing charge carrier mobility across the interfaces. Therefore, the microstructure morphology of the disordered organic active layer has been extensively studied in this work to visualize the charge transport phenomenon and to quantify several important transport parameters. The understanding of these parameters is crucial to increase the facilitation of charge carriers across the interface for improving the device performance for solar photovoltaic cells.

To characterize the microscopic morphology and architecture, Scanning Electron Microscopy (SEM) is one of the imaging techniques which has often been used whereby a specimen will be scanned with a highly focused electron beam. An example of SEM image for organic solar cells (NiTsPc thin film) after chloroform solvent treatment is shown in Figure 2.9 (Fakir, 2013). Another SEM example is shown in Figure 2.10, where spin-cast and drop-cast samples of MDMO-PPV (poly-[2-(3,7-dimethyloctyloxy)-5-methyloxy]-para-phenylene-vinylene) with PCBM (1-(3-methoxycarbonyl) propyl-1-phenyl [6,6]C_{61}) in toluene solution are compared to investigate film morphological change due to the effect of drying time (Hoppe, 2004).

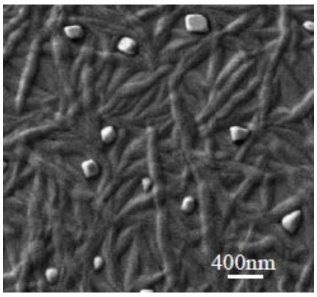

Figure 2.9: The SEM image for organic solar cells after chloroform solvent treatment (Fakir, 2013).

University of Malaya

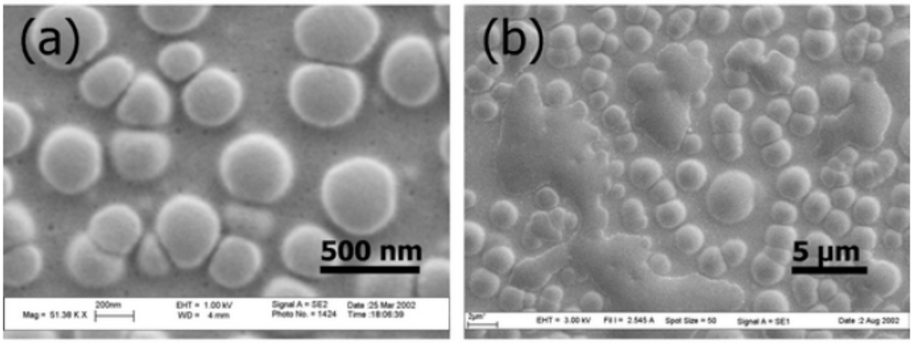

Figure 2.10: The SEM images for (a) spin-cast and (b) drop-cast films of MDMO-PPV mixed with PCBM in toluene solution (Hoppe, 2004).

Transmission Electron Microscopy (TEM) is using electrons instead of light source to produce higher resolution image of nano-scaled materials. The electron source consists of a cathode which produces electrons when heated, and an anode which accelerate the electrons towards the specimen. The electron beam is then directed into the imaging system by electromagnetic field that works like optical lens to focus the electrons. When the electron beam passes through the specimen, it hit the phosphorescent plate of the screen that forms and enlarges the image of the specimen. This TEM technique has been widely applied for specimen with irregular density, whereby the electrons pass through more easily in porous material.

In this study, only AFM images have been used thus it will be elaborated in this section. The Atomic Force Microscopy (AFM) is the improved version of Scanning Tunneling Microscopy (STM) by Binnig, Quate and Gerber in the year of 1986. AFM microscopy is a topology-scanning equipment setup for microstructure imaging up to atomic resolution to visualize the amplitudes of the electronic wave function. The local properties such as surface height, magnetism and friction can be measured by using AFM.

There are three common measuring modes for the AFM where a probe with a sharp tip is scanning back and forth across a square-sized specimen through: contact mode,

University of Malaya

non-contact mode, and dynamic force (tapping) mode. AFM measurement depends on the forces between the tip and the specimen, which is measured in term of the deflection of the microlever, which known as the stiffness of the cantilever. The stiffness of the cantilever is measured through Hooke's law: $F = kx$, where F is the force, k is the stiffness of the microlever, and x is the bending distance of the lever.

(a) *Contact mode:* The tip mounted on a lever is pressing directly onto the specimen surface with a constant force or constant height. The tip can be maintained at certain degree of deflection under constant force mode, while the constant height mode is used for relatively small and flat specimen surface.

(b) *Non-contact mode*: The tip is not touching the specimen surface directly in this operation mode. The surface scanning is based on the changes of resonant frequencies or amplitude of the lever. The oscillating cantilever is used to probe the surface at a nano-scaled distance where long-range attractive forces are the dominant interaction. The example of a topographic image by using non-contact mode scanning is shown in Figure 2.11.

University of Malaya

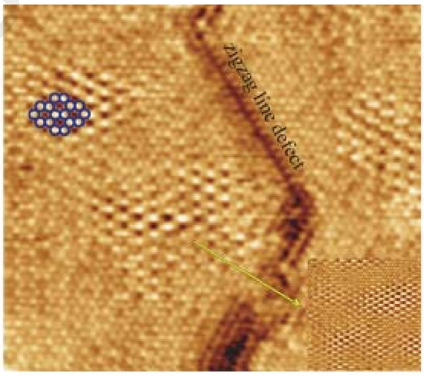

Figure 2.11: The AFM topographic image by using non-contact mode scanning extensively the domains around a zigzag line defect of the Sn/Ge (Yi et al., 2007).

(c) *Tapping mode*: The tip is tapping directly on the specimen surface, whereby the cantilever is oscillating at intermittent-contact mode. A rigid cantilever is needed to avoid the embedment of the tip into the specimen layer. Especially for soft specimens, the lateral resolution is higher with this operating mode as it does not drag along the specimen surface. A two dimensional AFM images of the polymer microstructure by using tapping mode is shown in Figure 2.12.

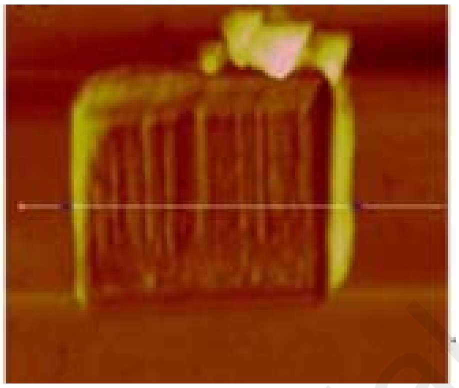

Figure 2.12: A two dimensional AFM images of the polymer microstructure by the dynamic ploughing with the TAP525 probe at driving amplitude of 1000 mV (Yan et al., 2015).

2.3 Material Surface Modelling

The microstructure morphology (also called as nano-morphology) of organic materials is a study of structural order on a super-molecular scale, concerned with dimensions in the order of 10^{-9} meters or less. Morphologies of the surfaces play crucial roles in the system performance, particularly related to the interfacial contact and transport properties. There are many concrete models that serve as surface generators, which can be used to simulate the morphological features. These include the Kardar-Parisi-Zhang (KPZ) model (Kardar et al., 1989), Brownian motion and the associated fractional Brownian motion (FBM) (Mandelbrot, 1982) indexed by the Hurst exponent and the generalized Cauchy process (GCP). In this section, the dynamic surface modelling (conventional models) has been reviewed, followed by geometric surface modelling (fractal models).

University of Malaya

2.3.1 Dynamic Surface Modelling

In order to understand the surface and interface growth processes, the surface roughness and the associated scaling properties of the surfaces are usually examined. In 1989, Kardar and authors (Kardar et. al., 1989) implemented the Kardar-Parisi-Zhang (KPZ) model which was proposed as a non-linear stochastic partial differential equation to describe the temporal change of the height $h\ (\vec{x}, t)$, whereby the scaling properties of the surface has significant effects on the growth velocity. The KPZ equation

$$\frac{\partial h}{\partial t} = v\nabla^2 h + \frac{\lambda}{2}(\nabla h)^2 + \eta(\vec{x}, t), \tag{2.1}$$

where v and $\frac{\lambda}{2}$ are constants that represents the surface tension and excess velocity respectively, and η is a Gaussian white noise with zero mean and variance:

$$\langle \eta(\vec{x}, t)\eta(\vec{x'}, t')\rangle = D\delta^d(\vec{x} - \vec{x'})\delta(t - t'), \tag{2.2}$$

where d is the dimension of the substrate. For fixed t, the local roughness w scales as $w \sim r^\alpha$ for r is less than the total surface length ($r \ll L$). In the growth regime, the average roughness increases as $w \sim t^{2\beta}$ where β is the growth exponent (Aarão Reis, 2006). In d = 2, the best numerical estimate of KPZ exponents of α is 0.38−0.39 and β around 0.23 (Paiva & Aarão Reis, 2007). However, KPZ model is limited in determining steady state distributions for three dimensional systems (growth in two-dimensional substrates).

The height and roughness distributions in thin films had been studied with KPZ scaling in order to understand the basic mechanism of thin films growth by Paiva and Aarão Reis (Paiva & Aarão Reis, 2007). In their work, they concluded that the roughness distributions corroborate well with KPZ model but the height distributions showed some deviations in extracting the accurate universal values of amplitude ratios.

Other than KPZ model, there were other surface generators/models used to characterize the surface morphology. Hartree-Focks semi-empirical Austin Model One

University of Malaya

was adopted to characterize geometrical structures of short oligomers in the polymer blend, which were observed by AFM (Viville et al., 1995). Density functional theory (DFT) has been adopted in (Maldonado & Stashans, 2016) to process the quantum-chemical calculations in order to predict the absorption properties on the surface. Same DFT theory has been applied in (Yang et al., 2010) with generalized gradient approximation to simulate the microscopic reaction mechanism in the early growth of thin films. Besides, kinetic modelling is one of the surface generators used to determine the surface diffusion at initial stage of thin film deposition (Galdikas, 2008).

2.3.2 Geometric Surface Modelling

Fractal models has been widely used to analyze signals in different applications, e.g. medical imaging applications, geographical image analysis, morphological study, physical properties of materials and other fields. Its efficiency has been demonstrated in classification and segmentation experiments where it was used as an additional texture parameter. Texture analysis by using fractal methods provide 2D descriptors that are a good reflect of surface roughness and heterogeneity. The calculation of fractal dimensions and other related parameters are useful as quantitative morphological and developmental descriptors.

The concept of fractal theories has been extensively used in modelling nature objects with complexity in morphology, branching and irregular in shape. The contribution of the "Minkowski cover" and "Kolmogorov box" methods to compute fractal characteristics for a texture roughness are convincingly presented in many research work. The greater the morphologic complexity of an object, the higher its fractal dimension.

In biomedical field, bone mineral density (BMD) analysis is used to determine the stages of osteoporosis by determining the ranges of frequencies over fractal dimension

University of Malaya

(Dougherty & Henebry, 2002). The fractal dimension increases with BMD when computed over a lower range of spatial frequencies and decreases for higher ranges using the power spectral method. Fractal analysis in this case improved the prediction of strength and elastic modulus of a bone. The fractal based texture analysis of radiographs is used to quantify trabecular (bone) structure and different density of tissue. A more cell-dense tissue usually has a higher fractal dimension than a tissue with fewer cells. A tumor has a higher fractal mass dimension and its density will maintain the same as it grows bigger that resulting in more rapid growth rate and a larger final size. For example, breast tumor results in a very dense tissue which has higher fractal dimension as compared to a normal breast tissue (Tambasco et al., 2010).

Fractal geometry has been widely used as 2D descriptors to determine surface roughness and heterogeneity. For example, extremely rough surface would give $D \sim 3$, while a marginal (smooth) surface has $D \sim 2$. Meanwhile, a Brownian fractal surface gives a unique $D = 2.5$. The greater the morphologic complexity of an object, the higher its fractal dimension (Tambasco et al, 2010).

Fractal geometry has been proven to be useful for characterizing complex signals and images in diverse applications, for example morphological study of material surfaces (Sahoo et al., 2006), physical properties of materials (Biancolini et al., 2006), biomaterials surface (Bojović et al., 2008), hematology (Mashiah et al., 2008), medical imaging (Timbó et al, 2009), geographical image analysis and others. Fractal theory provides robust multi-dimensional descriptors for surface roughness and texture heterogeneity.

Fractals can be found in many nature and man-made objects. A fractal object shows self-similarity on all scales, whereby the same patterns repeat over and over in a never-ending form. For instance, Koch curves, begin with a straight line and then divided it into three equal segments, as shown in Figure 2.13. The middle segment is replaced by the two

University of Malaya

segments of an equilateral triangle. The same procedure is repeated by replacing each of the four resulting segments and dividing them into three equal parts again. The length of the intermediate curve at the *n*th iteration is $(4/3)^n$, where $n = 0$ denotes the initial straight line segment. Therefore Koch curve has an infinite perimeter in the limit but its limit area is finite (Sergeyev, 2016). For example, the total length of a coastline increases when a smaller ruler is used, as shown in Figure 2.14.

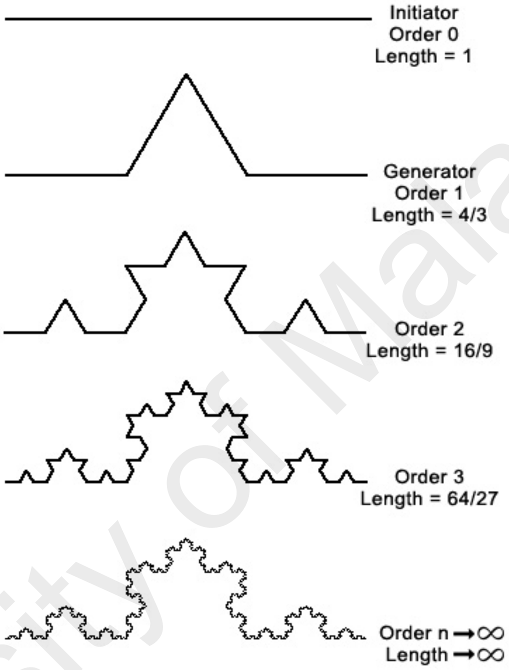

Figure 2.13: The iterations of Koch curve (Sergeyev, 2016).

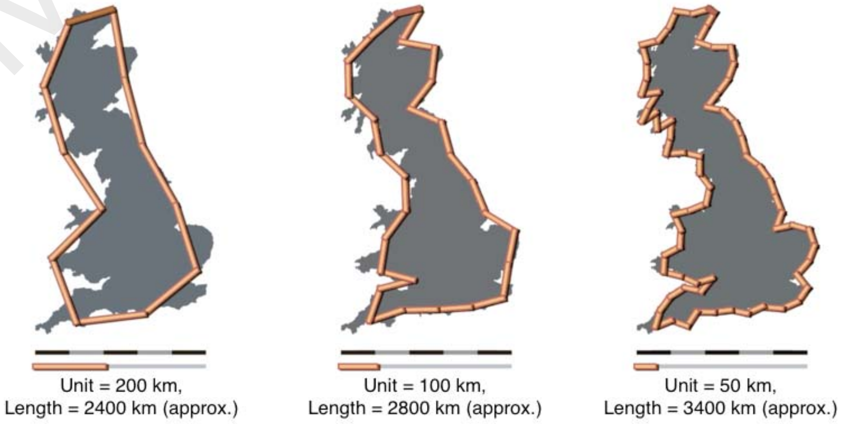

Figure 2.14: Smaller ruler contributes to the increment of the coastline length, which also shows a better and more accurate coverage of the entire coastline (Mandelbrot, 1967).

University of Malaya

Another famous geometrical fractal is Sierpiński triangle, which is constructed by repeatedly removing the central triangle from the previous generation, as shown in Figure 2.15. The step starts with an equilateral triangle, and then substitute the removed triangle with smaller congruent equilateral triangles. The number of triangles increases by a factor of 3 each step.

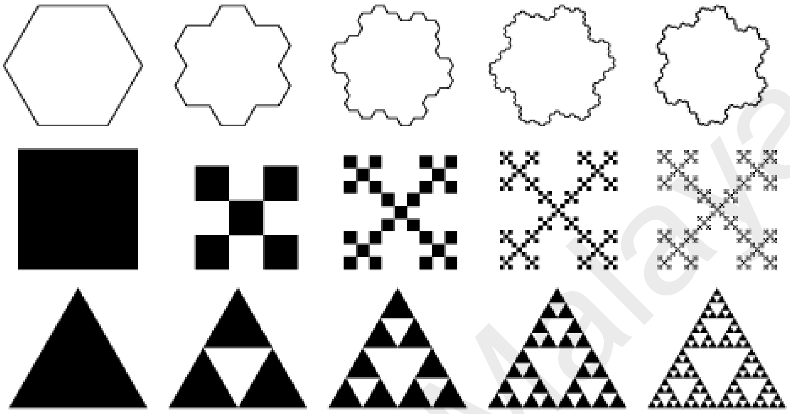

Figure 2.15: Illustrated fractals known as the Gosper island, box fractal, and Sierpiński triangle.

In nature, branching process can be found from tiny blood vessels (Mashiah et al., 2008), lungs (Lee et al., 2014), neurons (Stam & Reijneveld, 2007), trees, and river networks (Rinaldo et al., 1993). Plotting of a log-log graph of mass versus different scales will contribute a straight line with gradient that represents the fractal dimension. For example, fractal branching of lungs indicate the surface area for oxygen and CO_2 exchange. Fractal analysis has been applied to further quantify the histo-morphological of lung cancer, as shown in Figure 2.16.

University of Malaya

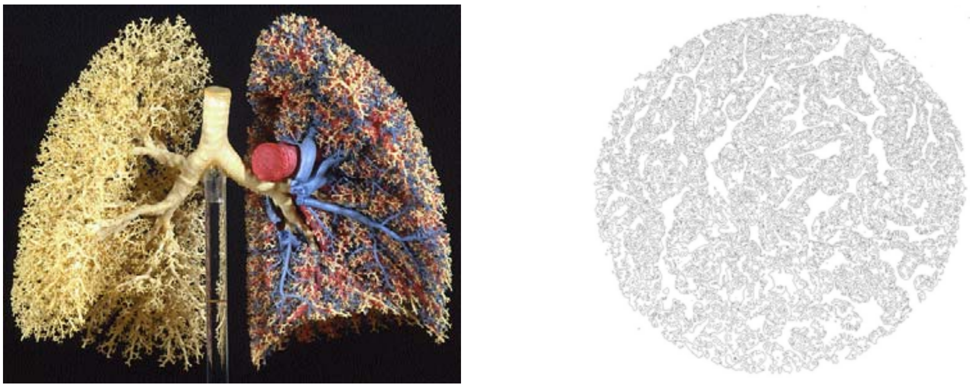

(a) (b)

Figure 2.16: (a) The fractal branching of lungs, (b) the outline image of lung adenocarcinoma cell whereby the fractal dimension is calculated with appropriate spatial scale (Lee et al., 2014).

Fractal analysis has also been widely applied to study the geomorphology such as river network and forestation, as shown in Figure 2.17. In most study, river patterns exhibit power laws which reveal the fractal behavior that describes the river basin morphology.

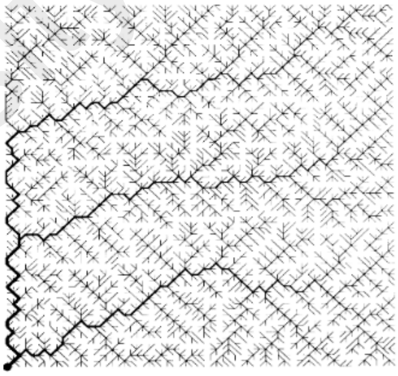

Figure 2.17: River networks show fractal and multi-fractal characteristics (Rinaldo et al., 1993).

2.4 Material Surface Analysis and Characterization

Surface physics is the study of physical changes such as surface diffusion, surface properties, quantum mechanics of electrons that occur at interfaces. Surface science is crucially important for interface and colloid investigation and has been widely applied

University of Malaya

in different fields, which includes biomedical field, as shown in Figure 2.18 (Friedrichs et al., 2007; Meyer et al., 2010; Valencia-Lazcano et al., 2013), calcite surfaces (Karoussi et al., 2008), mineral surfaces as shown in Figure 2.19 (Filby et al., 2012), surface engineering (Zabat et al., 2015), metal engineering (Yin et al., 2015; Pea et al., 2016), solid nanoparticles (Domenici et al., 2016), nanoporous films (Oyarzún et al., 2016), wear surface (Furustig et al., 2016), polymer (Švanda et al., 2016), thin films as shown in Figure 2.20 (Mohan & Sunandana, 2013; Bui et al., 2015) and etc.

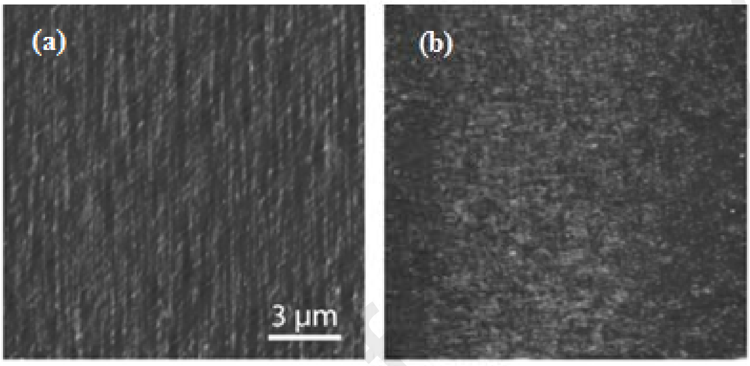

Figure 2.18: Cellular remodelling of (a) periodic and (b) non-periodic collagen cells (Friedrichs et al., 2007).

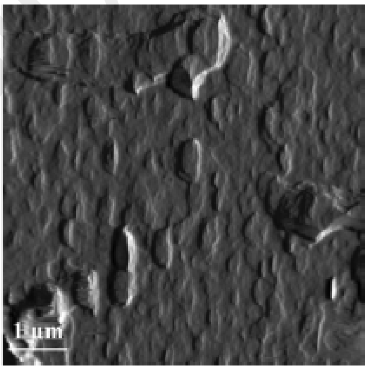

Figure 2.19: AFM image of carboxylated latex colloids interacting with mineral surfaces (Filby et al., 2012).

University of Malaya

Figure 2.20: The AFM study of structurally disordered Ag(Sn)I thin films (Mohan & Sunandana, 2013).

University of Malaya

Morphologies can be studied with Atomic Force Microscopy (AFM), Scanning Electron Microscopy (SEM), and Transmission Electron Microscopy (TEM). In this study, AFM images have been used and this characterization technique will be briefly described in this section. The microscopic surface texture has been widely described by conventional surface roughness descriptors such as Roughness Average (*Ra*) and Root Mean Squared (RMS), which measure the surface height, peaks and valleys. There are other three surface roughness descriptors such as power spectral density (PSD), semivariograms and fractal box counting method will also be discussed in this section. These surface profile measurements illustrate on how the charge carriers possibly interact with its environment and also its effect on the overall device performance.

2.4.1 Roughness and Root-Mean-Squared Height Fluctuation

Roughness represents small, finely-spaced deviations from nominal surface which is determined by material characteristics and processes that formed the surface, as shown in Figure 2.21. Large deviation indicates rougher surface while small deviation indicates smoother profile.

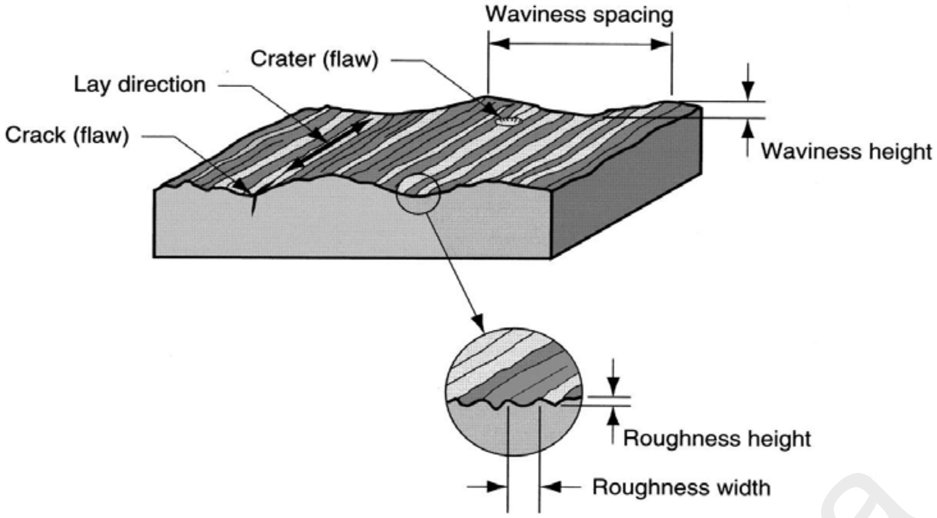

Figure 2.21: Surface texture with large deviation indicates rougher surface while small deviation indicates smoother profile (Kalpakjian & Schmid, 2008).

Waviness is the deviations of much larger spacing that occur due to work deflection, vibration, heat treatment, and similar factors. The spacing of the waviness is larger than the roughness width and typically periodic in nature. Roughness is superimposed on waviness. Lay is predominant direction or pattern of the surface texture. Flaws are the irregularities that occur occasionally on the surface, includes cracks, scratches, inclusions, and similar defects in the surface. Although some flaws relate to surface texture, they also affect surface integrity.

Surface roughness descriptors are the statistical parameters that give average behavior of the surface height or the vertical deviations of the surface roughness from the mean line. For example, average roughness (R_a), the root mean square roughness R_q or (R_{RMS}), the skewness (R_{sk}) and the kurtosis (S_k). There are extreme value descriptors that depend on isolated events such as the maximum peak height (R_p), the maximum valley height (R_v), and the maximum peak to valley height (R_{max}).

Average roughness (R_a), is the arithmetic average departure of the profile from the mean line, and is defined as

$$R_a = \frac{1}{l}\int_0^l z.dx \tag{2.3}$$

University of Malaya

where l is the sampling length and $z = f(x)$ is the profile height as a function of the distance, x, along the surface.

The root-mean-squared (RMS) deviation of the surface, R_{RMS}, is standard deviation that represents the square root of the second moment about the mean of the probability distribution. In other words, it is the square root of the average of the profile height deviations squared from the mean line within the sampling length l, and is defined as

$$R_{RMS} = \sqrt{\frac{1}{l}\int_0^l z^2.dx} \quad (2.4)$$

RMS roughness has been used in analyzing the morphological change of bio-mechanic field. For instance, oxidative stress level has been reported to be higher with a increase in cell membrane roughness (Wang et al., 2011). The study has confirmed the occurrence of cell apoptosis due to the morphological roughness change on cell membranes. At the same time, the importance of studying surface roughness by using different approaches has been emphasized to understand the topology properties, such as physico-chemical properties as surface charge and hydrophobicity or surface free energy (Mendez-Vilas et al., 2007), as shown in Figure 2.22.

University of Malaya

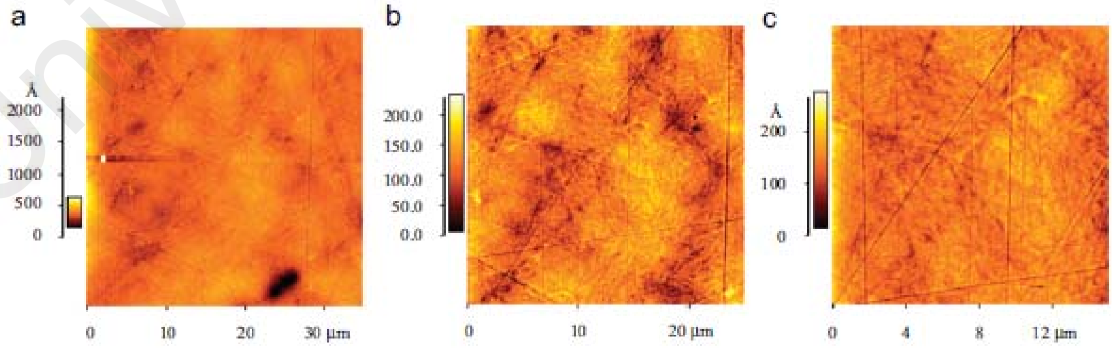

Figure 2.22: AFM images of different surface roughness of the Ti alloy at different length scales (Mendez-Vilas et al., 2007).

RMS roughness has been widely applied in applied surface science, for example, the results of rms roughness with the SIMS beam induced roughness (BIR) have been compared to study the presence of defects in monocrystalline silicon (Fares et al., 2006). In their work, the SIMS results have been correlated with AFM measurements of the root mean square roughness in craters of different depths.

However, there are limitations of interpreting rms roughness for further information and characteristics of the material surface (Dash et al., 2009; Kong et al., 2014). The total effective interface area and the conventional approach such as the spatial indicator based on root mean squared of height fluctuation are among the common parameters often used to corroborate device performance upon modifying surface properties, even tough it provides limited information on the localized features. Thus, alternative measures have been introduced to characterize the surface properties, such as power spectral density, two-point correlation function or variogram, and, of course the fractal parameters, such as Hurst exponent, Holder exponent, and fractal dimension, which will be described after this section.

University of Malaya

2.4.2 Power Spectral Density

Hurst exponent is denoted as H, to measure long-term memory of time series. In fractal geometry, Hurst exponent is directly related to fractal dimension. Fractional Brownian Motion (FBM) with Hurst exponent $0 < H < 1$ provides a powerful tool to generate natural looking fractal graphs and surfaces (Mandelbrot, 1982).

A two-dimensional FBM has a PSD of power-law type with $\gamma = 2H + 2$ in equation $S(k)\sim\frac{1}{k^{\gamma}},$, hence $1 < \gamma < 3$. The noise process associated to FBM or the generalized derivative of FBM is known as fractional Gaussian noise (FGN). FGN is shift-invariant (or stationary) Gaussian stochastic process with power-law correlation function and also has power-law type in the form with $\gamma = 4H - 2$ thus accommodating $0 < \gamma < 2$ for $\frac{1}{2} < H$

< 1. The fractal dimension of the graph is then given by $D_{\mathrm{PSD}} = 3 - H$. The fractal dimension is directly related to the Hurst exponent, where small Hurst exponent contributes to rougher surface with higher fractal dimension, and vice versa, as shown in Figure 2.23.

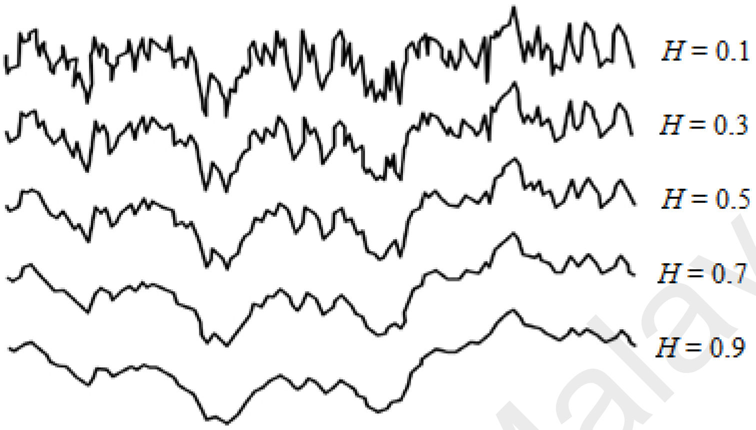

Figure 2.23: Hurst exponent and Fractional Brownian Motion (FBM) (Kwan et al., 2012).

The surface morphology of a thin film can be studied and efficiently characterized by PSD method. This technique is useful for characterizing complex multi-scale features as compared to the standard measure of surface roughness based on root mean squared fluctuation of height fluctuation. Fractal parameters from the geometry surface models were then linked to electrical conductivity of thin films that used for fabricating organic photovoltaic devices (Monemdjou et al., 2014). The method starts with the surface morphologies of the organic thin films scanned by atomic force microscopy and the fractal dimension of each film is then determined from the AFM data by using PSD with fast Fourier transform (FFT) function. As the fractal dimension of the thin film image increases, the conductivity of the photovoltaic device increases as well. This result has encouraged the fractal dimension analysis for morphological images that allows more detailed 2D descriptors to reflect of surface roughness and heterogeneity.

University of Malaya

The thin film morphology and electrical properties are crucially related to each other to enhance the overall device performance (Itoh & Yamauchi, 2007). In their study, the pentacene films have been formed on glass and Au under-layer by thermal evaporation. The pentacene film growth were characterized by the PSD method by using fast Fourier Transform algorithm and k-correlation model has been applied to describe the function parameters, as shown Figure 2.24. The surface irregularities has been evaluated by using fractal dimension value and the bulk diffusion was interpreted by the power values of PSD.

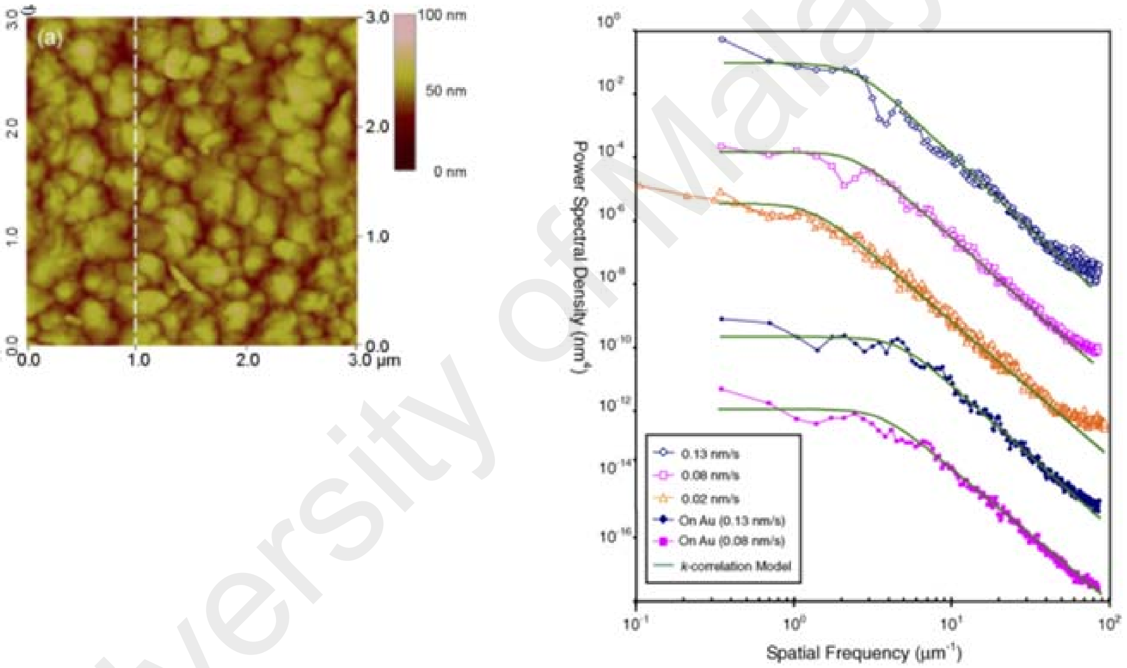

Figure 2.24: (left) AFM image of pentacene surface of evaporation rate 0.13 nm/s on glass substrate, (right) PSD plots of pentacene films at different evaporation conditions on glass and Au layer (Itoh & Yamauchi, 2007).

Gadolinium oxide thin films have been studied and well characterized by power spectral density functions (Senthilkumar et al., 2005). In their observation, higher substrate temperature contributes to the presence of larger similar grain size over the surface which influences the charge mobility in the film growth. They also suggested that the surface morphology of the thin films exhibited fractal behaviour at higher spatial frequency region of the PSD spectrums and the aggregates were then represented

University of Malaya

by low frequency components which dominantly contributes to the overall surface roughness, as shown in Figure 2.25. At the same time, the authors concluded that the fractal components are highly correlated with the refractive index of the films.

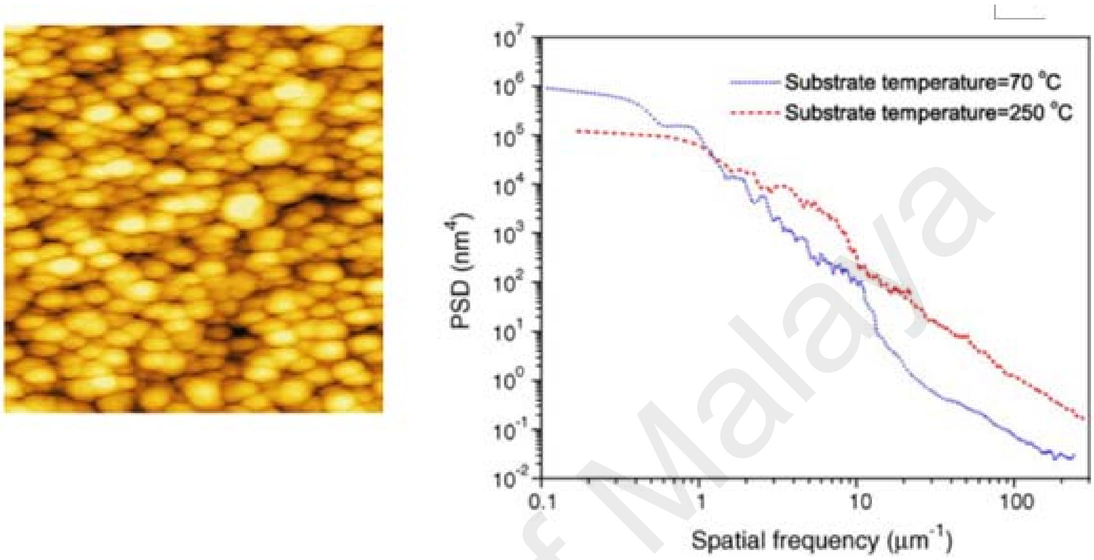

Figure 2.25: (left) AFM image of gadolinium oxide films deposited at the substrate temperature of 250°C, (right) PSD plots of gadolinium oxide films at different deposition temperature (Senthilkumar et al., 2005).

University of Malaya

The power spectral density of the surface topology transforms the morphological images into different spatial frequency ranges to describe the surface roughness of the profile. Overall, all PSD curves performs flat plateau in the lower spatial frequency region and a power law roll-off in the higher spatial frequency region of the spectrum. The further study of PSD spectra provides qualitative understanding of the morphological parameters and its effects on different specific fabrication conditions (Gavrila et al., 2007). This PSD analysis has been suggested as one of the effective method in quantifying the fiber alignment and macroscopic architecture features (Ayres et al., 2006).

As shown in Figure 2.26, indium tin oxide (ITO) thin films were deposited by electron-beam evaporation technique on glass substrate at room temperature and at different annealing temperature (Raoufi, 2010). In their work, the surface morphological study has been carried out by using PSD method to provide information about optical characterization and the surface roughness of the ITO thin films. They reported that the surface roughness increases with higher fractal dimension. The detailed description of the irregularities found in the ITO thin films provided by PSD study had further explained the influence of the annealing temperature onto the interface width and lateral correlation length (Raoufi et al., 2007).

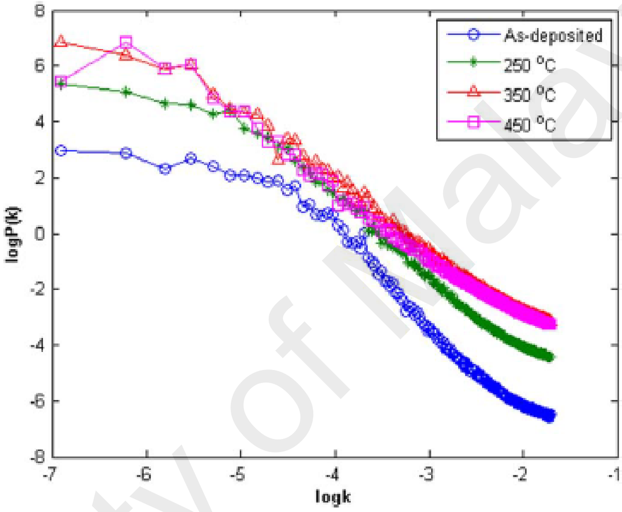

Figure 2.26: PSD method has been used to study the morphological surface of indium tin oxide thin films which were deposited at different annealing temperature (Raoufi, 2010).

FBM is a fractal process but it cannot be used to generate shift-invariant homogeneous (or stationary) surfaces as the process only has increments stationary. However, one may opt to use FGN instead of FBM. In order to generate stationary surfaces with fractal properties, one needs a concrete Gaussian process (or random field) that accommodate dual-fractal properties, namely power-law scaling in the local growth (variance) and in correlation function, with independent scaling parameters. An example of such as a stochastic process is known the generalized Cauchy process (Gneiting &

University of Malaya

Schlather, 2001) characterized by the correlation function with spatial lag (*h*), which will be described in next section.

2.4.3 Semivariograms

Surface roughness or spatial continuity can be characterized by the variogram. Analysis starts with experimental variogram which is calculated from the data and then fitted with a suitable variogram model.

The variogram analysis has been widely applied in geo-statistics field to determine spatial random variables for mineral resource estimation (Sadeghi et al., 2015), element concentration in soil (Kerry & Oliver, 2011), the shear resistance of rock (Roko et al., 1997), hydrology (Voss et al., 2016) and others (Zorzi et al., 2008). The variogram is a theoretical function that are not the real properties of the data, but it is useful to help us to understand the complexity and to predict the conditions at random or unvisited point. Experimental variogram for a particular separation vector of interest is determined by averaging one half the difference squared of the z-values over all pairs of observations at lag distance. It is plotted as a two-dimensional graph, as shown in Figure 2.27.

University of Malaya

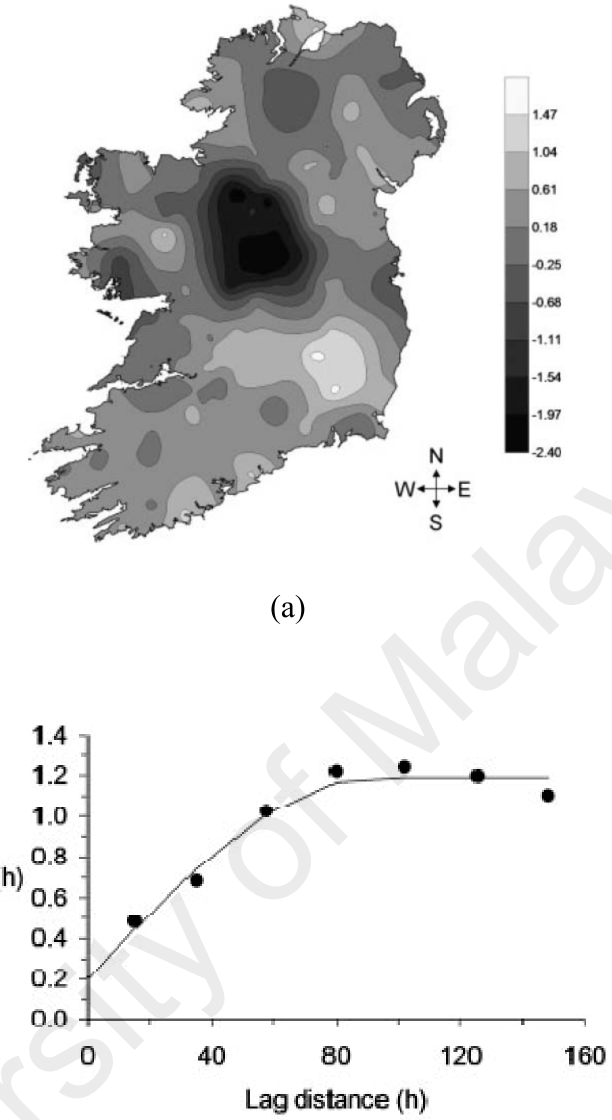

(a)

(b)

Figure 2.27: (a) Contour map A, (b) variogram and model for contour data A (Relethford, 2008)

University of Malaya

The variogram values increase with increases in the distance of separation until it reaches the maximum sample variance, as shown in Figure 2.28. The slope of the beginning part of the variogram model represents the range or the structural part of the variogram model.

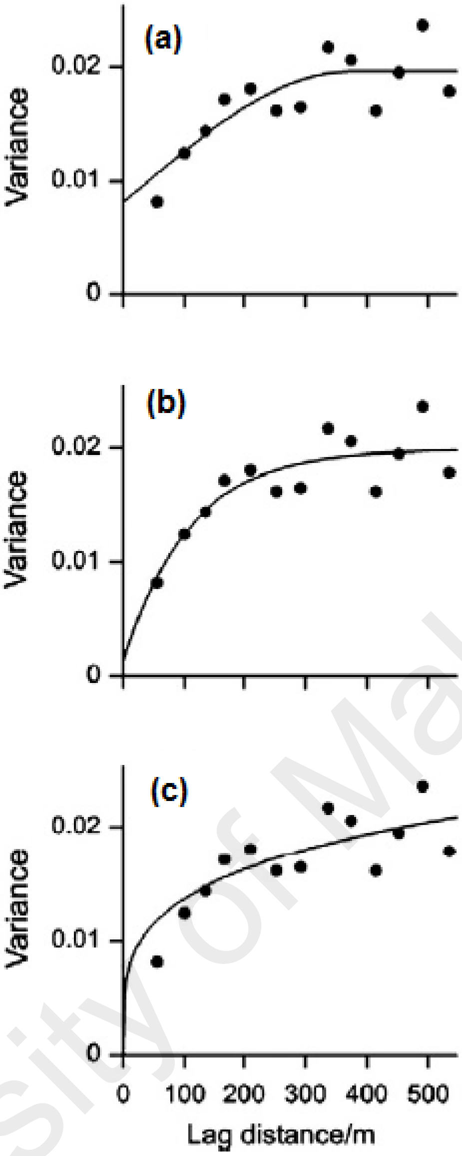

Figure 2.28: The variogram model from suitable mathematical functions is selected to describe the spatial relationships, (a) spherical model, (b) exponential model, and (c) power function (Oliver & Webster, 2014).

For example, the resulting morphological surface changes between electric and non-electric field induced bR layers formed on the Indium Tin Oxide (ITO) conductive slides has been investigated from the empirical semi-variograms with least square fitted model covariances based on generalized Cauchy process (Vengadesh et al., 2009), as shown Figure 2.29. In their work, model parameters α (fractal scaling), β (long-range dependence exponent (LRD) properties), σ^2 (variance of the process) are extracted from GCP to describe the morphological cluster distributions of bR protein. Fractal

University of Malaya

dimension and the Hurst exponent are then estimated to investigate local distribution of bR protein and their spatial correlation.

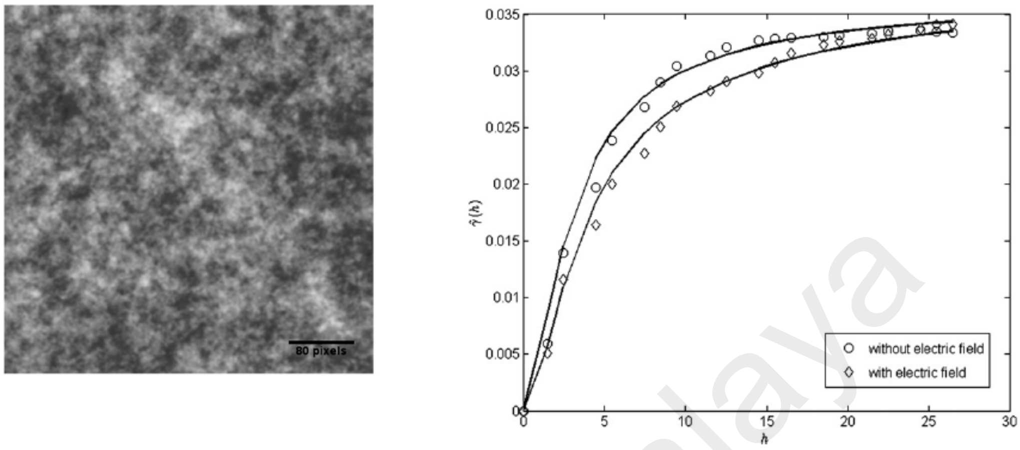

Figure 2.29: (left) AFM images of electric field assisted bR film, (right) Empirical semi-variograms and the least square fitted model covariances based on generalized Cauchy processes (Vengadesh et al., 2009).

In geospatial and agricultural application, semivariogram analysis has been adopted to quantify the heterogeneity of the topology. For instance, soil roughness changes due to rainfall had been tabulated and analyzed by using semivariogram method (Rosa et al., 2012). On the other hand, semivariograms have been used to analyze the heterogeneity of the distribution elements with periodic patterns in remotely sensed images (Balaguer-Beser et al., 2013). In their work, successful evaluation of several parameters such as distribution of elements, size and faults from the semivariograms helps to characterize the heterogeneity of a topology. This means that the same potential application can thus be used in many other pattern recognition fields particularly in microstructure morphological study, whereby the distribution of charge carriers, grain sizes, morphological defects can be analyzed and well-described accordingly.

University of Malaya

2.4.4 Fractal Box-Counting Method

The famously used box-counting technique is used to quantify the fractal dimension of a topology which describes the surface properties and enhance the profilometric analysis, and the image processing sequences have been shown in Figure 2.30. In material science such as microstructure morphological study of thin films, fractal dimension is crucial to reveal the surface roughness of the active layer to describe further the mechanical properties.

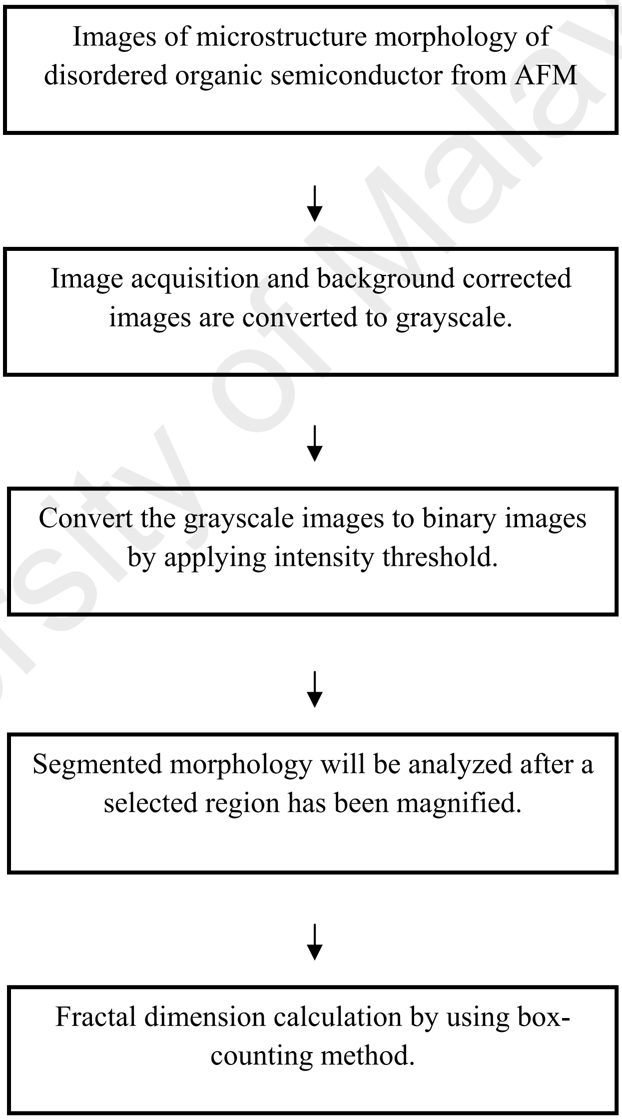

Figure 2.30: Flow chart shows the extraction of fractal dimension from box-counting method.

University of Malaya

The use of box-counting method has been demonstrated to analyze the scattered data (Buczkowski et al., 1998). The log-log plot, as shown in Figure 2.31, has been divided into three regions for separate fractal dimension calculation, where N_ε is the number of boxes needed to recover the object and ε is the side length of the box. The distribution density of a discontinued object can be predicted from the dimension obtained from the middle part of the graph (labelled as region 3 in the graph). The fractal dimension of the substructures is extracted from region 2 while the dimension of the total area obtained from region 1 of the graph. This means that BCM enables the estimation of dimensions of an object at different scales.

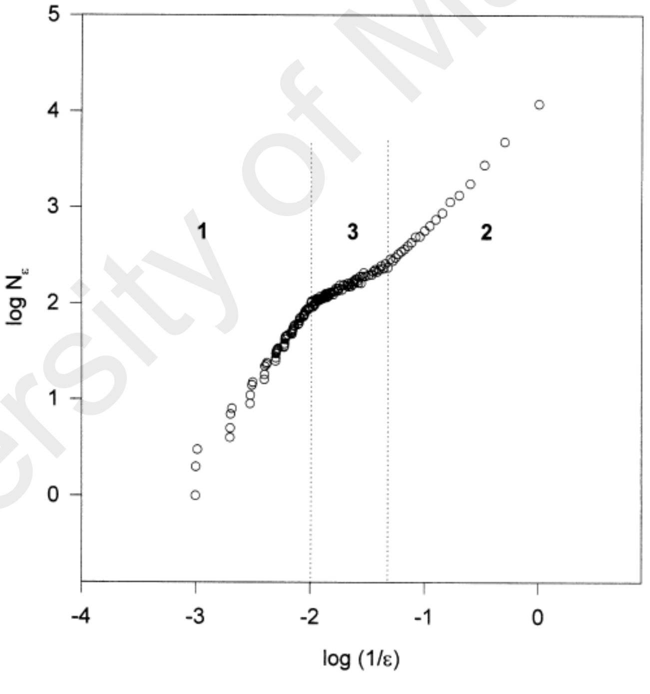

Figure 2.31: Scattered data on a log-log plot, which has been categorized into three regions to be analyzed (Buczkowski et al., 1998).

However, BCM might be limited for deterministic fractals whereby only one data point available. At the same time, the accuracy of this method decreases to calculate the fractal dimension of an image with arbitrary size $M \times N$ pixels. Therefore, there are many who suggest their improved BCM method to overcome these limitations. For

University of Malaya

example, the application of integer ratio based box-counting method has been recommended, which is applicable to arbitrary images (Long & Peng, 2013). The proposed method has reflected better surface roughness analysis of images and contributes to higher accuracy of fractal dimension value.

On the other hand, the improved BCM method has been proposed to overcome the drawbacks by well-known differential box-counting method (DCM) (Li et al., 2009). These drawbacks include the limitations of box height selection, least box number calculation, and discontinuous image intensity surface partition. They claimed that their suggested method has improved the inaccuracy of getting the fractal dimension by using the smallest number of boxes to cover completely the entire image at specific box dimension.

The microstructure morphology of polymer-oxide thin films has been studied by using fractal analysis (Ţălu et al., 2015). The result in their work has suggested that fractal dimension provides additional insight of the detailed geometrical patterns variations during casting. From there, the other mechanical properties such as stiffness, viscosity and thermal stability can be further investigated.

Surface characterization by using fractal parameters through box-counting method (Kulesza & Bramowicz, 2014) has concluded that the method provides information about the kinetics of the deposition process of the polycrystalline diamond films. The fractal dimension has been reported significantly decreases as the surface starts to etch together and forms a smoother ground. However, the method has been limited to scan size of images and critical grain size, which might resulted in inaccurate fractal dimension estimation.

The methodology of PSD and GCP models, box counting method, fractal spectrum and percolation theory will be explained in details in Chapter 3.

University of Malaya

CHAPTER 3: METHODOLOGY

The material preparation, the process of image acquisition and pre-processing details are described accordingly in this chapter. At the second part of this chapter, the methodology of PSD and generalized Cauchy process models, box counting method, fractal spectrum and percolation theory have been further investigated and explained. The dual-fractal parameters (GCP) is related for the first time to charge transport properties by measuring the short-circuit current density (J_{sc}) of the OPV with surface treatment.

3.1 Material Preparation

3.1.1 Active Layers

As mentioned in Chapter 2 earlier, the microstructure of the active layer plays an important role in determining the performance of a photovoltaic device.

A bulk heterojunction of the donor-acceptor allows the charge to diffuse at minimal length and shorten the time of dissociation process. In other words, large interface area for exciton dissociation will promote higher photocurrent (J_{sc}), measuring in unit of μA/cm^2 which appears to be one of the factors to characterize the overall performance of the photovoltaic device. An example of typical solar cell structure has been shown in Figure 3.1.

University of Malaya

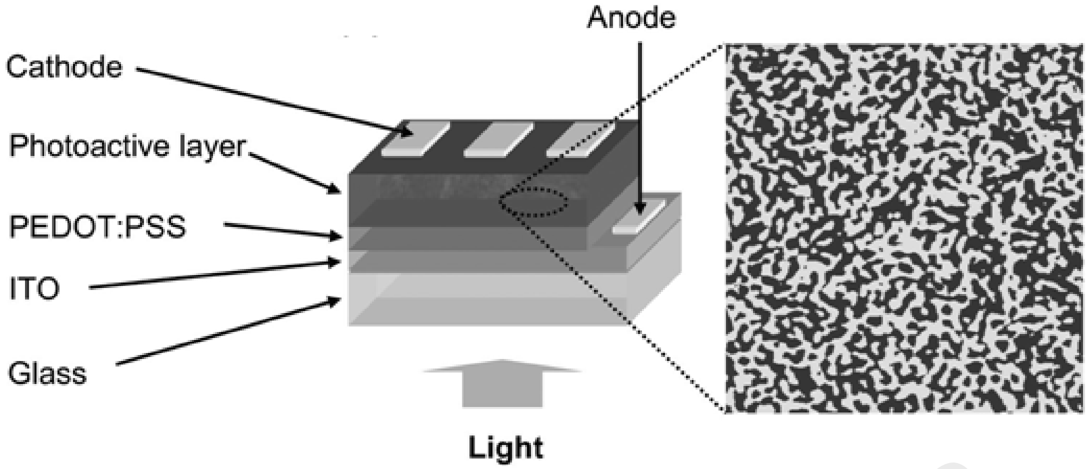

Figure 3.1: An example of typical solar cell structure consisting of Poly(3,4-ethylenedioxythiophene) polystyrene sulfonate (PEDOT:PSS) deposited onto a glass/ITO substrate (Dang & Nguyen, 2010).

University of Malaya

In this study, there are two set of AFM images have been studied, whereby the first set of thin films was treated using same solvent over different durations, and the other set of thin films was processed with different solvent treatment.

For first set of thin films, organic nickel (II) phthalocyanine-tetrasulfonic acid tetrasodium salt (TsNiPc) is used as the solution and commercially available glass slides are used as the substrates are used in this study. The glass slides are subsequently cleaned using acetone, isopropyl alcohol and de-ionized water for purification purpose. TsNiPc powder is dissolved in de-ionized water to obtain TsNiPc solution with a concentration of 35 mg/ml. As indicated by a surface profiler meter, 100 nm thick TsNiPc films are coated onto the glass substrate using spin coating technique. The spin-coated TsNiPc layer is then annealed to 140°C for drying process to remove the water content.

For surface treatment, chloroform is chosen due to its very low solubility of TsNiPc powder. The thin films are then immersed in the chloroform as solvent for 40 minutes, 80 minutes and 120 minutes. Microfibers with average width not more than 200 nm are formed from the solvent treatment. At the same time, an untreated thin film is reserved for comparison as control specimen. The thin films are then carefully dried under ambient condition. The effect of immersion duration on the morphology and the mobility of charge carriers are investigated by incorporating the TsNiPc films with tris(8-hydroxyquinolinato) aluminium (Alq3) on the electrical properties.

For second set of thin films, organic nickel tetrasulfonated phthalocyanine (NiTsPc) films are immersed separately in chloroform and toluene solvents for same immersion time of 20 minutes. NiTsPc has been chosen as the target of study because it can be fully dissolved in de-ionized water in order to utilize spin-coating method for film deposition. The photovoltaic devices are fabricated by depositing Tris(8-hydroxyquinolinato) aluminium (Alq3) as n-type material on top of the solvent treated NiTsPc film. Alq3 is selected as an acceptor material since its highest occupied molecular orbital (HOMO) and lowest unoccupied molecular orbital (LUMO) are well-matched with NiTsPc. The electrical properties of the device are measured. From the observation, the device using NiTsPc film treated with chloroform produce a better electrical performance (high photocurrent density) as compared to NiTsPc treated with toluene, by referring to the *IV* graph as shown in Figure 3.2. Thus, chloroform is used as the poor solvent throughout this work (poor solvent is defined as the solvent which has low solubility to the NiTsPc material). During the immersion process, the solvent molecules are absorbed into the thin film layer, and then evaporated during the drying process. It is expected that the modification of the film surface does not occur during the immersion process. The film has started to aggregate and align during the evaporation of solvent or the drying process. The vapor pressure of toluene and chloroform is 22 mm Hg and 159.8 mm Hg, respectively.

Keithly 236 Source Measurement Unit (SMU) was used to measure the as-fabricated devices with arrangement ITO/NiTsPc/n-type material/Al in a controlled environment. ITO and Al electrodes were connected to anode and cathode respectively at the SMU

University of Malaya

before taking the measurement. The sample holder, the electrical probe and the light source were placed in a black box with the background light eliminated. Characterization under light illumination was done using an Oriel solar stimulator (model 67005 with Air Mass 1.5 filter) under standard conditions with a white light irradiation at 100 mW/cm^2 to simulate the irradiation of light from the sun. The voltage was set to be at range – 1.0 to 1.5 V in order to detect the photovoltaic effect which occurred at the 4th quadrant of the current-voltage curve. The response time was set to 1 μs to match the typical mobility of electron in organic material. The measurement of photocurrent (*Jsc*) and voltage of the device were taken by a personal computer, equipped with a LabVIEW system design software.

Surface morphologies of the both sets of organic thin films are then studied by using atomic force microscopy (AFM).

3.1.2 Charge Density Measurement

The conductivity of the thin film is the measure of a material's ability to conduct electric current, whereby the conductivity increases with higher charge density. The relationship between the amount of photocurrent (electrons) that facilitate across the terminals with a certain applied voltage can be described by a graphical curve called the IV (Current-Voltage) curve. The IV curves is often characterized under illuminated conditions and the reverse bias readings of a solar cell is obtained under dark conditions. The conversion efficiency and maximum power of a solar cell device can be determined.

University of Malaya

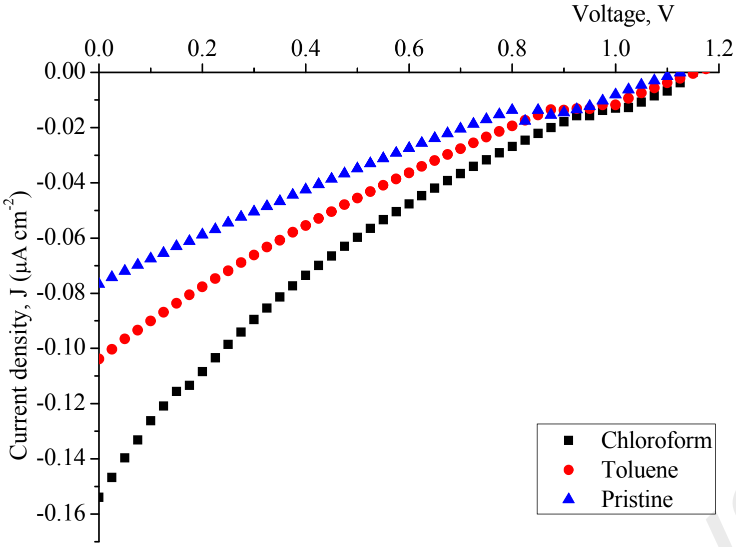

Figure 3.2: The current density – voltage (*J-V*) characteristics of ITO/NiTsPc/Alq3/Al and ITO/treated NiTsPc/Alq3/Al devices under light illumination, for thin films set 2.

University of Malaya

For both sets of thin films, a computer system with a Keithley 2400 or 236 digital source meter is used to control the applied voltage and the resulting photocurrent amount has been recorded. The voltage range was swept through in little steps of 10 mV. A voltage usually in the range between –2 to 2 volts is applied to the solar cell diode which is placed in an argon glove-box system. IV-curves readings are measured in the dark condition whereby parameters such as parallel resistance and breakdown region of the solar cell can be calculated. Otherwise, a solar simulator (Steuernagel 575) can be used to simulate AM 1.5 solar irradiation, with light intensity selection varies from 80 to 100 mW/cm^2, to obtain the readings. The conversion efficiency and maximum power of a solar cell device can be determined.

On the other hand, photoluminescence (PL) is often used to represent charge transfer within the thin film. It indicates a better charge transfer across the interfaces when the intensity is decreasing. The reduction in PL intensity, known as PL quenching, represents an efficient charge transfer at the donor-acceptor interface. The quenching phenomenon was observed when the films were treated with different solvent. For thin film set 2, charge was transferred from the donor (NiTsPc) to the acceptor (Alq3).

3.2 Image Acquisition & Pre-processing

For thin films set 1, surface morphologies of the organic thin films are studied using atomic force microscopy (AFM) for the untreated and the solvent treated samples at 40 minutes, 80 minutes and 120 minutes immersion. The scan size of the thin film is 10 µm × 10 µm with elevation map scaled to surface height range of 100 nm, as shown in Figure 3.3. Five processed images of 400 ×400 pixels for each stage are sub-sampled from the parent images, as shown in Figure 3.4. The image processing software used in this study are *ImageJ* and *MATLAB*.

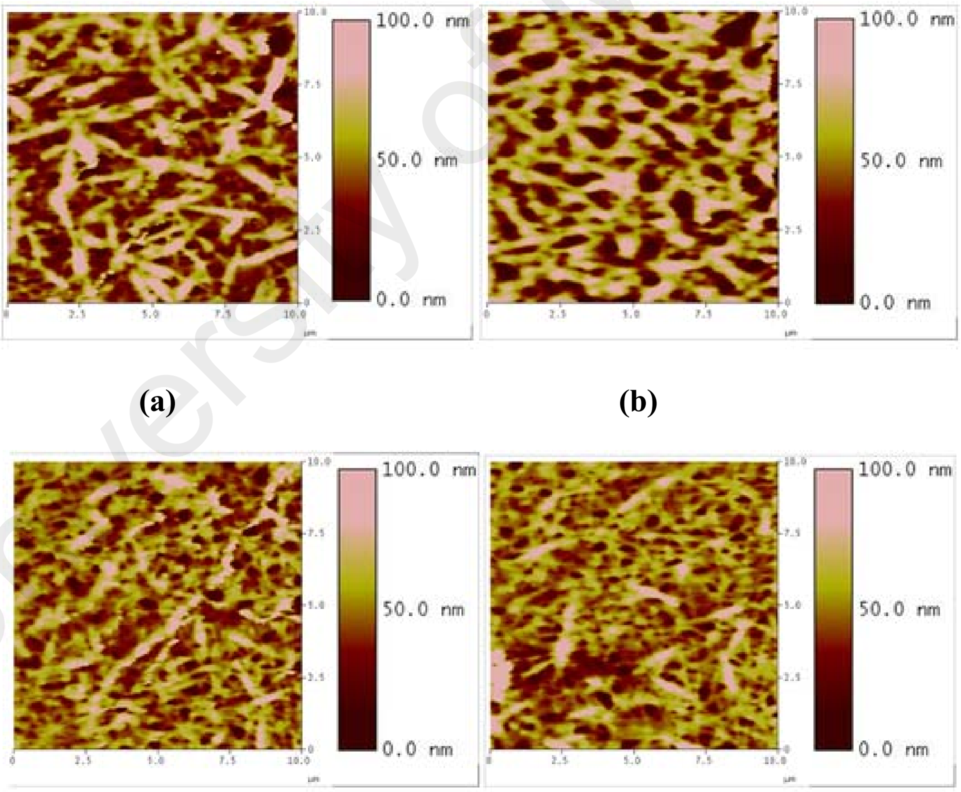

(a) **(b)**

(c) **(d)**

Figure 3.3: Unprocessed AFM original images of thin films set 1 (a) untreated sample and treated samples at different solvent immersion times of (b) 40 minutes (c) 80 minutes, and (d) 120 minutes.

University of Malaya

The color image is first converted to 8-bit grayscale and then processed under different stage of thresholding conversion to eliminate the shadowy region due to the minor unconnected clusters or other topographical irregularities. Grayscale image consists of intensity information in each pixel ranged from 0 to 255 different intensities, where intensity of 0 has been categorized as black and 255 as white. The main motivation here is to visualize the clustering contours effect that indicates the formation of percolative network, which is represented by the density of fibrous components spanning the module at different gray levels. Grayscale morphological reconstruction is able to reduce noise in the image in order to obtain clear textural information for further analysis (Yu & Tan, 2009).

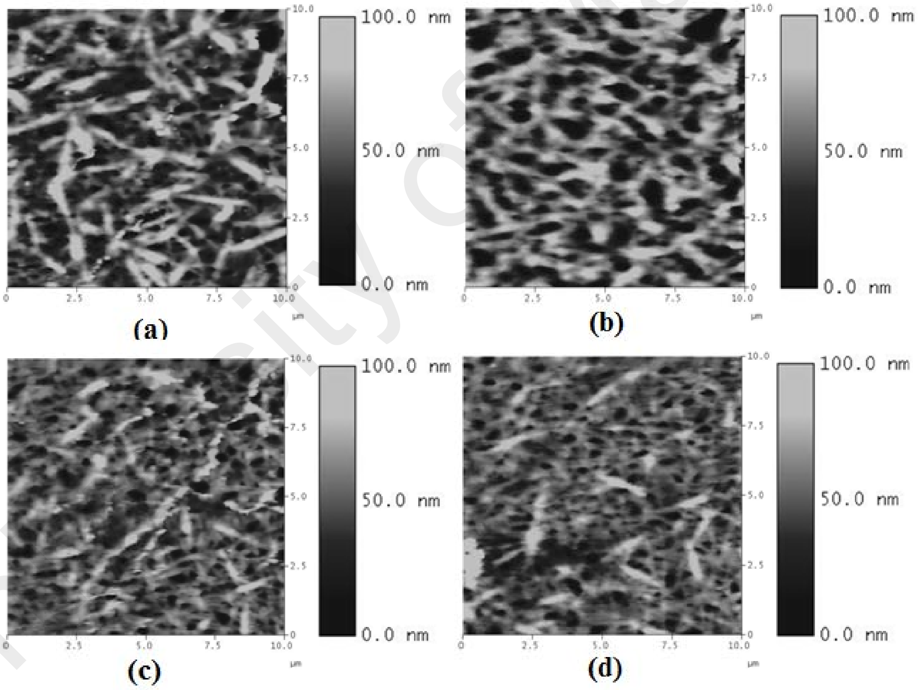

Figure 3.4: Processed AFM images of thin films set 1 (converted to grayscale): (a) untreated sample and treated samples at different solvent immersion times: (b) 40 minutes (c) 80 minutes and (d) 120 minutes.

Intensity-based image segmentation is used to segment the object from background and allows isolation of an area of interest for further connectivity study. This method has been applied in biomedical field (Mashiah et al., 2008), tissue engineering (Ayres et

University of Malaya

al., 2006), rock physics (Bagde et al., 2002) and thin films (Raoufi, 2010). Thresholding technique is often used for image segmentation that transforms an image into black and white (BW) or binary image that separate the object of interest from the background. The input image can be grayscale or color. The segmentation process will convert all data points below a certain threshold to zero and data points above that threshold to one. Therefore, pixels which are categorized as black has similar grayscale of multivariate values that share certain topological characteristics to form a connected region. Thus, it shows the probability distribution of image intensity and correlation between pixels, which later to be analyzed by using fractal dimension method.

As shown in Figure 3.5, five processed images of 400 × 400 pixels for each stage are sub-sampled from the parent image of thin film and processed for PSD functions separately. The results are then combined and averaged for higher accuracy.

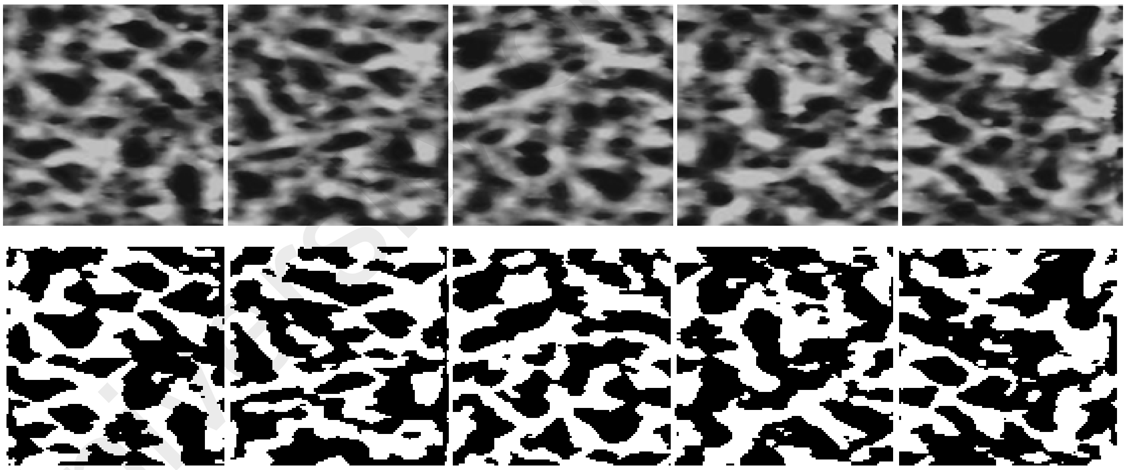

Figure 3.5: In this picture, samples of 40-mins thin films are shown (top five) gray-scaled, (bottom five) thresholded, using image processing toolbox *ImageJ*.

For thin films set 2, the observation of the surface morphology of the treated NiTsPc films is determined using Atomic Force Microscopy (AFM) in a tapping mode of Dimension 3000. The scan size of each thin film is 10 μm × 10 μm with scan rate of 2.001 Hz, as shown in Figure 3.6. Images of 240 × 240 pixels size for each solvent treatment are sampled from the original AFM images, as shown in Figure 3.7.

Universiti of Malaya

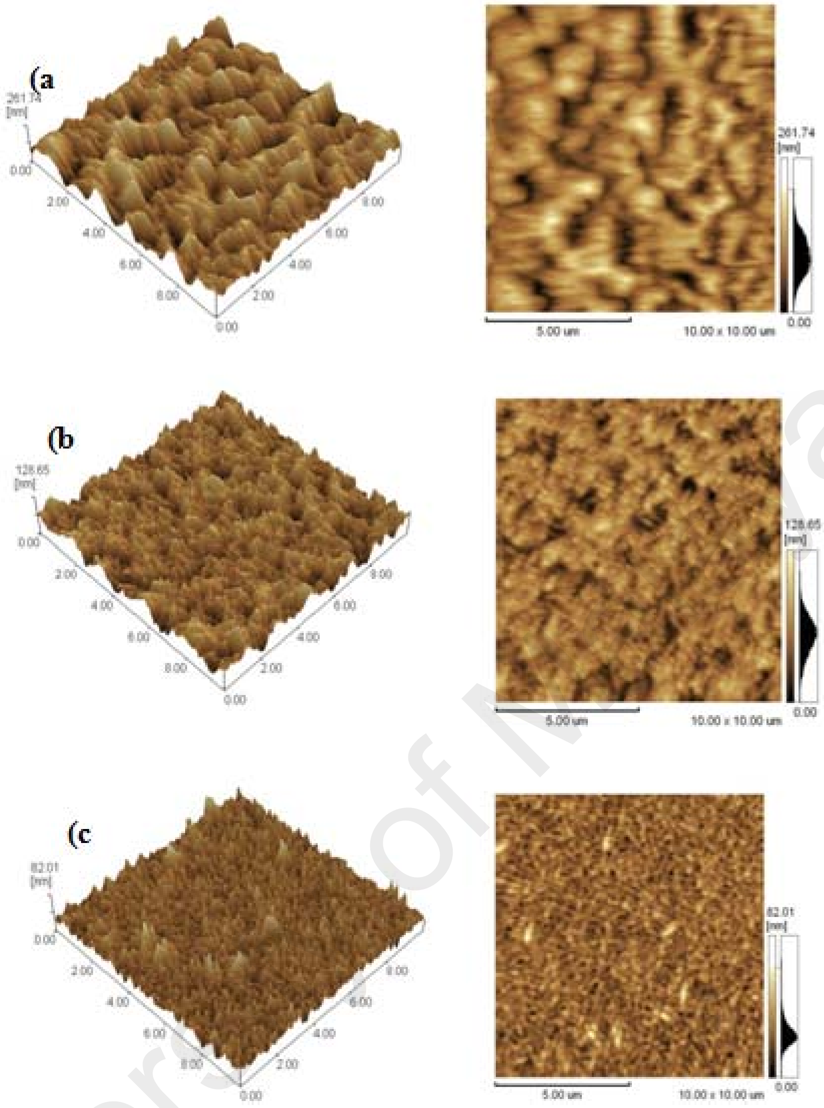

Figure 3.6: AFM images of NiTsPc films in 3-D (on the left) and in 2-D (on the right) for (a) the untreated pristine, (b) treated with chloroform, and (c) treated with toluene.

The untreated thin film (pristine) is reserved for comparison as control specimen. The root mean square (rms) values of the untreated pristine, chloroform treated and toluene treated films are 41.426 nm, 15.902 nm and 8.593 nm, respectively.

University of Malaya

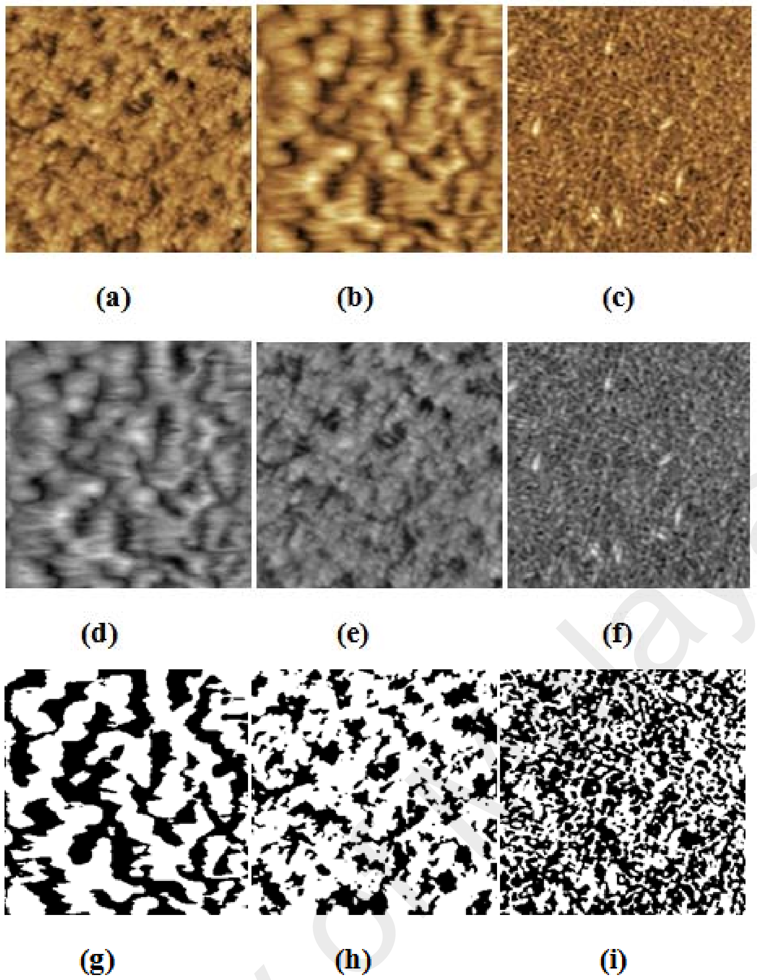

Figure 3.7: AFM images of the second set of thin films for (a)-(c) original & unprocessed (d)-(f) gray-scaled, (g)-(i) thresholded, for untreated pristine (all left), chloroform-treated (all middle), and toulene-treated (all right) films, respectively.

For anisotropic structure, the spatial frequencies will diverge in different direction and the 2DFFT of the image performs elliptical shape. On the other hand, an isotropic structure possesses angular similarity which results in circular and equiaxial shape for its Fourier transform image. This observation has been noticed to be congruent with the results from roseplot analysis whereby the plots are generated by calculating the number of white pixels in each direction from the center of the image (0° to 360°), as shown in Figure 3.8.

University of Malaya

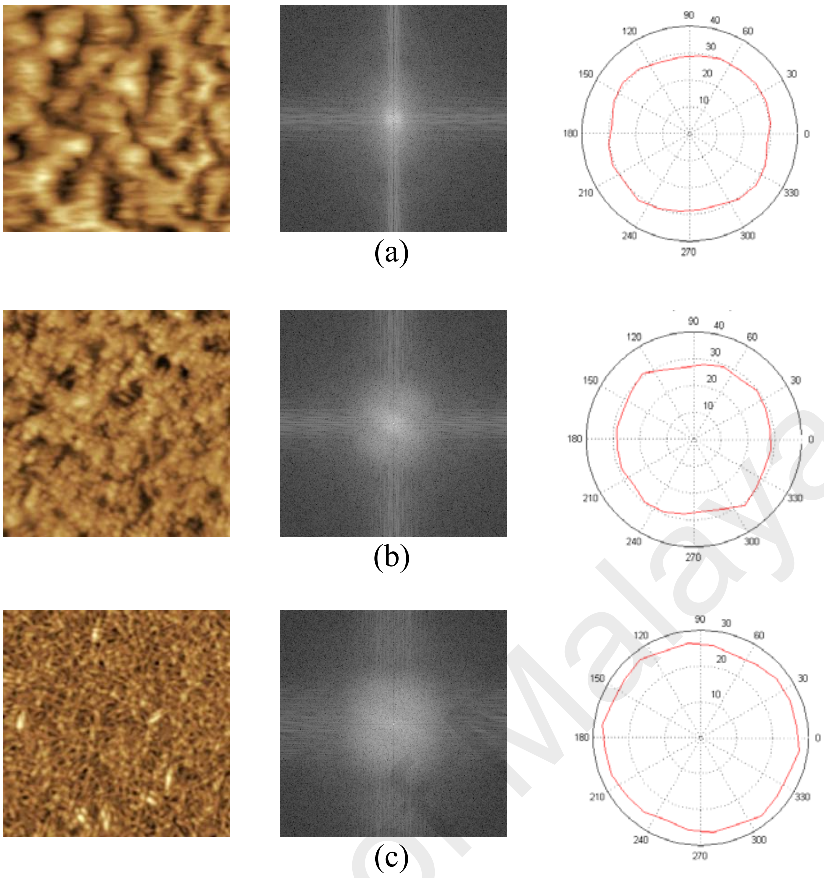

(a)

(b)

(c)

Figure 3.8: Surface image (left), 2DFFT (middle) and roseplot (right) for (a) untreated pristine, (b) chloroform, (c) toluene films.

University of Malaya

Aspect ratio (A_f) is then determined by the ratio of its sides (horizontal and vertical directions) from roseplot, with an increase in A_f indicates the presence of strong anisotropic structure. In this study, the A_f for all three roseplots have been observed to be nearly uniform (equal to 1) which distinctly indicates that the structure is almost isotropic and has no directional dependence.

Three dimensional images have been restructured from the parent images by using *ImageJ* software, as shown in Figure 3.9.

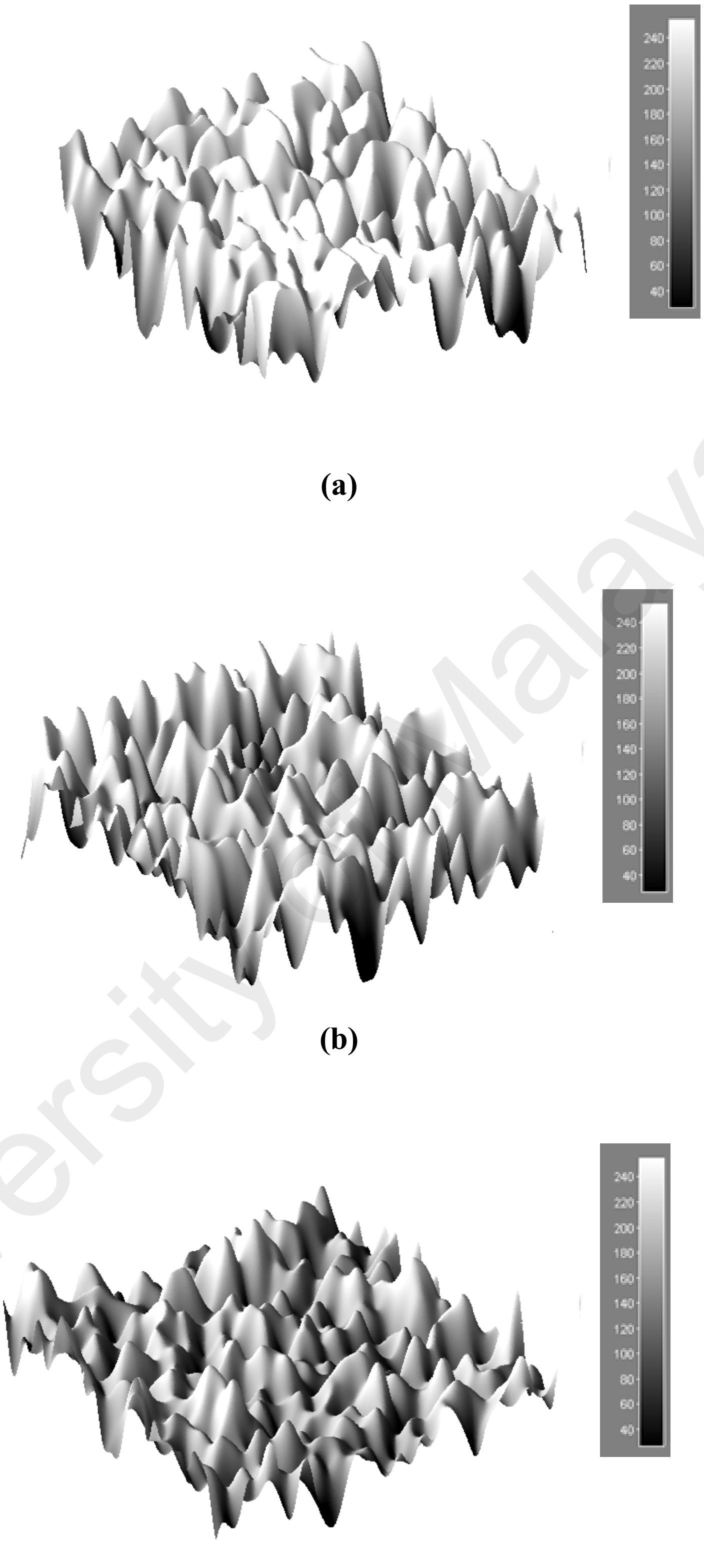

(a)

(b)

(c)

Figure 3.9: 3D surface restructuring from the parent image of AFM images for (a) untreated pristine, (b) chloroform-treated, and (c) toulene-treated films respectively.

University of Malaya

3.3 Surface Morphologies Characterizations

Microstructure morphologies reveal important information of materials properties such as charge carrier mobility, optical absorption and mechanical quality. Fractal texture analysis provides useful surface descriptors that serve as alternative measures of surface roughness and heterogeneity. There are a number of fractal stochastic models such as the fractional Brownian motion and generalized Cauchy models that are widely used in the modelling of material surfaces and their characteristics parameters such the Hurst exponent (and fractal dimension) can be linked to material properties.

In this section, the methodology of surface morphology characterization used in this study will be described and explained, which include power spectral density (PSD), Cauchy process (GCP), box counting method (BCM), fractal spectrum (FS) and percolation theory.

3.3.1 Power Spectral Density

The Power Spectral Density (PSD) measures the distribution of power intensity values as a function of frequency. In other words, it is a positive real function of a frequency variable associated with a stationary stochastic process or a deterministic function which illustrates the signal's power at particular frequency point. PSD is well-established and commonly adopted as the standard technique for surface characterization because it is competent to characterize the amplitude versus frequency content of a random signal. In nano-morphological study, this random signal or pulse like signal could represent disordered and irregular surface structure. PSD transforms the surface profile to different spatial frequency ranges in order to provide the measurement of surface roughness.

PSD has been widely adopted recently in surface roughness study (Lee & Lee, 1995; Vilmercati et al., 2009; Goetz et al., 2009; Qian et al., 2013) because the conventional

University of Malaya

spatial indicator based on root mean squared of height fluctuation (RMS roughness) provides limited information on localized features. Standard representation of an image consists of an intensity value for each spatial coordinate, $Z(m, n)$, which is called as spatial domain.

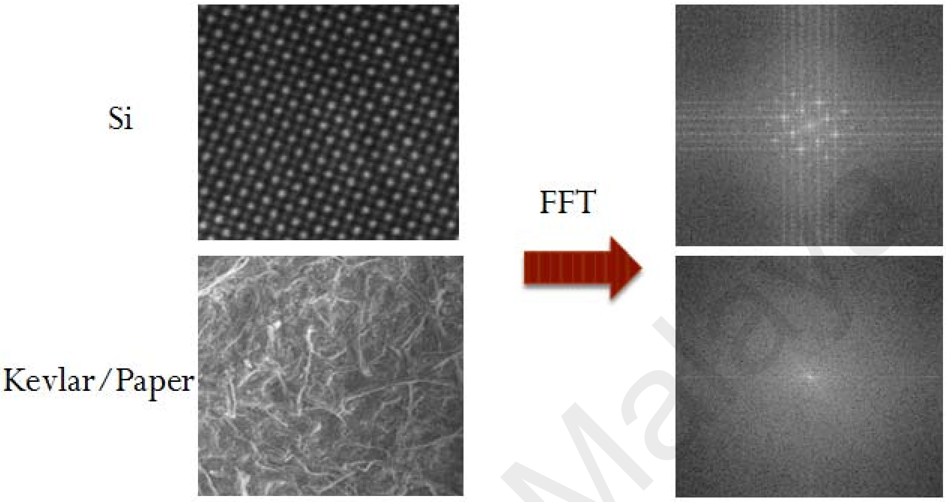

Figure 3.10: Transforming an image into frequency domain using fast Fourier transform (FFT).

Fast Fourier transform (FFT) transforms the original real data images (spatial domain) into mathematically defined frequency domain (spatial frequency), as shown in Figure 3.10. The FFT processed output image consists of grayscale pixels that are distributed in a pattern that reflects the alignment and distribution of fibrous component in the original data image. For example, as shown in Figure 3.11, the randomly distributed fibers contribute to more symmetrical and circular shape of output image.

In contrast, the aligned fibers arrangement results in elliptical shape of output image. The pixel intensities are distributed with a specific orientation, that contributes to the different distribution shape, as shown in the pixels intensity plots in Figure 3.11 (c) and (f) (Ayres et al., 2006). This is particularly important in the measurement of anisotropy model in order to evaluate the material used and its impact to the microstructure morphology.

University of Malaya

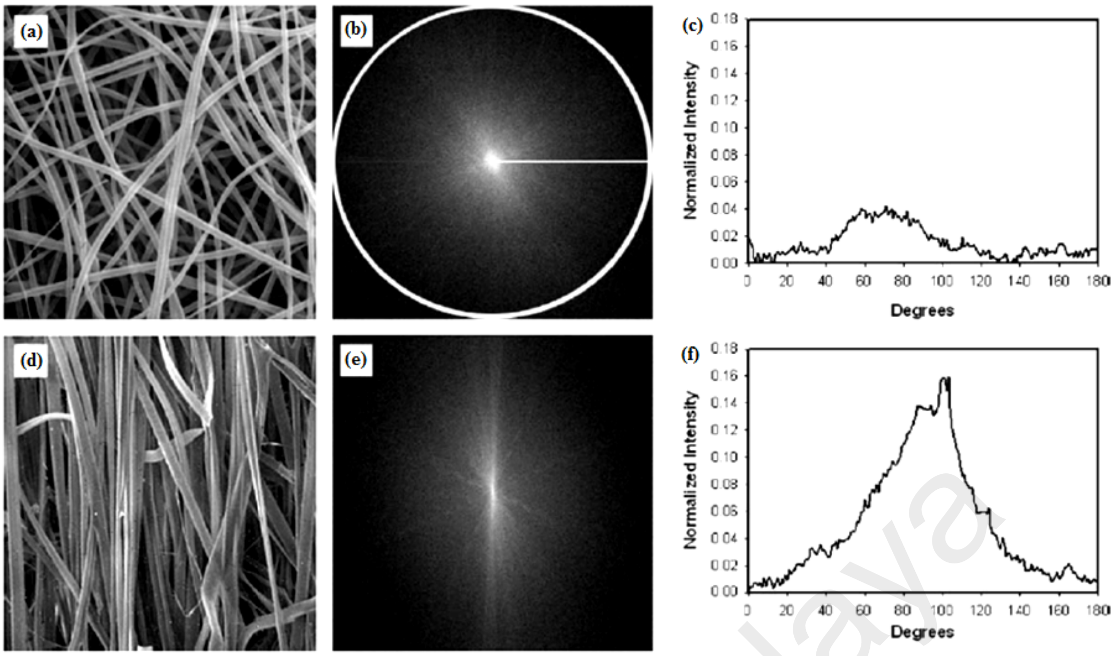

Figure 3.11: (a) and (d) SEM images of fibrous components, (b) and (e) FFT images, (c) and (f) pixels intensity plots respectively (Ayres et al., 2006).

University of Malaya

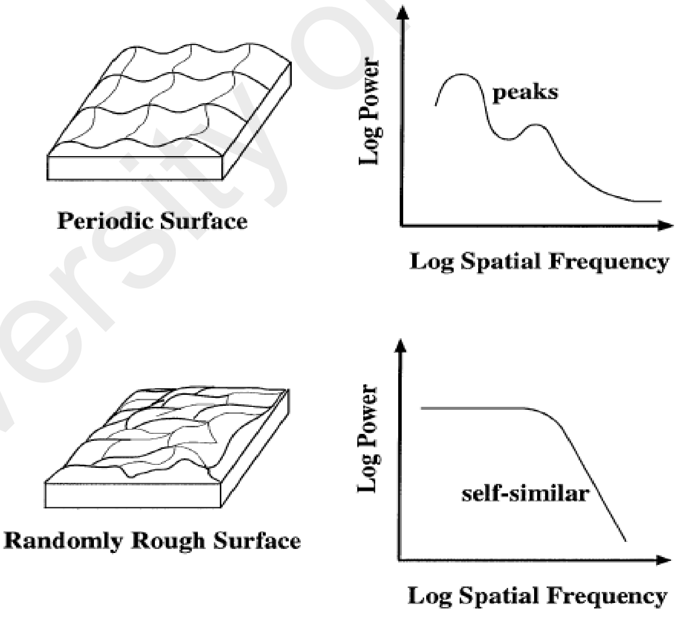

Figure 3.12: Significant difference between log-log plots for periodic surface and randomly rough surface.

Power spectral density (PSD) provides surface roughness data in spectral (spatial frequency) domain (Buchko et al., 2001). Any peak occurs in the PSD would represent the characteristic dimension of the surface, as shown in Figure 3.12. Ordered (periodic) surface would contribute to periodic peaks and amorphous surface exhibits self-similar in the PSD.

PSD is a squared of Fast Fourier Transform (FFT) of the topology which provides the spatial frequencies spectrum in inverse units of length. As the spatial frequencies range from $0 \rightarrow \infty$, the PSD reveals the difference of the surface roughness. Complex spatial data can be analyzed in frequency or wavevector space using Fourier analysis. PSD of an image $I(x,y)$ is determined its Fourier transform as shown below:

$$S(k_x,k_y) = \frac{1}{MN}\left|\int_{-M/2}^{M/2}\int_{-N/2}^{N/2} I(x,y)e^{-i(xk_x+yk_y)}dxdy\right|^2 \qquad (3.1)$$

where M, N are the scan length in x and y directions respectively, and k_x, k_y are the spatial frequencies for x and y directions, respectively. In practice, $M, N >> 1$ and by assuming image isotropy, one can take angular average (Sentilkumar et al., 2005)

$$S(k) = \frac{1}{2\pi}\int_0^{2\pi} S(k,\theta)d\theta \qquad (3.2)$$

where $k = \sqrt{k_x^2 + k_y^2}$ and $\theta = tan^{-1}(\frac{k_y}{k_x})$.

PSD of a homogeneous shift invariance or stationary surfaces can be linked to the two point correlation function using Fourier transform. Thus it is described as k-correlation model (Qian et al., 2013) and one such example is the Lorenztian type PSD

$$S(k) = \frac{A}{(1+B^2k^2)^{\frac{(C+1)}{2}}}. \qquad (3.3)$$

University of Malaya

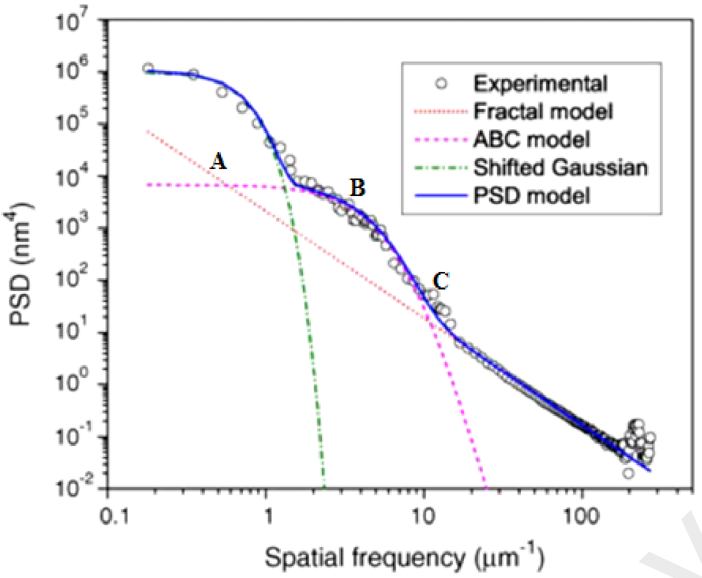

Figure 3.13: Analytical models have been used to fit the PSD functions (Senthilkumar et al., 2005).

From log-log plot of the PSD, parameters *A* (height of the rough surface), *B* (grain size), and *C* (power-law exponent) can be determined, as shown in Figure 3.13. The parameter *A* indicates the height of the rough surface, which usually corroborate well with the root-mean-squared roughness. The parameter *B* from k-correlation model here explains the correlation length of the surface, which represents the micron length of two connecting points on the surface. The exponent *C* represents the fractal region of the surface, which is also the nature of the roughness that contributes to the fractal dimension of the topology. For instance, this approach has been adopted to describe the surface morphology of pentacene thin films with its substrate (Itoh & Yamauchi, 2007).

However, at low spatial frequency, the PSD is often affected by measurement noise, resulting in greater inaccuracy in the determination of parameter *A*. At large wavevector (referring to small spatial scale) regime, the PSD plot exhibit power-law scaling

$$S(k) \sim \frac{1}{k^{\gamma}} \tag{3.4}$$

University of Malaya

where γ is the spectral exponent often used as surface roughness measure. Higher values γ of gives smoother surfaces. Fractional Brownian Motion (FBM) with Hurst exponent $0 < H < 1$ provides a powerful tool to generate natural looking fractal graphs and surfaces. A two-dimensional FBM has a PSD of power-law type as described in (4) with $\gamma = 2H + 2$, hence $1 < \gamma < 3$. The noise process associated to FBM or the generalized derivative of FBM is known as fractional Gaussian noise (FGN). FGN is shift-invariant (or stationary) Gaussian stochastic process with power-law correlation function and also has power-law type in the form of (4) with $\gamma = 4H - 2$ thus accommodating $0 < \gamma < 2$ for $½ < H < 1$. The fractal dimension is then given by $D_{\mathrm{PSD}} = 3 - H$. In this study, the FGN is used as the stationary Gaussian surface model in order to compare with the stationary GCP model.

Studies (Wang & Xu, 2004; Gavrila et al., 2007; Dash et al., 2009) also have shown that PSD model parameters can be used to provide more accurate connection to carrier mobility based on spectral (or wavevector) information at low and high spatial frequencies.

In this study, the AFM scan size of the first set of thin film is 10 μm × 10 μm with elevation map scaled to surface height range of 100 nm. The range of the spatial frequencies depends crucially on the sampling distance and the scan length. And the accuracy of the PSD functions is limited by the measurement artifacts. Therefore, five processed images of 400 ×400 pixels for each stage are sub-sampled from the parent images (from top-left, top-right, middle, bottom-left and bottom-right corner of the parent image). It means that the spatial frequency ranges of the sub-images (extracted from the parent image) are partially overlapped with each other, with the results thereafter combined and averaged. This is called as extended PSD, which has also been adopted in report by Gavrila et al. (2007) to generate a more accurate PSD curve.

University of Malaya

3.3.2 Generalized Cauchy Process

Empirical variogram has been extensively applied in geostatistics (Bojović et al., 2008; Mashiah et al., 2008; Timbó et al., 2009) especially hydrology (Meyer et al., 2015) and soil geo-morphological study (Kerry & Oliver, 2011) to indicate spatial correlation in observations measured at sample locations. Correlation or variogram analysis allows the spatial features to be determined particularly the textures and the two-point image pixel correlation. The complexity increases when the variation appears to be random but spatially correlated at some scale. The examples of spatial random variables are air temperature, rainfall, porosity of different rocks, the concentration of charge carriers in active layer and etc. The process is called as stationary when many realizations are needed to compute the randomness. The random process is represented by

$$Z(x) = \mu + \varepsilon(x) \tag{3.5}$$

where *Z(x)* is a random variable at position x, μ is the mean of the process and $\varepsilon(x)$ is the a random quantity. A covariance, *C(h)* with a random quantity, $\varepsilon(x)$ of zero mean,

$$C(h) = E[\varepsilon(x)\varepsilon(x+h)] \tag{3.6}$$

Thus,

$$C(h) = E[\{Z(x) - \mu\}\{Z(x+h) - \mu\}] \tag{3.7}$$

which is equivalent to

$$C(h) = E[\{Z(x)\{Z(x+h) - \mu^2] \tag{3.8}$$

where h is the lag distance (sample separation), *E* is the estimation at that point, *Z(x)* and *Z(x+h)* are the magnitudes of Z at position x and x+h respectively. The covariance function is replaced by the semivariance, named as variogram, $\gamma(h)$ to overcome the situation whereby the estimation differences are zero,

$$\gamma(h) = \frac{1}{2}E[\{Z(x) - Z(x+h)\}^2] \tag{3.9}$$

However, the variogram does not represent the real properties of the data but to assist in visualizing the complexity and to predict the conditions at selected sample location.

The experimental variogram is then fitted with plausible weighted least square approximation models to extract the parameters which competently describe the complexity. Such models include Gaussian, power, exponential, spherical, GCP and others.

GCP has been used in wide variety of applications including biomaterials surfaces study (Muniandy & Stanslas, 2008). In this morphological study, GCP incorporates the RMS roughness measure through the fractal dimension determined from the local growth scaling behaviour of the semi-variogram when $h \rightarrow 0$. The semi-variogram contains useful information that can be used to characterize detailed morphological features. Any oscillation in the semi-variogram would suggest the presence of ordered/periodic structures, an example of non-stationary feature. For example, nugget effect is referred to $\Gamma(0) \neq 0$ when there are clusters of blobs/patches in the image. The onset of the plateau in the semi-variogram gives the range, h_R suggesting the maximum distance between two spatial points for non-zero correlation before the semi-variogram reaches a plateau indicating lack of correlation between pixels.

The GCP provides unique decoupling of the fractal parameters, thus allowing the surface to be characterized for roughness (using H or D) and two-point spatial correlation exponent (using β) independently. FBM is a fractal process but it cannot be used to generate shift-invariant homogeneous (or stationary) surfaces as the process only has increments stationary. However, one may opt to use Fractional Gaussian Noise (FGN) instead of FBM. In order to generate stationary surfaces with fractal properties, one needs a concrete Gaussian process (or random field) that accommodate dual-fractal properties, namely power-law scaling in the local growth (variance) and in correlation

University of Malaya

function, with independent scaling parameters. An example of such as a stochastic process is known the generalized Cauchy process (GCP) characterized by the correlation function with spatial lag *h*:

$$C(h) = \frac{\sigma^2}{(1+|\frac{h}{a}|^{\alpha})^{\beta/\alpha}} \tag{3.10}$$

or equally written as the semi-variogram

$$\Gamma(h) = (\sigma^2 - \frac{\sigma^2}{(1+|\frac{h}{a}|^{\alpha})^{\beta/\alpha}}), \tag{3.11}$$

where the GCP model parameters (α, β) as such, α is the fractal exponent related to Hurst exponent $\alpha = 2H$ and β is related to the correlation exponent. Meanwhile, sample variance is given by σ^2 and *a* is the spatial scale factor.

Experimental variogram for a particular separation vector of interest is determined by averaging one half the difference squared of the *z*-values over all pairs of observations at lag distance. The variogram values increase with increases in the distance of separation until it reaches the maximum sample variance. Generalized Cauchy process (GCP) is characterized by the correlation function with spatial lag *h,* and the semi-variogram is fitted on the empirical semi-variogram with $h = (h^2_x + h^2_y)^{½}$, as shown in Figure 3.14.

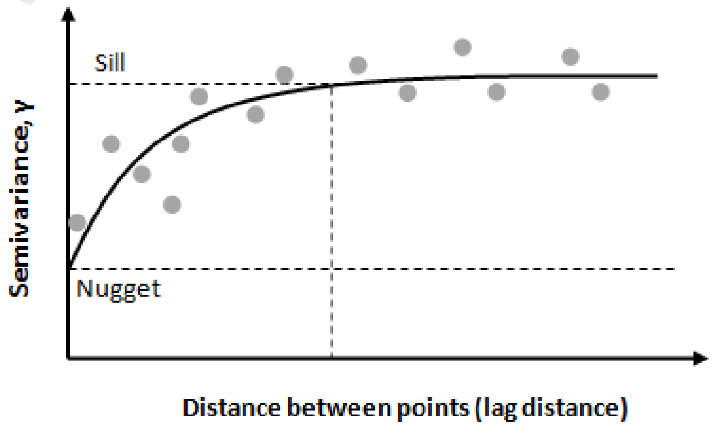

Figure 3. 14: The sill and the presence of nugget in a semivariogram.

University of Malaya

GCP provides dual-fractal descriptors through the fractal dimension $D_{GCP} = 3 - \alpha/2$ and the long-range dependence (LRD) via$1 - \beta/2$, independently (Karan & Mallik, 2008). A fractal signal that exhibits long-range persistence dependence can be predominantly quantified by Hurst exponent. Correlation behaviour can be observed from β exponent, whereby $\beta \in (0, 1)$ indicates LRD and $\beta > 1$ indicates short-range dependence (SRD).

Assuming the gray-level intensity of an image $I(x,y)$ at grid points (x_i, y_j) is represented by $I_{i,j}$, where $i = 1, 2, \ldots, M$, and $j = 1, 2, \ldots, N$. The empirical semi-variogram is then computed as:

$$\Gamma(h_x, h_y) = \frac{1}{[(M-h_x)(N-h_y)]} \sum_{i=1}^{M-h_x} \sum_{j=1}^{N-h_y} (I_{i+h_x,\ j+h_y} - I_{i,j})^2, \tag{3.12}$$

where MN is the total number of points on the surface, $(M - x_i)$ and $(N - y_i)$ are the number of pairs of points, respectively at spatial lag distance $h_x \in [-M/2, M/2]$ and $h_y \in [-N/2, N/2]$.

GCP model semi-variogram (3.10) is then fitted on the empirical semi-variogram (3.11) with $h = \sqrt{h_x^2 + h_y^2}$. Model parameters α and β are the two most important parameters that will be extracted and used for dual-fractal descriptors of complex surfaces.

3.3.3 Fractal Box-Counting Method

There are a number of alternative measures that have introduced to characterize the surface properties, for example the power spectral density, two-point correlation function or variogram and, of course the fractal parameters, such as Hurst/Holder exponent (that have all been described in previous sections), and fractal dimension.

Fractal methods has been adopted in many application, such as material science (Huang et al., 1997; Rao et al., 2002; Kong et al., 2014), rock mass characterization

University of Malaya

(Bagde et al., 2002), viscosity (Zhang & Liu, 1998; Lazouskaya et al., 2006), morphological study of cell (Muniandy & Stanslas, 2008; Tambasco et al., 2010), and mammography (Raguso et al., 2010; Rangayyan et al., 2010). It provides robust multi-dimensional descriptors for surface roughness and texture heterogeneity.

As mentioned in Chapter 2, fractal dimension provides 2D descriptors that are a good reflect of surface roughness and heterogeneity. The calculation of fractal dimensions and other related parameters are useful as quantitative morphological and developmental descriptors. The box counting method is the most commonly used to generate fractal dimension of a complex object.

A three dimensional image size of $L \times L$ with spatial surface *(x, y)* denoting pixel coordinate and z denoting the gray level intensity of the pixel. The method begins by superimposing regular grid of pixels of length L on a binary image and counts the number N of occupied pixels/boxes. This procedure is repeated by using different length value of L with defining power-law relationship, $N(L) = L^{-D_f}$, where D is the fractal dimension of the topology surface that can be estimated from the slope of the logarithmic regression line:

$$D_f = -\lim_{L \to 0} \frac{logN_L}{\log L} \tag{3.13}$$

The box counting method shows the development of the complexity as L approaches 0. For example, in this work, L_{12} represents the box size scale of 12 pixels wide. Fractal dimension is estimated by superimposing the grid of boxes with different box scale length on the image. Smaller grid box size as shown in Figure 3.15 (a), describes the substructures better with higher fractal dimension of 1.55 as compared to the Figure 3.15 (b) with fractal dimension of 1.39. With smaller scale of pixel box (grid), the count of occupied box is getting higher which characterizes the substructure of the topology, as shown in Table 3.1 and the result of fractal dimension is shown in Figure 3.16.

University of Malaya

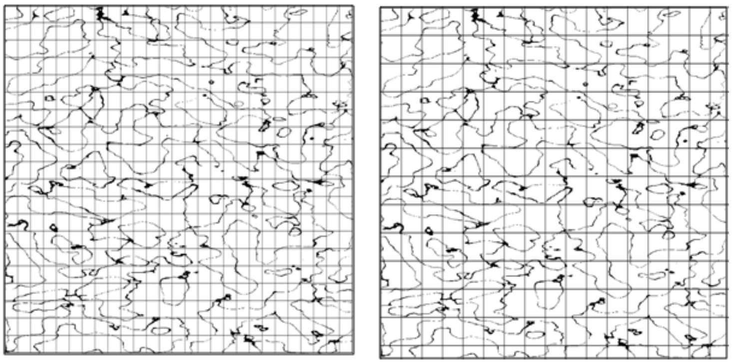

(a) **(b)**

Figure 3.15: Different grid box size contributes to different fractal dimension measurement for the same image.

Table 3.1: Box counting result for Figure 3.15 (b).

Length, *L*	**Box counting, *N (L)***
L_2	14075
L_3	9158
L_4	6804
L_6	4419
L_8	3247
L_{12}	2058
L_{16}	1468
L_{32}	537
L_{64}	144
L_{128}	36

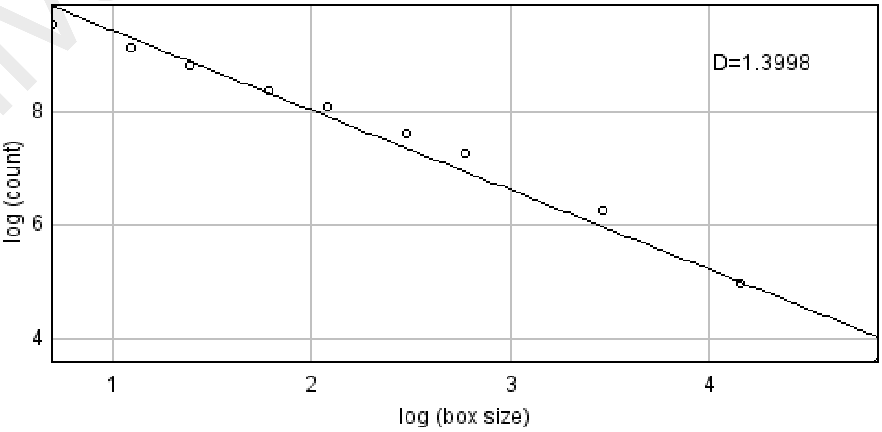

Figure 3.16: Extracting the fractal dimension from the slope of the logarithm regression line for the Figure 3.15 (b).

University of Malaya

Accuracy of fractal dimension estimation can be increased by shrinking the grid size repeatedly, that would increase the coverage of substructure in the topology.

For a thin film image, the white pixels represent the fibrous component while the black pixels represent the inter-fiber space or substrate material. Estimation of fractal dimension on the structure of interest has to be carefully selected from the background as the results are significantly different from each other. At the same time, the direct estimation of fractal dimension from the power law linear regression line explains limited feature of a complex and disordered structure. Therefore, the implementation of modified box counting method (MBCM) and multi-fractal analysis have been suggested to overcome the mentioned drawback (Lopes & Betrouni, 2009).

3.3.4 Distribution of Fractal Dimension &Percolation Theory

The distribution of fractal dimension or fractal spectrum, which is generated by computing fractal dimension for each point of selected channel of colour information (Red, Green, Blue, Hue, Saturation, Brightness, Intensity). Example of a fractal spectrum has been shown in Figure 3.17, which is produced by using a fractal spectrum generator software called Harmonic and Fractal Image Analyzer, (HarFa). HarFa software was implemented by Institute of physical and Applied Chemistry, Technical University of Bino in Czech Republic.

Fractal spectrum analysis has been applied in grading cervical cancer images according to cells formation in the tissue (Jayalalitha & Uthayakumar, 2009), plants (Azzarello et al., 2009) and texture analysis (Florindo & Bruno, 2012).

University of Malaya

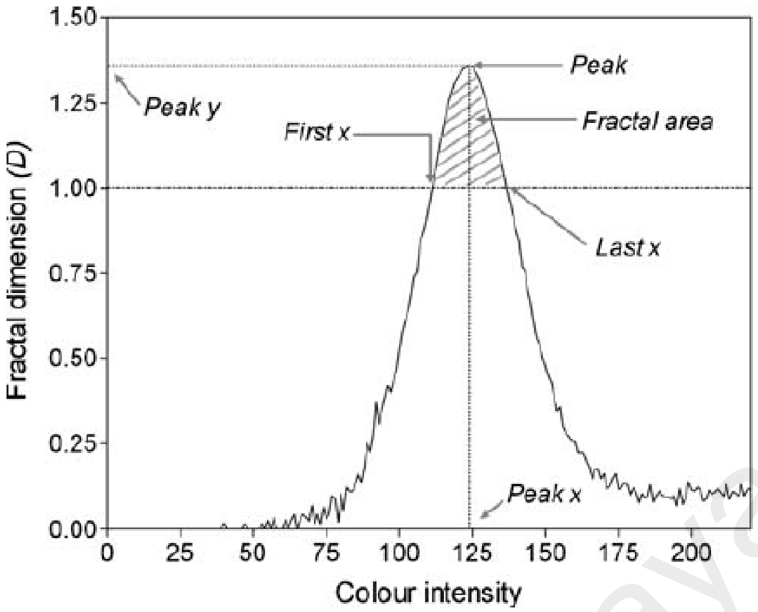

Figure 3.17: Fractal spectrum has been generated to detect damages on olive plants (Azzarello et al., 2009).

The generation of a fractal spectrum begins with applying box counting method to cover an image with boxes and then computing the number of covered boxes where, N_B = number of black boxes, N_W = number of white boxes, N_{BW} = number of black and white boxes, N_{BBW} = number of black and white and black boxes, N_{WBW} = number of black and white and white boxes. This measurement is repeated by using different sizes of boxes. Resulting fractal dimension is displayed as a function of masked level of colour information (for example, gray level intensity of an image). D_{BW} characterizes properties of border of fractal pattern; D_{BBW} characterizes fractal pattern on the white background; and D_{WBW} characterizes fractal pattern on the black background.

In this study, fractal spectrum is generated to discriminate the significant clustering contours effect at whole range of thresholding conditions. It determines the count of pixels of the same gray color and provide the information of the total conductive area that has been spanned by the connecting bonds.

In this work, thresholding technique is used to provide labelling for almost-connected-component and also enable the visualization of the clustering contour effect

University of Malaya

at different gray levels. Color image is first converted to 8-bit grayscale and then processed under different stage of thresholding conversion to eliminate the shadowy region due to the minor unconnected clusters or other topographical irregularities. The local regularity of the thin films is characterized by the fractal dimension, whereby the result has been compared to the findings based on image analysis of the clustering effect from AFM and the fractal spectrum.

Thresholding technique is often used for image segmentation that transforms an image into black and white (BW) or binary image that separate the object of interest from the background. The input image can be grayscale or color. The segmentation process will convert all data points below a certain threshold to zero and data points above that threshold to one. The binary image has grayscale intensity ranged from 0 to 255, where intensity of 0 has been categorized as black and 255 as white. For instance, pixels which are categorized as black has similar grayscale of multivariate values that share certain topological characteristics and forms a connected region.

The grayscale image is then processed by using box counting method to generate fractal spectrum which indicates data points according to the grayscale intensity. As mentioned earlier, the method begins by superimposing regular grid of pixels of length L on a binary image and counts the number N of occupied pixels/boxes. This procedure is repeated by using different length value with defining power-law relationship: $N(L) = L^{-D}$. The fractal dimension, D can be estimated from the slope of the logarithmic regression line, $D = -(\log N)/(\log L)$. And the steps are repeated for all 256 pixels for each AFM image to complete the fractal spectrum.

Next, interpretation of the fractal spectrum is done by applying the structural properties of percolation to visualize the charge transport phenomenon in the active layer.

University of Malaya

The percolation theory has been applied in many fields over the years, e.g., to predict the oil field performance (King, Buldyrev, Dokholyan, & Havlin, 2002), to pharmaceutical technology (Leuenberger & Ineichen, 1997), to investigate the charge transport in disordered organic electronic devices (Yimer et al., 2009), to model for ionic transport in composite and glasses (Bunde & Dieterich, 2000) and many other applications.

The electron mobility μ between two composites can be predicted by percolation theory (Tada, Harada, Onoda, Nakayama, & Yoshino, 1999):

$$\mu = S(P - P_c)^d \tag{3.14}$$

where μ is the electron mobility, S = the scaling factor, P = occupation probability, P_c = the percolation threshold and d = the critical exponent (the conductivity exponent). Different critical exponent value will affect the whole result, whereby the critical exponent depends on the Euclidean or fractal dimension of the process (Siegmund & Leuenberger, 1999). Thus, a relationship between fractal dimension and percolation theory should be modelled to investigate further the carrier transport phenomena in disordered organic semiconductors to achieve significant improvement in device performance, as shown in Figure 3.18.

University of Malaya

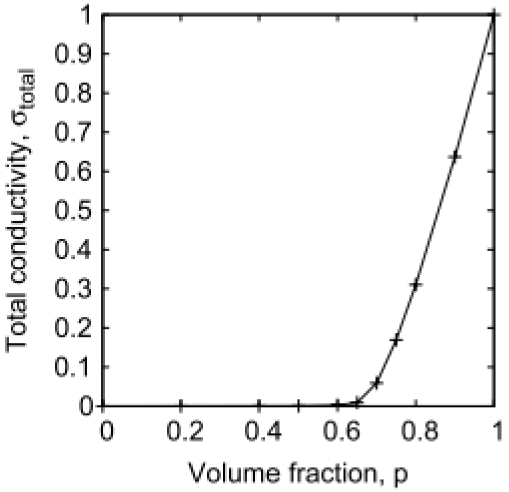

Figure 3.18: Percolation curve shows the linear scale behavior of the average of total conductivities of a continuum percolation model (Matsutani et al., 2012).

Percolation theory is an effective approach to characterize the randomness of internal topology of a composite with higher precision (Kalnaus et al., 2011). They suggested that there is profound connection between the probability distribution of random walks on disordered network, with the example shown in Figure 3.19.

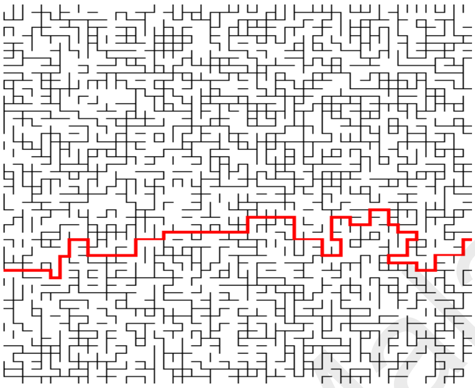

Figure 3.19: The percolation threshold occurs when a number of nanotubes is connected to form an electrical connection across the material.

As shown in Figure 3.20, a percolation transition is characterized by a set of universal critical exponents, which describe the fractal properties of the percolating medium. Site occupation probability of 0.50, 0.58, 0.59, 0.60 respectively shown in Figure 3.20 (a) to (d), and (e) near the critical threshold, the maximum cluster takes on fractal properties, and behaviour becomes markedly different (Schroeder, 1992).

The study of percolation theory helps to improve the overall device performance, for instance, the reduction of the percolation threshold of Ag has improved the overall performance of the Ag thin film electrode with the introduction of MoO_3 interlayer to enhance the lateral growth of Ag thin film (Wang et al., 2014).

University of Malaya

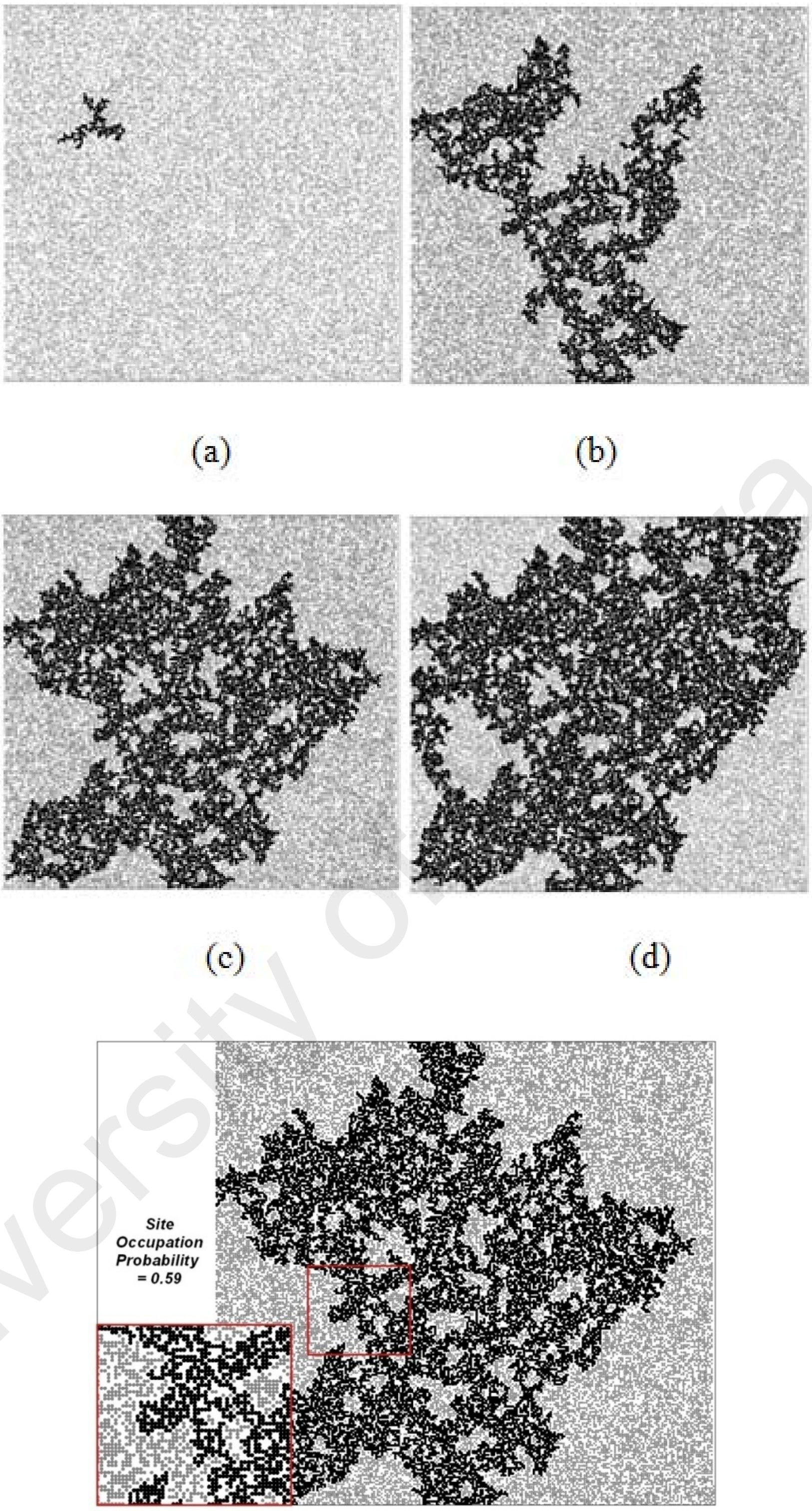

(a) (b)

(c) (d)

(e)

Figure 3.20: A percolation transition is characterized by a set of universal critical exponents, which describe the fractal properties of the percolating medium. (a) - (d) (Schroeder, 1992).

University of Malaya

The application of percolation theory in determining the cluster statistics and transport mechanism in composites has been further described (Dani & Ogale, 1997). The cluster formation and growth of the fibrous network have been observed and they reported that the fractal dimension increased when the randomness of the microstructure increased. In their work, the critical exponent that describes the geometrical of the percolation network has been discussed. Nevertheless, there was no further investigation on the relationship between transport exponents and percolation critical exponents.

To understand and visualize the charge transport in microstructure morphology remains challenging. However, it is feasible to describe the transport phenomenon effectively through percolation theory. For example, various doping concentrations have resulted in change of charge mobility by using percolation theory with charge transfer integral calculation (Li et al., 2013). According to their work, the power-law dependence of the carrier mobility upon concentration can be explained successfully by determining the percolation threshold in a co-evaporated amorphous organic molecular mixture. The authors has also commented that the bond percolation might be more effective in describing the charge transport in disordered organic semiconductor mixtures and a proper fiber/molecular alignment will ensure a continuous percolating pathway.

Percolation theory is widely used to characterize the morphological of disordered system. The overall conductivity of a percolating network can be observed near percolation threshold and it is possible to determine the conductivity exponent from the percolation curve. Therefore, studies have been carried out to investigate the conductivity exponent in a percolative network and its relationship with the Euclidean dimension of the topology. For instance, the conductivity exponent and the correlation exponent of three-dimensional percolation network were calculated by using random

University of Malaya

walk simulations based on molecular trajectory algorithm and the ant-in-the-labyrinth method (Cen et al., 2012). Besides, two-dimensional random fractal network has been studied for DC conductive percolation network interacting with Sierpinski carpet (Young & Fang, 2000) whereby the DC percolation current near percolation threshold (below and above) has been reported to exhibit scaling behaviour in its ranges. By modifying the fractal pattern in the percolating network, the percolation threshold changed as well. This means, by changing the fiber/molecular arrangement in the morphological structure, the percolation threshold will be shifted and its parameters will be directly affected.

In the log-log plot shown in Figure 3.21, the percolation curve has shown different scaling behaviour at four regions. For higher order of iteration of Sierpinski carpet, the percolation threshold will be bifurcated. For highly heterogeneous surface, the critical path analysis under percolation theory is crucially important to reveal the transport phenomenon. For a percolative network, there is a continuous interconnecting path for the carriers to flow between the interfaces. Percolation theory explains the geometry of connectivity of a system (Hunt, 2001). The spatial correlations and the distributions of the conductivity can be generated by cluster statistics of percolation theory. However, they mentioned about the challenge to calculate the chemical length for critical path analysis which influentially contributes to the DC conduction properties calculation.

University of Malaya

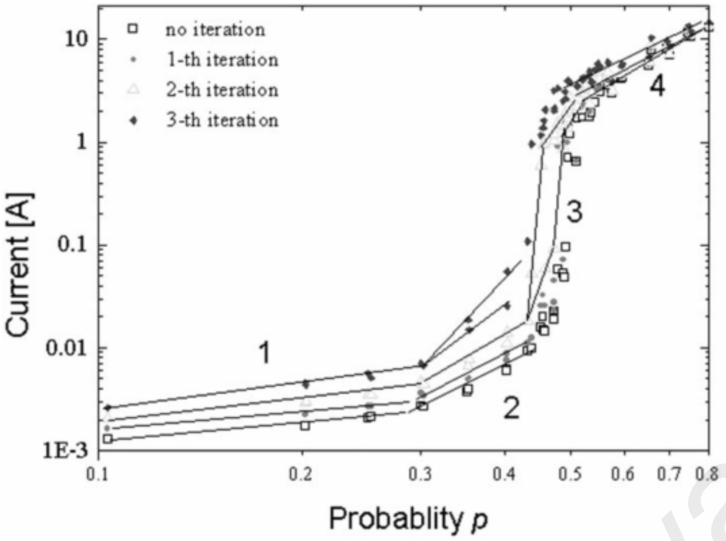

Figure 3.21: Log-log plot of the percolation current in the percolative network (Young & Fang, 2000).

A percolative network in which a conducting path consists of connected clusters that are present with occupation probability P and absent with probability $(1-P)$. For a highly disordered network, the density of the fibrous components acts like electrical conductors when it reaches percolation threshold. Below the percolation threshold, there is insignificant concentration of connected micro fibers and thus no distinct percolative cluster formed which explain a network of disconnected clusters ($P < P_c$). The cluster size is finite and self-similar at this phase. The charge transport has been restricted within the cluster which is secluded from the others. The charge carriers tend to move to adjacent unoccupied space by diffusion which results in minimum conductivity rate.

At percolation threshold point, P_c, the clusters are fractal and the carriers might be trapped due to the existence of internal holes within the cluster, which are non-reachable from outside the cluster. The finite clustering size effect can be clearly seen when P approaching P_c. The system changes its behaviour qualitatively during phase transition ($P = P_c$), that leads to formation of macroscopic clusters for current to flow abruptly when $P \geq P_c$.

University of Malaya

Above percolation criticality, the propagation of the charge carriers across the module is fast and in tremendous amount. At this stage, the interconnected clusters form a continuous percolating path with chemical distance, l which is separated by geometrical distance, r. The chemical distance, l, reveals the length of the shortest path between two sites of cluster for transporting electrons, while the geometrical distance represents the displacement corresponding to the starting and the ending points of hopping. In some cases there is possibility to have more than one chemical path, which consist of percolative bonds carrying the electric current, often referred as elastic backbone of the cluster.

In this work, the fractal dimension of each thin film is determined from the AFM data using generalized Cauchy process (GCP) model. Fractal spectrum is also used to provide labelling for almost-connected-component and also enable the visualization of the clustering effect at different segmentation stage. The results are thereafter compared to the current density – voltage (*J*-*V*) graph and the conventional surface descriptor such as power spectral density (PSD) and rms roughness.

Analysis of morphological parameters based on AFM images using GCP approach will be reported in next chapter. The GCP result is thereafter compared to the current density – voltage (*J*-*V*) graph and the conventional surface descriptor such as power spectral density (PSD) and rms roughness.

Fractal spectrum is generated to show the distribution of fractal dimension with respect to different image gray levels segmentation in order to quantify the complexity of the disordered structure. For disordered microstructure, the formation of atomic and subatomic processes cannot be visualized in complex spatial time-domain but it can be analyzed through image segmentation using thresholding technique. Thresholding technique is used to provide labelling for almost-connected-component and also enable the visualization of the clustering contour effect at different gray levels. The dusky

University of Malaya

region due to the minor unconnected clusters or other topographical irregularities is eliminated through thresholding technique, whereby the technique is often used for image segmentation that transforms an image into black & white (BW) or binary image to separate the object of interest from the background. The segmentation process will set thresholded pixels to black and all other pixels to white. Pixels which are categorized as black has similar grayscale of multivariate values that share certain topological characteristics to form a connected region.

Box counting method is then used to generate fractal spectrum to show the distribution of fractal dimension with respect to 256 image gray levels. The method begins by superimposing regular grid of pixels of length L on a binary image and counts the number N of occupied pixels/boxes. This procedure is repeated by using different length value with defining power-law relationship: $N(L) = L^{-D}$ and the fractal dimension, D is estimated from the slope of the logarithmic regression line, $D = -(\log N)/(\log L)$.

Fractal spectrum at different gray levels for all thin films has been generated, which determines the pixels of similar grayscale of multivariate values that share certain topological characteristics to form a connected region. The result of the fractal spectrum has been analyzed and explained in next chapter.

University of Malaya

CHAPTER 4: ANALYSIS AND RESULT

Surface morphologies are often used to characterize various interface processes including charge transfer and surface contact between layers in thin films. In fractal surface analysis, Hurst exponent is used as descriptor of surface roughness and the spectral exponent as long-range correlation between two spatially separated points. In this chapter, the results from the modelling techniques such as the application of Fourier based power spectral density (PSD) and the dual parameter stochastic surface model (GCP) have been reported and demonstrated in detailed for describing complex surface morphologies. The PSD and GCP models are used to characterize surface morphologies of organic nickel (II) phthalocyanine-tetrasulfonic acid tetrasodiumthin film. The fractal and correlation exponents estimated from the AFM images of the thin film are then used to explain the variation in the electrical conductivity of thin films (i) treated with solvent for different time durations, and (ii) under different solvent treatment that modified the surface properties.

Morphological analysis of thin film surfaces based on the AFM images are reported in this section, first using the PSD approach followed by the GCP semi-variogram approach for both sets of thin film images. Comparison has been done between two approaches and results have been supported by fractal spectrum analysis and photocurrent density measurement, J_{sc}. In both cases, higher electric conductivity is observed for thin films with higher fractal dimension but also enhanced when there exists spatially correlated morphologies in the form of network enhances charge transport at interfaces.

University of Malaya

4.1 Surface Analysis Under Different Treatment Time

The first set of AFM images obtained from the thin films treated with solvent for different time durations, are first homogenized using uniform illumination routine in MATLAB Image Processing toolbox and the PSD are determined using discrete two-dimensional Fast Fourier Transform routine available in MATLAB. The PSD versus wavevector (or spatial frequency) are plotted on log-log scale.

4.1.1 Power Spectral Density

As shown in Figure 4.1, five processed images of 400 × 400 pixels for each stage are sub-sampled from the parent image of thin film and processed for PSD functions separately, as shown in Figure 4.2. The results are then combined and averaged for higher accuracy.

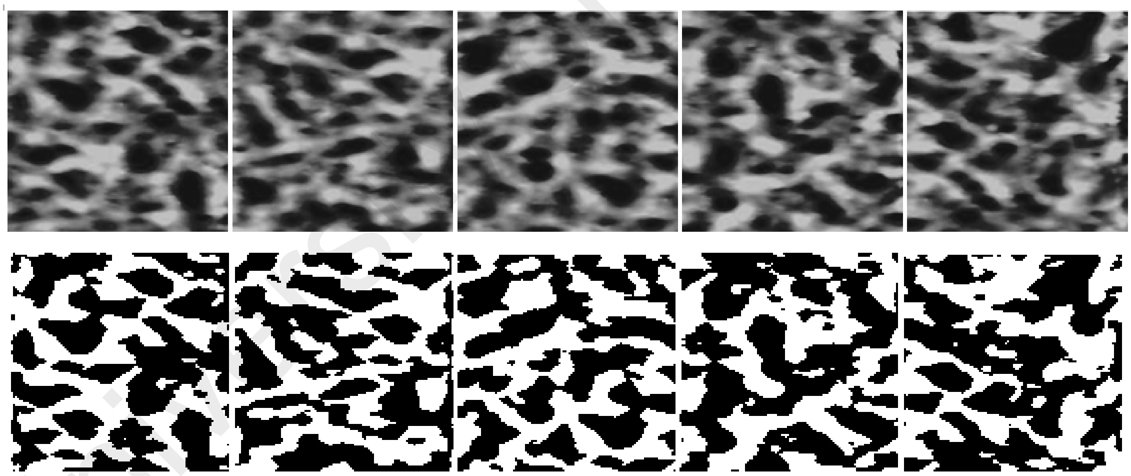

Figure 4.1: Morphological images of thin films under solvent treatment of 40 minutes have been (top five) gray-scaled, (bottom five) thresholded, using image processing toolbox *ImageJ*.

University of Malaya

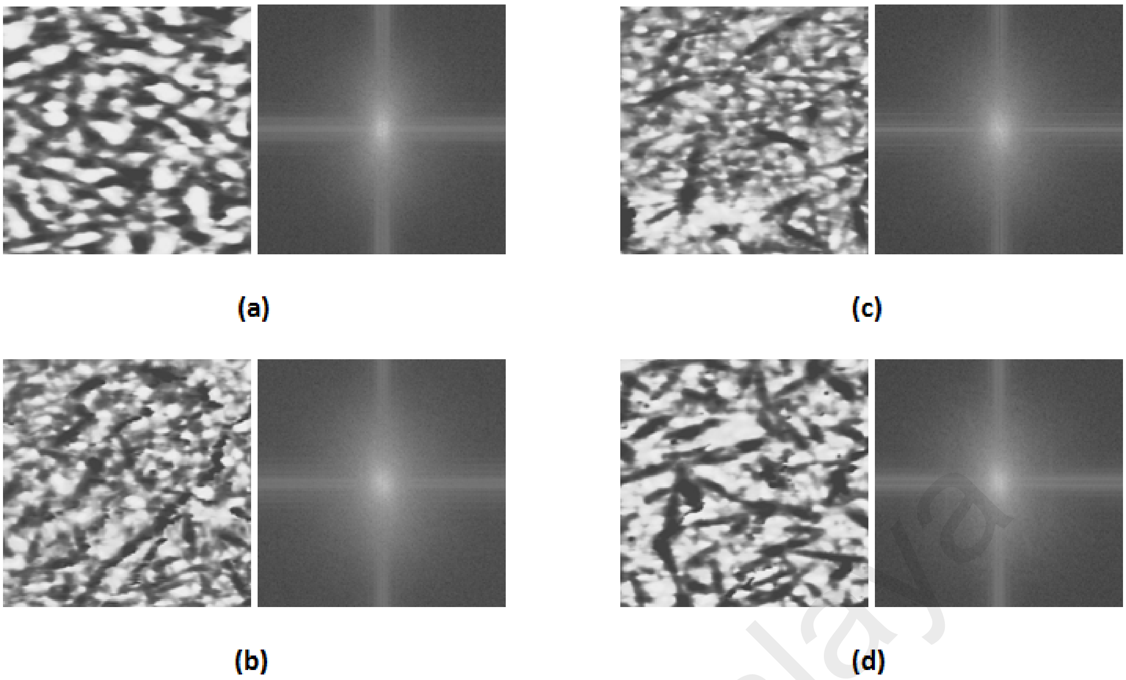

Figure 4.2: Transformation of the original AFM images into frequency domain using fast Fourier Transform (FFT) methods for (a) 40 minutes, (b) 80 minutes, (c) 120 minutes and (d) untreated thin films.

The PSD for all the samples (untreated and treated) exhibit power-law scaling at high spatial frequency regime, even though the range of scaling regime shrunk as the samples are immersed in the chloroform solution for longer period of time. The spectral exponents are obtained using least square fitting of the linear regimes and the results are summarized in Table 4.1.

Table 4.1: 1D and 2D fractal analysis result.

Film	RMS roughness (nm)	1D PSD	2D Fractal Analysis	
		D	*PSD, D_{PSD}*	*Cauchy, D_{GCP}*
Untreated	22	1.36±0.24	2.41±0.02	2.03±0.39
40 minutes	28	1.50±0.21	2.45±0.01	2.20±0.84
80 minutes	17	1.34±0.23	2.33±0.02	2.10±0.31
120 minutes	14	1.29±0.23	2.38±0.02	2.08±0.28

University of Malaya

For untreated film, the elongated microfibers are rather separated from each other. Due to the porosity of the exposed surface of the film, immersion in a poor solvent allows the solvent molecules to absorb and penetrate into the TsNiPc film. As immersion time increases, for example at 40 minutes, the formation of similar sized cluster of microfibers is observed causing the inter-distances between the microfibers to decrease.

Thin film immersed for 40 minutes has allow the formation of relatively bigger grain sizes as compared to the other films due to the surface mobility of the adatoms in the nucleation stages of the film growth (Muniandy & Stanslas, 2008). The presence of a broad spectral peak at $\log_{10}k \sim 4$ also suggests the formation of rather organized but aperiodic structures.

It is noted from PSD plots that films immersed for 80 minutes and 120 minutes have lower roughness if compared to 40 minutes sample. This is quite expected as longer solvent treatment time has caused the exposed surface of the films to etch, and thus smoothen the surfaces gradually.

As mentioned in the earlier chapter, the spatial frequencies are distributed with a specific orientation, that contributes to the different distribution shape, which is similar to a pixels intensity plot. This is particularly important in the measurement of anisotropy model in order to evaluate the material used and its impact to the microstructure morphology.

University of Malaya

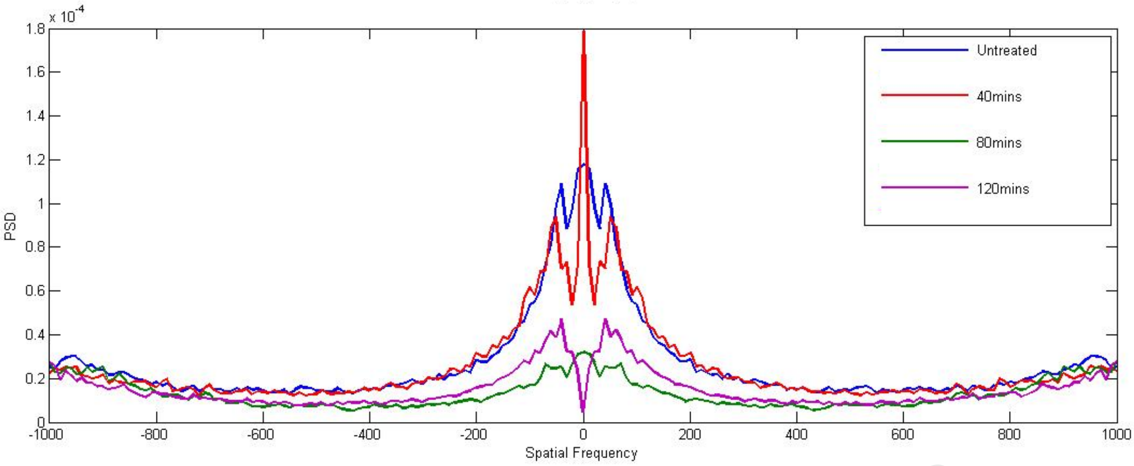

Figure 4.3: One dimensional discrete Fourier transform (1DDFT) produces highest peak for 40 minutes film while 80 minutes film performs the lowest.

University of Malaya

The spatial frequencies are distributed in a pattern that reflects the alignment of fibrous component in the data image. By referring to the one dimensional discrete Fourier transform (1DDFT) as shown in the Figure 4.3, the 40 minutes film shows significant peak as compared to the other films. The distribution is in elliptical shape which reveals that the fiber arrangement in 40 minutes film is somehow aligned and periodic. In contrast, the randomly distributed fibers in 80 minutes and 120 minutes films contribute to more symmetrical and circular shape of distribution. The array data has then been processed by using two dimensional fast Fourier transform algorithm (2DFFT) to extract the fractal exponent.

From the 1DDFT plot, the solvent treatment time remains one of the factor that contributes to the overall surface roughness and fibers alignment changes. With higher solvent treatment time, the thin films exhibit smoother surface with randomly aligned fibers, which causes the reduction of the charge transfer between the electrodes. In other words, the distribution plot can be used to predict the appropriate time range for solvent treatment, even though the plot is unable to provide more morphological details.

The PSD versus wavevector (or spatial frequency) are plotted on log-log scale, as shown in Figure 4.4. Subplots of the PSD with the parameters *B* (correlation length) have been generated, as shown in Figure 4.5. The presence of a broad spectral peak at $\log_{10}k \sim 4$ also suggests the formation of rather organized but aperiodic structures.

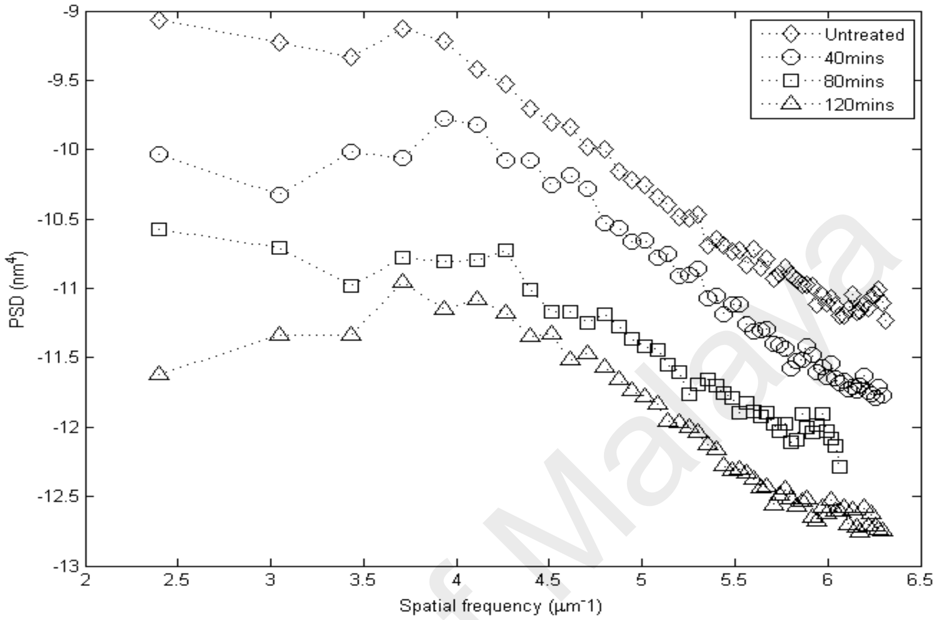

Figure 4.4: Log-log plots for all organic thin films at untreated stage, after solvent treatment of 40 minutes, 80 minutes, and 120 minutes.

University of Malaya

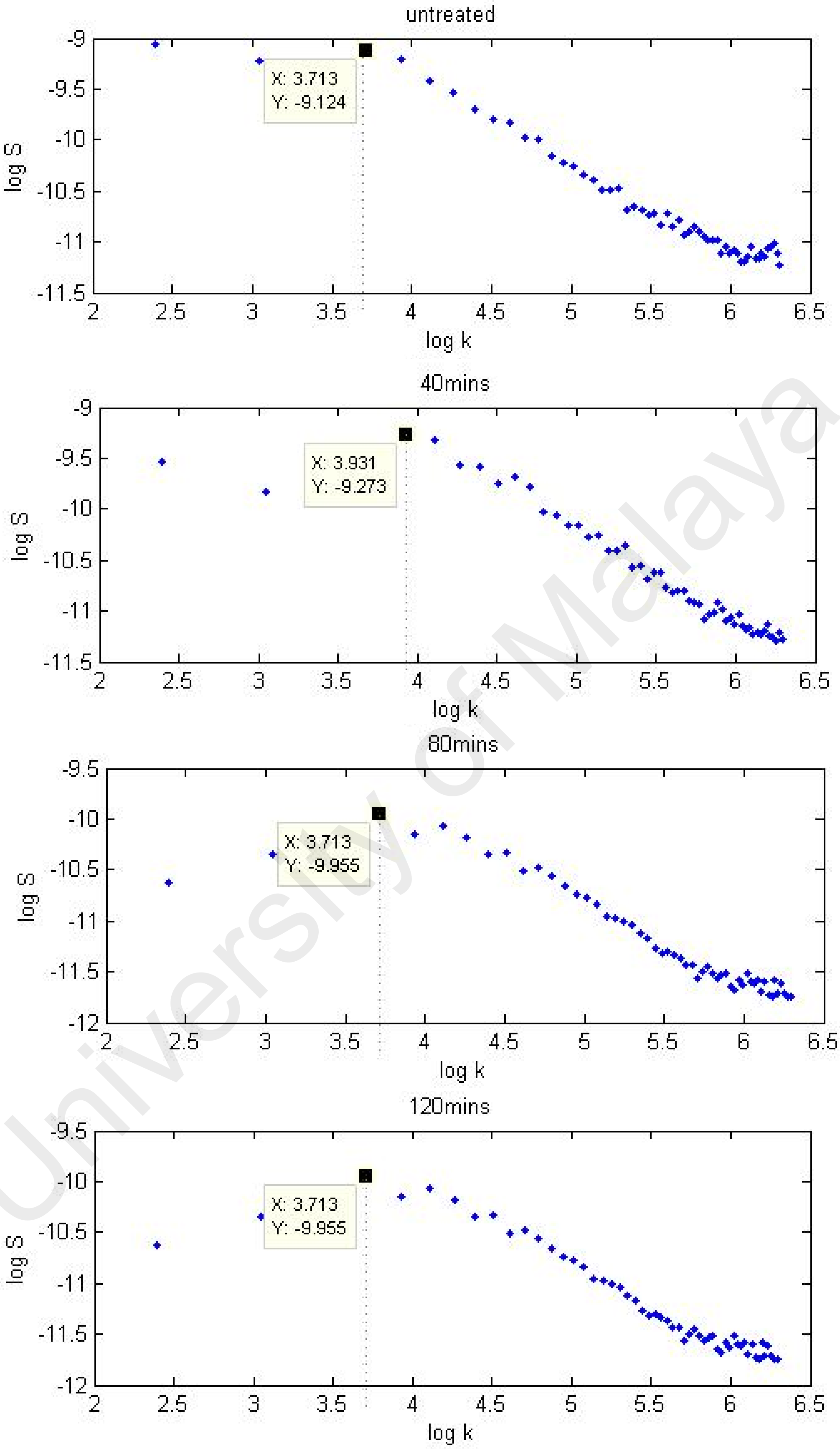

Figure 4.5: Subplots of the PSD with the parameters *B* (correlation length) indicated respectively.

University of Malaya

The spectral exponent γ has been extracted at large wavevector regime, with the PSD plot exhibit power-law scaling for all thin films, as shown in Figure 4.6.

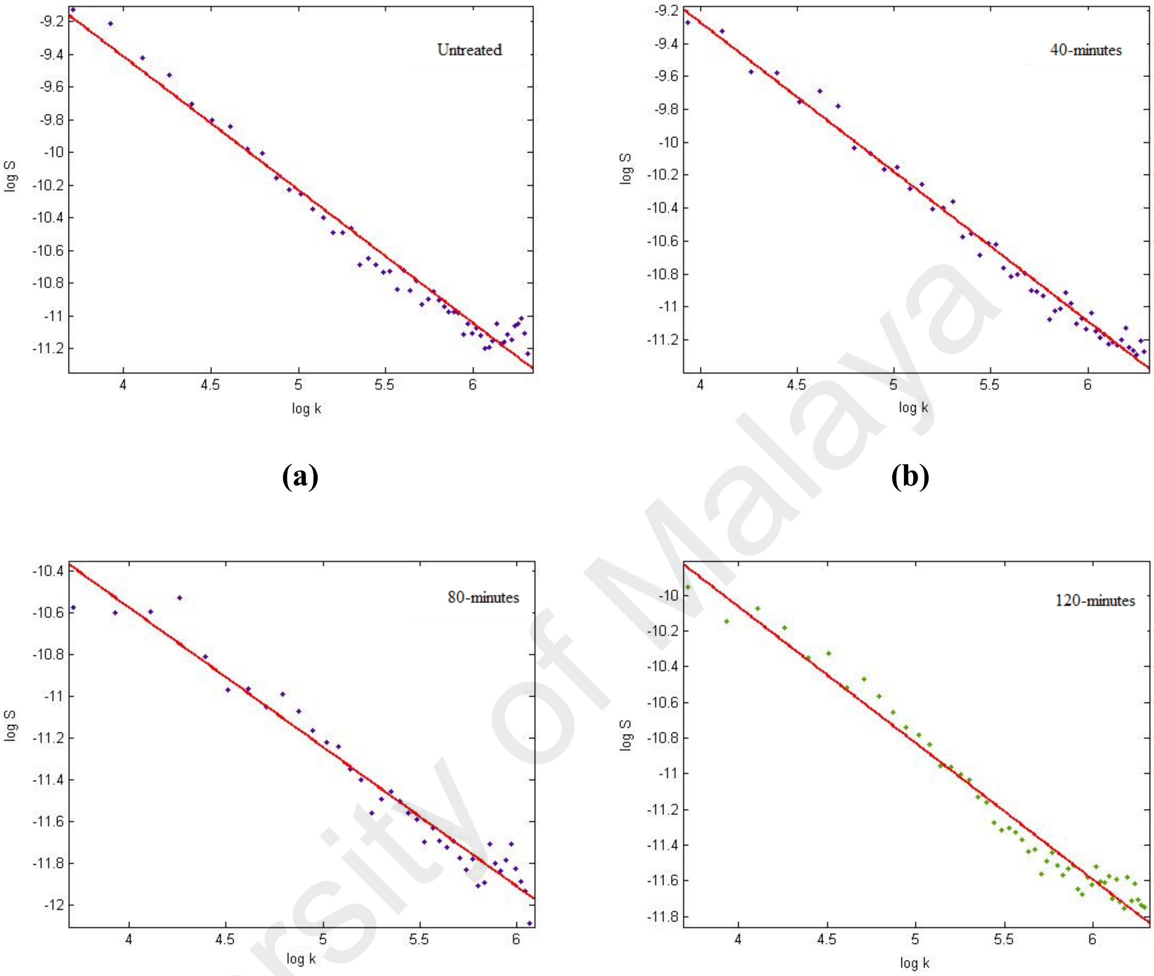

(a) **(b)**

(c) **(d)**

Figure 4.6: The spectral exponent γ has been extracted at large wavevector regime, with the PSD plot exhibit power-law scaling for (a) untreated film, (b) 40 minutes, (c) 80 minutes, and (d) 120 minutes treated films.

PSD approach is well-established and commonly adopted as the standard technique for surface characterization. Nevertheless, the technique involves the transformation of spatial microstructure data into spectral domain, where patterns are to be interpreted in terms of harmonics/wavevectors. Thus, localized features in *x-y* space will be distributed over wide range of harmonics. On the other hand, correlation or variogram analysis allows the spatial features to be analyzed as the way they are perceived by

University of Malaya

human vision, particularly the textures and the two-point image pixel correlation. Moreover, GCP incorporates the rms roughness measure through the fractal dimension determined from the local growth scaling behavior of the semi-variogram when $h \rightarrow 0$.

4.1.2 Generalized Cauchy Process

Analysis has been continued for first set of AFM images by using GCP model. The empirical semi-variograms for the thin films are shown in Figure 4.8. The semi-variogram contains useful information that can be used to characterize detailed morphological features. For example, nugget effect is referred to $\Gamma(0) \neq 0$ when there are clusters of blobs/patches in the image. The onset of the plateau in the semi-variogram gives the range, h_R suggesting the maximum distance between two spatial points for non-zero correlation before the semi-variogram reaches a plateau indicating lack of correlation between pixels. Any oscillation in the semi-variogram would suggest the presence of ordered/periodic structures, an example of non-stationary feature. GCP model based semi-variogram shows reasonably good fit for all the empirical data over wide lag distances, except for film sample immersed for 40 minutes in the solvent. Here, the presence of oscillation is observed suggesting periodic-like structure in the morphology. A similar remark was made earlier when we examined the images using PSD approach. The results of key GCP model parameters (α, β) estimated from the nonlinear least squared of the analytical semi-variogram are summarized in Table 4.1.

The fractal signals exhibit long-range persistence dependence (Qian et al., 2013), which predominantly quantified by Hurst exponent. Correlation behavior is observed from β exponent, whereby $\beta \in (0,1)$ indicates LRD and $\beta > 1$ indicates short-range dependence (SRD). From the Cauchy model, all organic thin films exhibit SRD except 40 minutes film, as shown in Figure 4.7.

University of Malaya

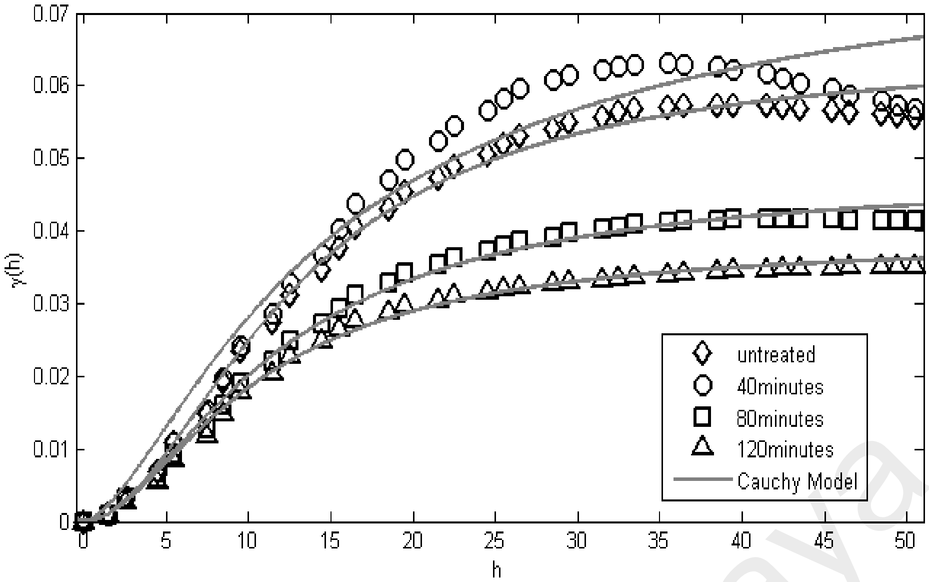

Figure 4.7: Empirical semivariograms fitted by generalized Cauchy field at untreated stage, after solvent treatment of 40 minutes, 80 minutes and 120 minutes.

A decrease in surface roughness with increasing immersion duration time is revealed by progressive reduction in sill variance σ^2 values ($h > h_c$). Films immersed for 40 minutes in solvent showed roughest surface structure if compared to other films samples.

Based on the model parameters summarized in Table 4.2 and Table 4.3, the Cauchy model obviously shows the consistency in the variation of the fractal-related parameters D_{GCP} and β with device performance obtained from photocurrent measurement. Highest photocurrent measured from thin films treated for 40 minutes, which apparently are roughest (RMS = 28 nm or D_{PSD} = 2.45 and D_{GCP} = 2.20) with long-range spatial correlation ($\beta < 1$).

Table 4.2 Estimated model parameters for PSD and GCP.

Films	*2D PSD parameter*	*GCP parameters*	
	γ	α	β
Untreated	0.82±0.04	1.95±0.02	1.68±0.02
40mins	0.91±0.03	1.60±0.11	0.91±0.06
80mins	0.67±0.04	1.80±0.01	1.48±0.01
120mins	0.76±0.04	1.85±0.01	1.51±0.01

University of Malaya

Table 4.3 Morphological parameters with respect to the short-circuit current density

Films	RMS (nm)	D_{PSD}	D_{GCP}	J_{sc}(μA/cm^2)
Untreated	22	2.41±0.02	2.03±0.02	0.525
40mins	28	2.45±0.01	2.20±0.11	0.825
80mins	17	2.33±0.02	2.10±0.01	0.800
120mins	14	2.38±0.02	2.08±0.01	0.600

Both PSD and GCP approaches described above provide characterization of complex surfaces based on fractal parameters. One may notice that the fractal dimensions obtained from PSD and GCP approaches ($D_{PSD} = 2.45 \pm 0.01$ and $D_{GCP} = 2.20 \pm 0.11$, respectively) for the thin films treated for 40 min do not differ significantly (2% and 8%) from that of the untreated film ($D_{PSD} = 2.41 \pm 0.02$, $D_{GCP} = 2.03 \pm 0.02$), even though the measured photocurrent differs significantly (about 57%). This can be attributed to the basic property of fractal object X(r), $r \in R^2$, hence fractal dimension which describes local feature of a fractal object, namely $<|X(r + \tau) - X(r)|^2> \tau^{\alpha}$, as $\tau \rightarrow 0$. In the case of semi-variogram, this limit refers to behaviour of Γ (h) as $h \rightarrow 0$.

Interestingly, as proven by this study, the scaling parameter β obtained from the two-point correlation behaviour of microstructures for large lag using GCP model is able to provide clear explanation of the effect of long range spatial correlation ($\beta < 1$) in thin film treated for 40 minutes with significant increased (about 46%) in current density.

At untreated stage, the cluster size is finite and self-similar but no percolating cluster is formed. The clusters are short-range ($\beta > 1$) spatially distributed fractal (and the charge carriers might be trapped due to the existence of internal holes within the cluster, which are non-reachable from outside the cluster. The charge carriers only move within the cluster or do not move at all if the cluster seem to be isolated from the others. A percolating cluster started to form at 40 minutes and the finite clustering size effect is clearly seen. The system changes its behaviour qualitatively and the percolation network formed at this critical point connects the clusters to transport the charge carriers across

University of Malaya

the medium for the first time (Stauffer & Aharony, 1994). Therefore, the photocurrent density increased significantly from untreated stage to treated film at 40 minutes.

A qualitative explanation can be extracted based on surface topography seen in Figure 4.8, where spatially correlated morphologies in the form of network could have contributed towards enhanced charge transport at interfaces.

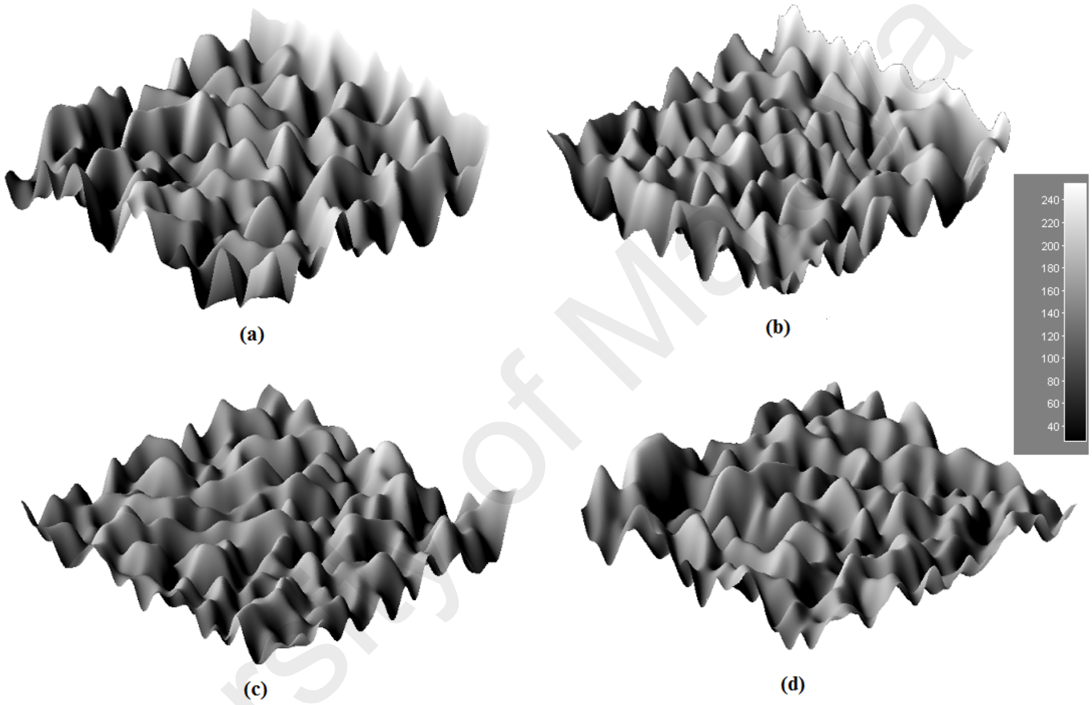

Figure 4.8: Surface topography reconstructed from AFM images for (a) untreated thin film and treated thin films at different time durations: (b) 40 minutes (c) 80 minutes and (d) 120 minutes.

University of Malaya

To conclude the comparison between GCP and PSD approaches, the potential application of dual parameter stochastic surface model, namely the generalized Cauchy process has been demonstrated for describing complex surface morphologies. Conventional approaches such as the spatial indicator based on root mean squared of height fluctuation or the Fourier based power spectral density provides limited information on localized features. The generalized Cauchy process on the other hand, provides dual description of fractal and long-range correlation properties simultaneously.

In this study, the model is used to characterize AFM images of surface morphologies of organic nickel (II) phthalocyanine-tetrasulfonic acid tetrasodium thin films treated with solvent for different time durations.

The local regularity of the thin films is characterized by the fractal dimension, which is shown to corroborate well the findings based on direct measurement of the surface roughness from the AFM. The fractal dimension is relatively higher when the surface is rougher. It is noticed that thin films exposed to solvent for longer duration are smoother.

Higher electric conductivity is observed for thin films with higher fractal dimension but also enhanced when there exists spatially correlated morphologies in the form of network enhances charge transport at interfaces. The latter remark is justified using the correlation parameter $\beta < 1$ obtained from the GCP model.

4.2 Surface Analysis Under Different Solvent Treatment

In this section, random fractal surface modelling methods are adopted and then illustrated by percolation theory to study the second set of AFM images (as shown in Figure 3.6 in previous chapter), which are obtained from the thin films treated with different solvents. Surface morphologies in active transport layers and interfaces often possess fractal dimensions approaching percolation threshold, which have been consistently proven in many research work (A. Dani & Ogale, 1996; Young & Fang, 2000; Cheng et al., 2004; Matsutani et al., 2012).

In the study, the fractal dimension of each thin film is determined from the AFM data using power spectral density (PSD) and generalized Cauchy process (GCP) approaches. The structural properties of a fractal spectrum for studying surface morphologies of organic nickel tetrasulfonated phthalocyanine (NiTsPc) films under different solvent treatment have been studied in order to interpret the relevant transport phenomenon. Analysis of morphological parameters based on AFM images has been described and

University of Malaya

the results are thereafter compared to the current density – voltage (*J-V*) graph and the rms roughness. At the same time, the image grayscale fractal spectrum is generated to show the distribution of fractal dimension with respect to different image gray levels segmentation, which represents the overall roughness changes on the surface topology of thin films. The relationship between the electrical transport properties and fractal dimension has also been discussed in this section.

4.2.1 Power Spectral Density

By using PSD approach, surface texture is interpreted in terms of harmonics/wavevectors providing the spectral exponent to calculate the fractal dimension of a topology. The PSDs for the three films are determined using discrete two-dimensional Fast Fourier Transform routine available in MATLAB. The PSD versus wavevector (or spatial frequency) are plotted on log-log scale as shown in Figure 4.9.

The spectral exponents are obtained using least square fitting of the linear regimes and the fractal dimension has been calculated, as summarized in Table 4.4 and Table 4.5.

Table 4.4 Estimated model parameters for PSD and GCP.

Films	*GCP parameters*		*PSD parameter*
	α	β	γ
Untreated pristine	2.00±0.02	1.99 ±0.01	0.59±0.18
Chloroform	1.55±0.01	0.63±0.01	0.71±0.17
Toluene	1.97±0.02	0.88±0.02	0.08±0.17

Table 4.5 Fractal dimensions with respect to the rms and short-circuit current density (J_{sc})

Films	D_{GCP}	D_{PSD}	RMS (nm)	J_{sc} ($\mu A/cm^2$)
Untreated pristine	2.00±0.02	2.29±0.09	41.43	0.08
chloroform	2.23±0.01	2.35±0.08	15.91	0.15
toluene	2.02±0.02	2.04±0.08	8.59	0.10

University of Malaya

The fractal dimensions obtained from PSD approach are 2.29±0.09, 2.35±0.08, and 2.04±0.08 for untreated pristine, chloroform-treated, and toluene-treated films respectively. The highest D_{PSD} for chloroform-treated film does not differ significantly from that of toluene-treated film. Both films exhibit power-law scaling at high spatial frequency regime, as expected. Interestingly, the PSD for toluene film shows a flattening in the log-log plot at high spatial frequencies region and the fractal exponent yields the value of 0.08±0.17, which suggests a non-fractal surface pattern in the morphology.

Without solvent treatment (untreated pristine film), the film surface has bigger granular structure size corresponds to lower fractal dimension (D_{PSD}) and therefore smaller photocurrent density. As the film treated with chloroform, some part of the bigger structure has been etched by the poor solvent. Such immersion process has produced the smaller granular structure size before the drying process. During the drying process, the smaller structures were aggregated and aligned in ordered/periodic structure, as seen in Figure 3.6 in previous chapter, which significantly increase the fractal dimension (D_{PSD}) and the photocurrent density of the mentioned film.

University of Malaya

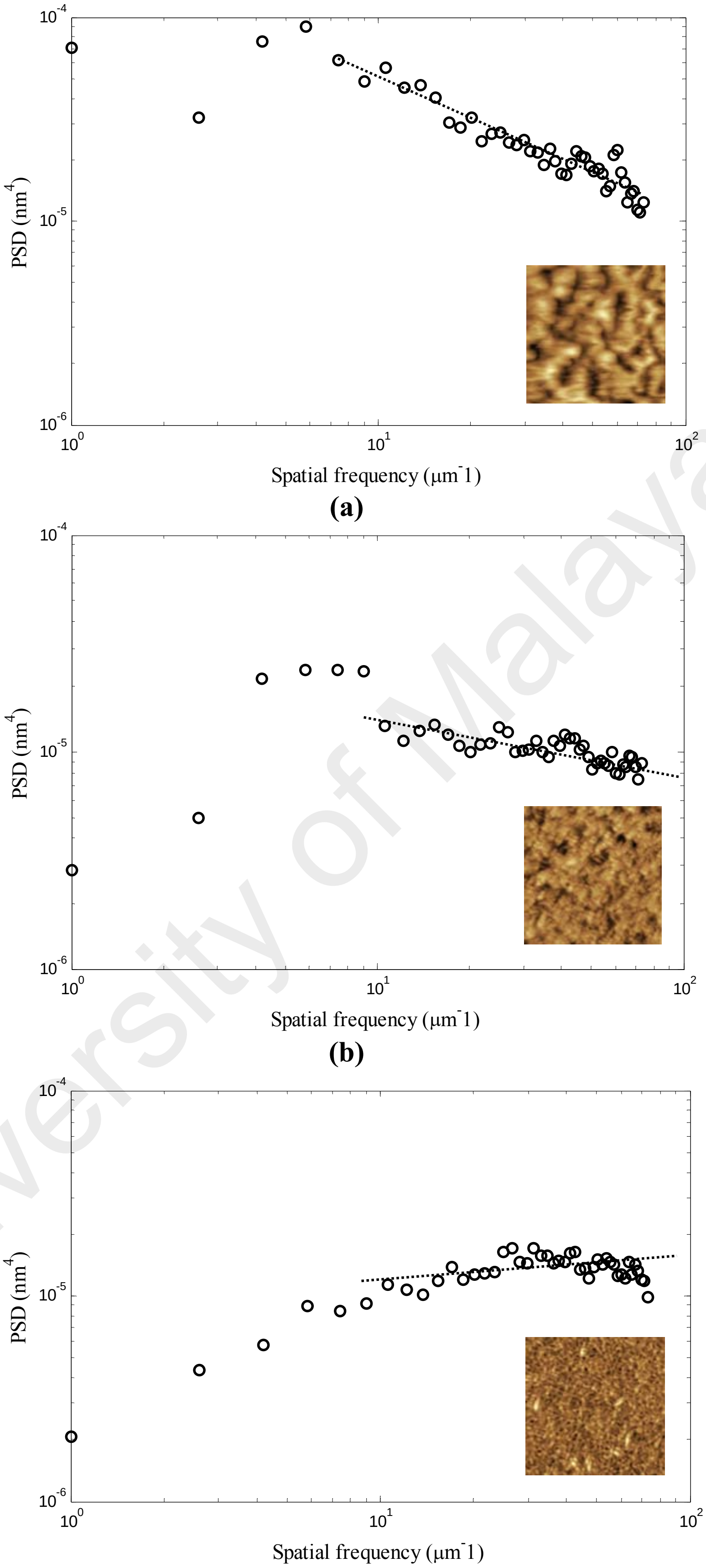

(a)

(b)

(c)

Figure 4.9: Fractal exponent has been extracted from the gradient of PSD plots for (a) untreated pristine, (b) chloroform, (c) toluene films.

University of Malaya

To show the consistency in the variation of fractal-related parameters with device performance obtained from photocurrent density measurement, the PSD result is thereafter compared to the GCP approach that accommodates dual-fractal properties.

4.2.2 Generalized Cauchy Process

Interestingly, we observed that the film with higher rms roughness does not contribute to the greater photocurrent density in this study, as referred to the results listed in Table 4.5. The untreated pristine with highest rms roughness value of 41.43 nm contributes to the lowest photocurrent density of 0.08 μA/cm^2, while the results of the other two films seem inconsistent too. This explains that the conventional spatial indicator such as rms of height fluctuation is lack of information on localized regularity and unable to describe the spatially correlated morphologies in the form of network that could have contributed to the charge transport at interfaces. Nevertheless, more localized features of the thin films can be characterized by fractal dimension, which is shown to corroborate well the findings based on direct measurement of the photocurrent density from the IV graph. The photocurrent density is relatively higher when the fractal dimension is greater. To accomplish this, all the AFM images are first homogenized using uniform illumination routine in MATLAB Image Processing toolbox and the GCP determines the local growth scaling behavior of the semi-variogram when $h \to 0$. The GCP model parameters (α, β) estimated from the nonlinear least squared of the analytical semi-variogram are summarized in Table 4.4.

University of Malaya

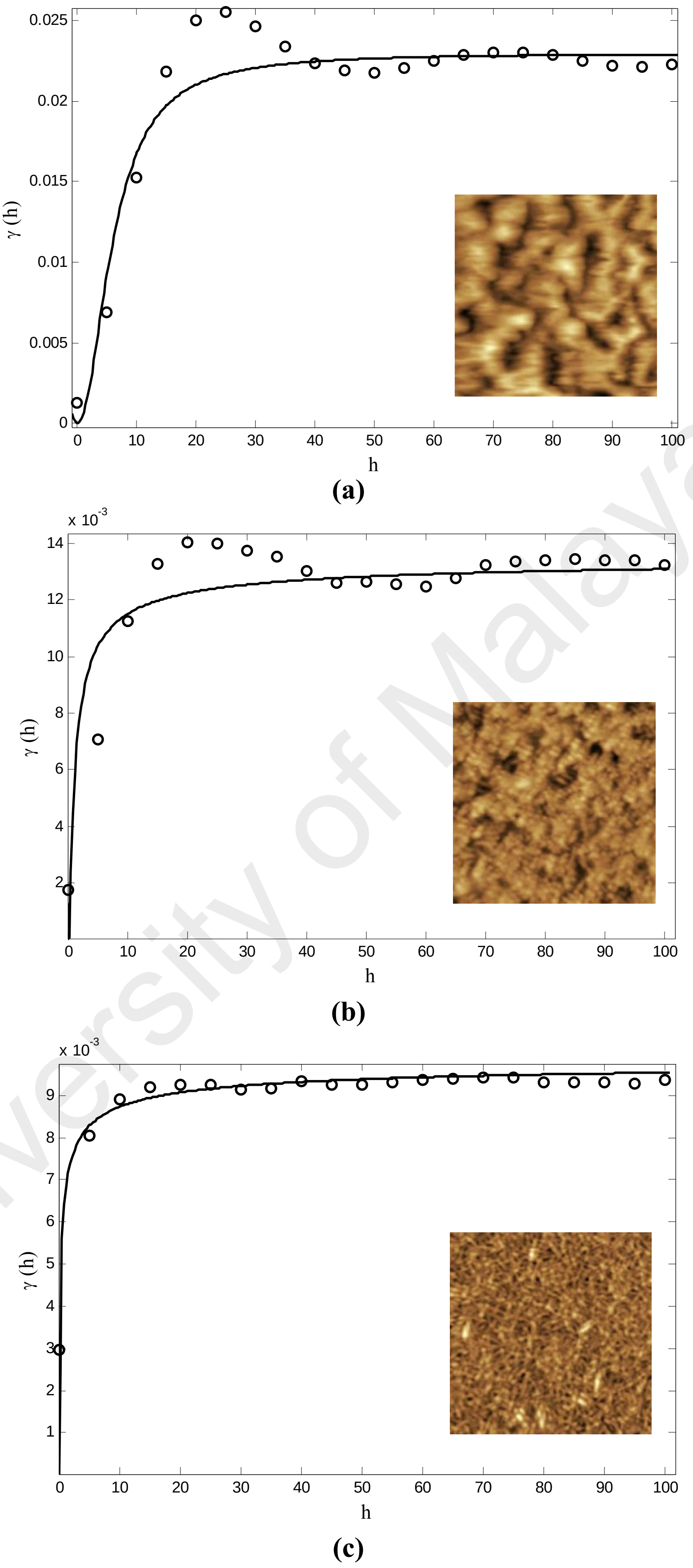

Figure 4.10: Empirical semivariograms fitted by Cauchy model for (a) untreated pristine, (b) chloroform, (c) toluene films.

University of Malaya

The correlation behavior can be observed from β exponent, whereby $\beta \in (0,1)$ indicates LRD and $\beta > 1$ indicates short range dependence (SRD). In this study, both chloroform and toluene treated films are exhibiting LRD except the untreated pristine film. The clusters are short range ($\beta > 1$) spatially distributed fractal for pristine film with short range spatial correlation of 1.99, whereby limited charge transport is expected across the electrodes. On the other hand, there is significant increase in photocurrent density for chloroform and toluene films which exhibit long range spatial correlation of 0.63 and 0.88, respectively ($\beta < 1$). This emphasizes the potential application of the correlation scaling parameter β to indicate the formation of a continuous percolating path from macroscopic interconnected clusters that leads to abrupt flow of current. The correlation exponent β changes with increase surface roughness, which suggests that a larger β has a smaller fractional dimension and thus a smoother surface, as proven by this study.

We observed a significant decrease in surface roughness after the films undergo different solvent treatment, which is revealed by the sill variance σ^2 values. By referring to the semivariograms in Figure 4.10, the sill variance are 0.023, 0.014 and 0.009 for untreated pristine, chloroform and toluene respectively. This result corroborates well with the direct measurement of the root mean squared of height fluctuation for the three films, which characterizes the fundamental structural aspect of the morphology but not the detailed localized features such as correlation length. The films under solvent treatment started to aggregate and align to form interconnected clusters during the evaporation of solvent or the drying process. Therefore, there are obvious periodic oscillations as seen in Figure 4.10 (b) for chloroform film, which suggest the formation of ordered structures in the morphology.

University of Malaya

4.2.3 Image Grayscale Box-counting Fractal Spectrum

Grayscale box-counting fractal spectrum is useful for detailed analysis of grayscale contour lines that may be related to percolation network. The clustering contours effect can be visualized through fractal spectrum that indicates the formation of percolative network, which represents the density of fibrous components spanning the module at different gray levels. By referring to the fractal spectrum, isolated and spatially distributed short range structure would give fractal dimension $D < 1$, line-like structure would contribute $D \sim 1$, while area-like interconnected clustering network has $D > 1$. The greater the morphologic complexity of an object, the higher its fractal dimension (Tambasco et al., 2010).

In this study, fractal spectrum is used to provide labeling for almost-connected-component and also enable the visualization of the clustering contour effect at different gray levels segmentation to analyze the random formation of atomic and subatomic processes. The dusky region due to the minor unconnected clusters or other topographical irregularities is eliminated through thresholding technique, whereby the technique is often used to transform an image into black & white (BW) or binary image to separate the object of interest from the background. The segmentation process will set thresholded pixels to black and all other pixels to white. Pixels which are categorized as black has similar grayscale of multivariate values that share certain topological characteristics to form a connected region. Figure 4.11, Figure 4.12 and Figure 4.13 are the binary images based on gray levels segmentation for all thin films.

Conventional box counting method is then used to generate fractal spectrum, as shown in Figure 4.14, that shows the distribution of fractal dimension with respect to 256 image gray levels. The method begins by superimposing regular grid of pixels of length L on a binary image and counts the number N of occupied pixels/boxes. This procedure is repeated by using different length value with defining power-law

University of Malaya

relationship: $N(L) = L^{-D}$ and the fractal dimension, D is estimated from the slope of the logarithmic regression line, $D = -(\log N)/(\log L)$.

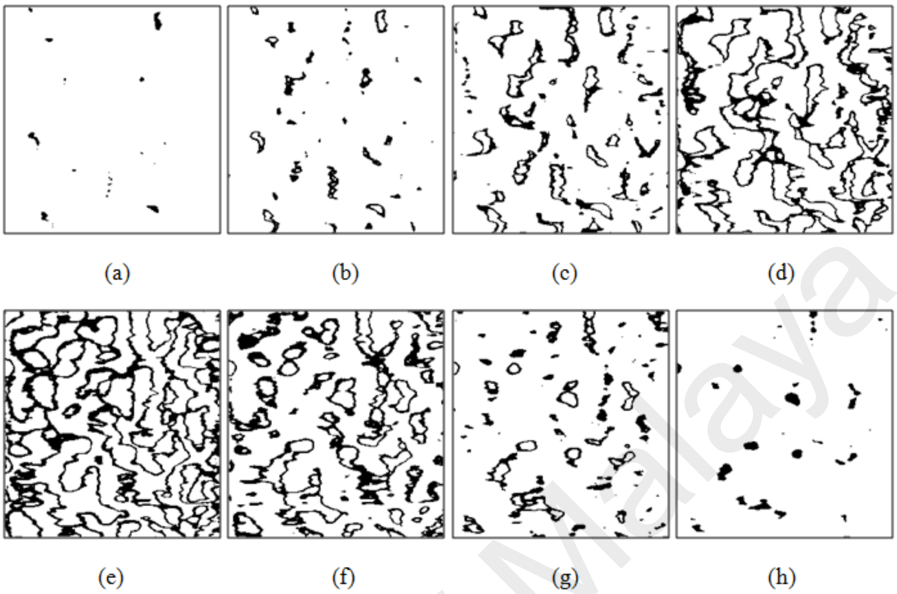

Figure 4.11: The binary images based on gray levels segmentation (a) 0-25, (b) 26-50, (c) 51-75, (d) 76-100, (e) 101-125, (f) 126-150, (g) 151-175, and (h) 176-255 pixels for untreated pristine film.

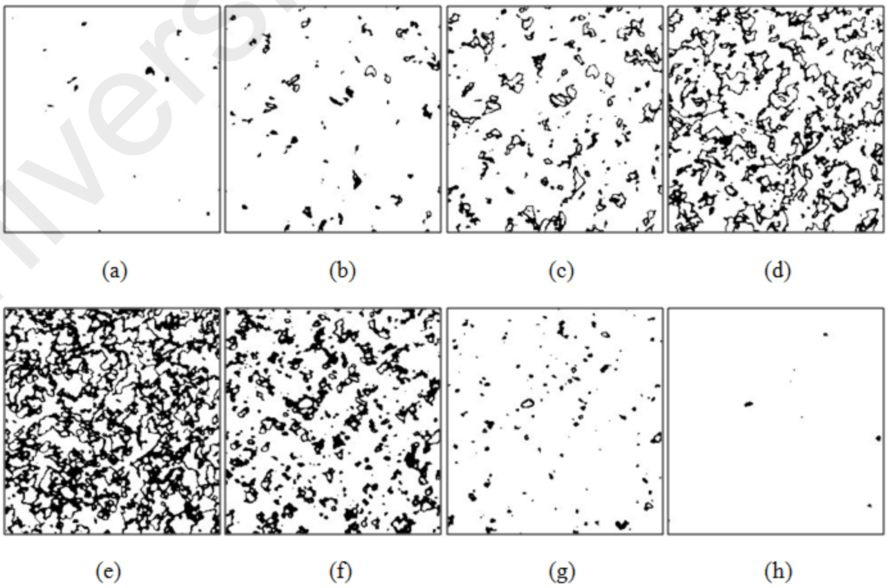

Figure 4.12: The binary images based on gray levels segmentation (a) 0-25, (b) 26-50, (c) 51-75, (d) 76-100, (e) 101-125, (f) 126-150, (g) 151-175, and (h) 176-255 pixels for chloroform film.

University of Malaya

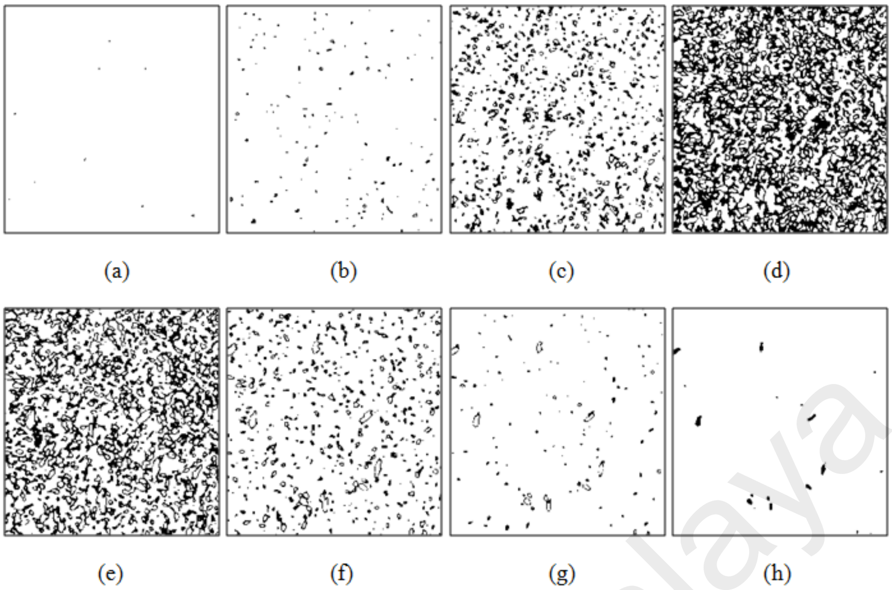

Figure 4.13: The binary images based on gray levels segmentation (a) 0-25, (b) 26-50, (c) 51-75, (d) 76-100, (e) 101-125, (f) 126-150, (g) 151-175, and (h) 176-255 pixels for toluene film.

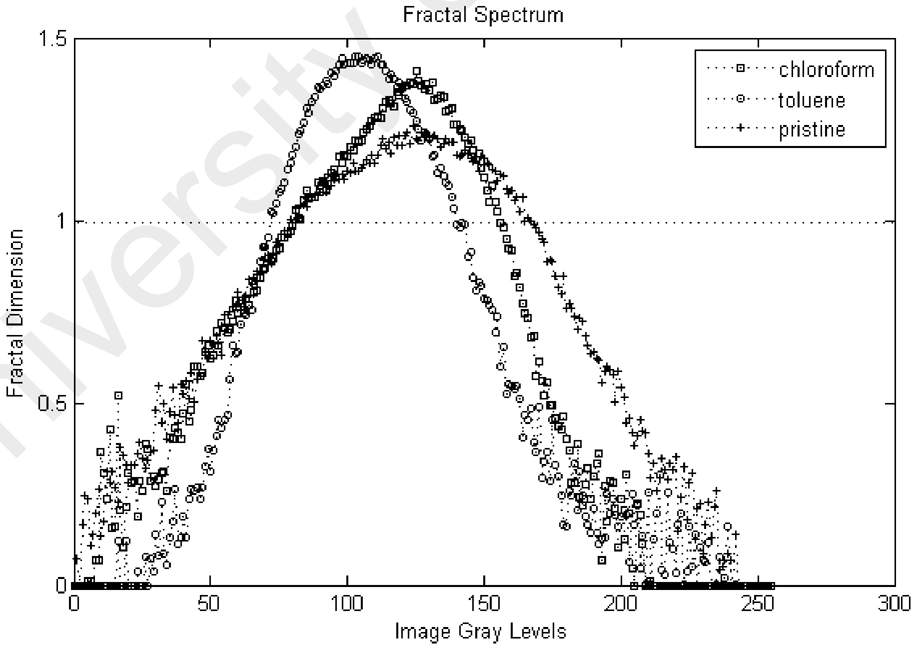

Figure 4.14: Fractal spectrum at different gray levels for all thin films, which determines the pixels of similar grayscale of multivariate values that share certain topological characteristics to form a connected region.

University of Malaya

As mentioned earlier, the 2D topology with low fractal dimension ($D < 1$) shows no noticeable cluster or obvious connection among the fibers while the topology with fractal dimension, $D = 1$, performs line-like network connection. The finite clustering size effect is clearly seen only when the fractal dimension becomes greater. The topology is observed to exhibit area-like interconnecting clustering network with greater fractal dimension ($D > 1$), which competently represents a larger area of connected network/clusters for charge transfer.

Therefore, a qualitative explanation can be extracted based on fractal spectrum as shown in Figure 4.14, the spectrum peak of both toluene and chloroform films with fractal dimension of 1.45 and 1.41 respectively perform area-like interconnecting clustering network while the untreated pristine film exhibits line-like structure with fractal dimension of 1.21 (towards D_f =1). Area-like interconnecting clustering reveals long range spatial correlation morphologies in the form of interconnecting network, which contributes to enhanced charge transport at interfaces. As shown in Fig. 4.13(d), toluene film performs area-like interconnecting clustering network towards the valley pixels while the chloroform's long range connection is seen at the mountain pixels of the periodic structure, as shown in Fig. 4.12(e). This has suggested that the total conduction area has increased between the interfaces for chloroform film. At this stage, the macroscopic clusters are interconnected to form a percolative network, which results in rougher surface topology that can be described by fractal dimension. The inter-connected percolative network allows fast propagation of the charge carriers across the module in tremendous amount (Grover et al., 2012). Therefore higher photocurrent is expected for chloroform film as compared to the toluene film. From the experimental observation, the device using NiTsPc film treated with chloroform produce a better electrical performance as compared to NiTsPc treated with toluene.

University of Malaya

For untreated pristine film, line-like structure is observed as shown in Fig. 4.11(e), indicating lack of correlation between pixels. The clusters are short range spatially distributed fractal as the elongated microfibers are rather separated from each other. There is insignificant concentration of connected microfibers or no distinct percolative cluster formed to explain an interconnecting network. The cluster size is finite and self-similar with the charge transport restricted within the cluster which is secluded from the other isolated clusters. In this situation, the charge can only move to adjacent unoccupied space by diffusion which results in minimum conductivity rate. As shown in Figure 4.11, the inter-distances between clusters for pristine is bigger as compared to chloroform and toluene, causing the lengthening of hopping distance for carriers, which possibly contributing to the lowest charge transfer rate. The system conductivity is expected to decrease when the neighbouring network possesses larger chemical length, l, which causes disconnected percolation pathway preventing the carriers to move to infinity across the module. The chemical distance, l, reveals the length of the shortest path between two sites of cluster for transporting electrons, often referred as elastic backbone of the cluster. However, the computation of the diffusion rate, chemical length and the precise hopping length are yet to be investigated in this work.

In this study, the nugget effect for untreated pristine, chloroform, and toluene films are 0.001265, 0.002391 and 0.002422 respectively. The overall nugget effects for three films are relatively small and almost equal to zero ($\Gamma(0) \cong 0$), indicates that there is no measurement error and short-scale variability in the sampling image. However, the explanation of the higher natural nugget effect on toluene film is that the solvent has dispersed the aggregate into small pieces over the space, causing it losing original spatial correlation. The aggregate size depends on the type of solvent used and the solvent concentration. The GCP result (D_{GCP} = 2.02±0.02) corroborate well with PSD plot (D_{PSD} = 2.04±0.08) for toluene film which exhibits nearly flat slope and the fractal

University of Malaya

exponent, γ of 0.08±0.17. The both results suggested that the surface possesses the characteristics of marginal fractal.

The fractal spectrum result has been confirmed by obtaining the fractal dimension, D_{GCP} using GCP approach that shows the consistency in the variation of the photocurrent density. Higher photocurrent has been reported for chloroform film of 0.15 μA/cm^2 (D_{GCP} = 2.23±0.01), followed by toluene film of 0.10 μA/cm^2 (D_{GCP} = 2.02±0.02) and pristine film of 0.08 μA/cm^2 (D_{GCP} = 2.00±0.02). The result is in good agreement with our previous findings (Kong et al., 2014) and other research works (Cheng et al., 2004; Matsutani et al., 2012) whereby the higher electric conductivity is observed for thin films with higher fractal dimension.

Interestingly, the GCP result (D_{GCP} = 2.00±0.02) has been strikingly different from the PSD result (D_{PSD} = 2.29±0.09) for untreated pristine film but corroborate well with fractal spectrum analysis. The untreated pristine film exhibits non-fractal characteristics with short range dependence (which predominantly quantified by Hurst exponent) as interpreted simultaneously from the GCP model and the fractal spectrum analysis. The D_{GCP} result has successfully predicting the lowest photocurrent density of untreated pristine film. In this work, we observe that the two-point correlation behaviour of microstructures using GCP explains the effect of long range spatial correlation in chloroform film with significant increased (about 87.5%) in photocurrent density.

The gray level contour images can be used to reconstruct 3D surface plot, as shown in Figure 4.15. In the final region of image gray levels range from 175 to 255, the chloroform thin film perform less granular counts as compared to the other two films. This is due to the faster rate of evaporation and aggregation of chloroform film. It is noticed that choosing a higher vapor pressure solvent with greater evaporation rate will cause the thin films to dry out quicker and the granular aggregate faster. This reduces the percolation threshold and speeds up the formation of the chemical path for the

University of Malaya

charge carriers to facilitate across the region. In other words, the density of the fibrous cluster increases at faster rate when the granular experiences rapid aggregation, which results in higher fractal dimension for a better percolative network to transport charge carriers. As a result, it has been observed that different types of solvent treatment is responsible to the overall roughness changes in providing extensive information on the surface topology of thin film. However, this procedure might be limited by the irregular fluctuations seen towards the both ends of the fractal spectrum, which are often affected by measurement noise.

University of Malaya

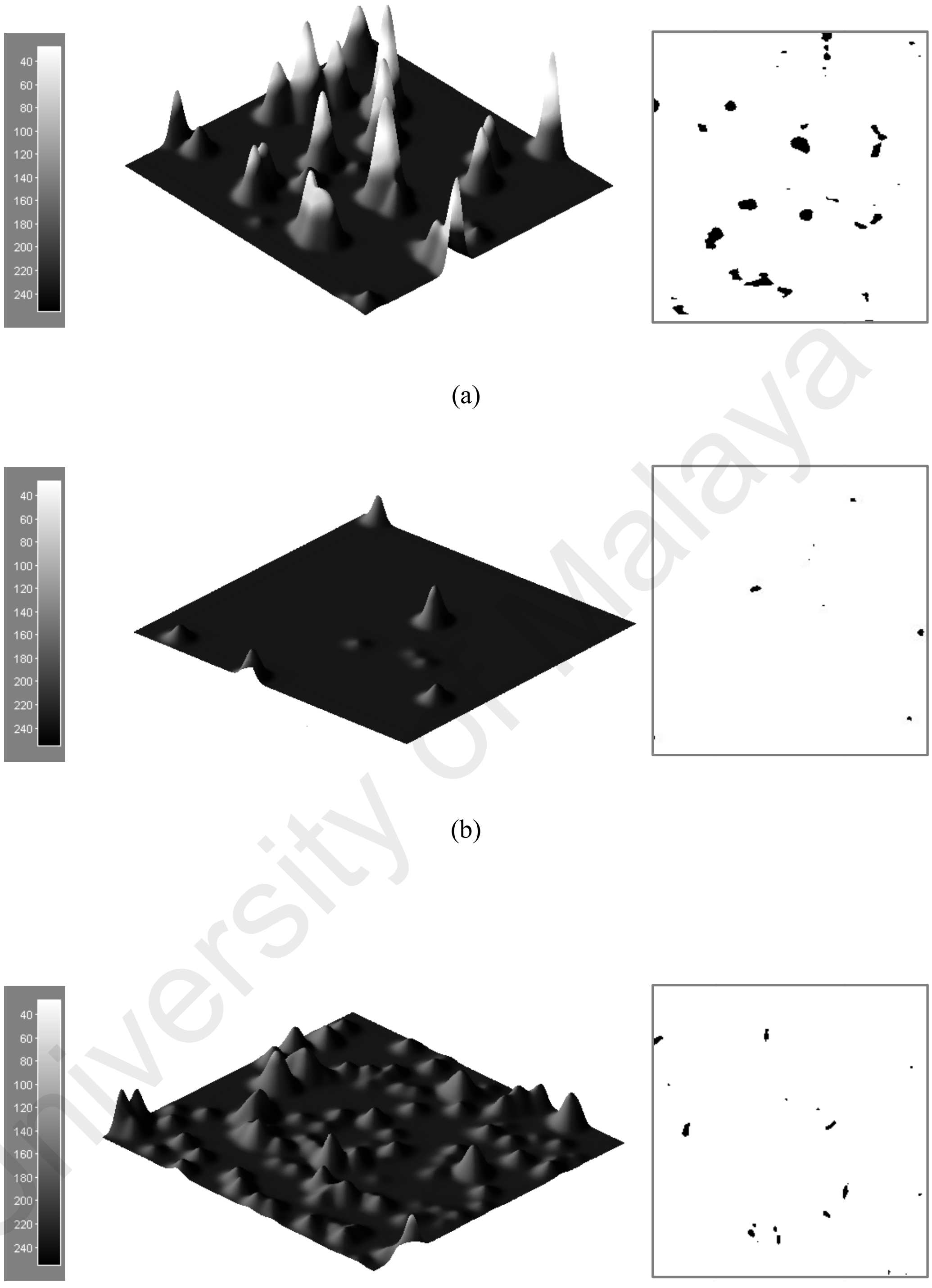

(a)

(b)

(c)

University of Malaya

Figure 4.15: Surface topology reconstructed from the gray level contour images at intensity of 170-255 pixels: (a) untreated pristine, (b) chloroform-treated, and (c) toluene-treated thin films. Faster rate of evaporation and aggregation of chloroform film, causing it to perform less granular counts as compared to the other two films.

Figure 4.16 shows the direct measurement of the photocurrent density from the IV graph for all thin films. On the other hand, photoluminescence (PL) is often used to represent charge transfer within the thin film. It indicates a better charge transfer across the interfaces when the intensity is decreasing. The quenching phenomenon was observed when the films were treated with different solvent. For second set of thin films, charge was transferred from the donor (NiTsPc) to the acceptor (Alq3).

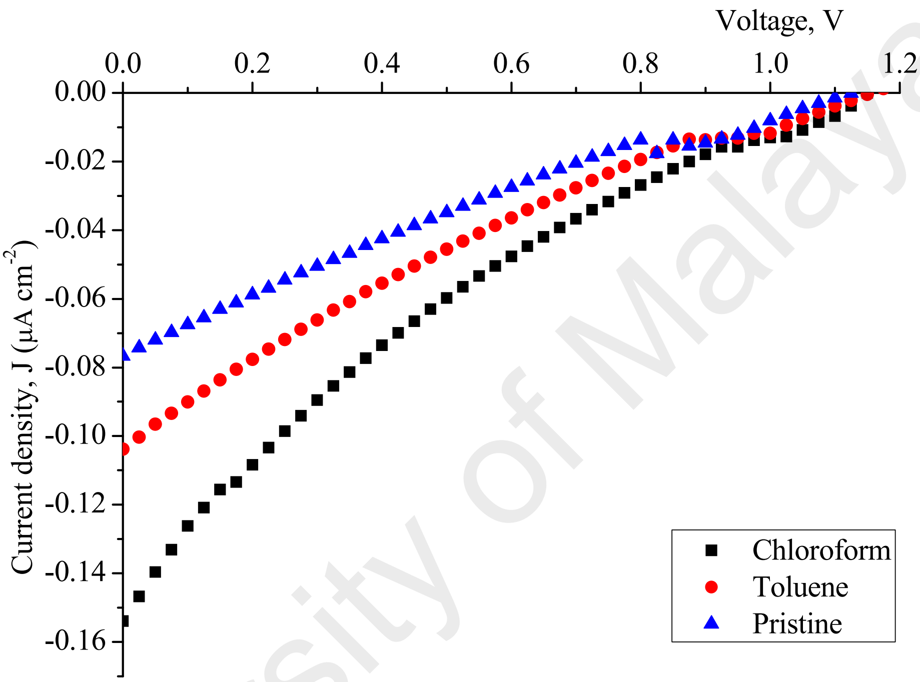

Figure 4.16: The current density – voltage (*J-V*) characteristics of ITO/NiTsPc/Alq3/Al and ITO/treated NiTsPc/Alq3/Al devices under light illumination.

As observed from the PL graph in Figure 4.17, the intensity of the toluene-treated and chloroform-treated films were decreased by ~21% and ~25%, respectively. While the untreated (pristine) film showed the highest peak intensity as compared to the other two. The detailed PL properties and IV results for both sets of thin films have been described and explained in (Fakir, 2013). The fractal dimension of the fibrous component and the photocurrent density are expected to be higher when the intensity is decreasing.

University of Malaya

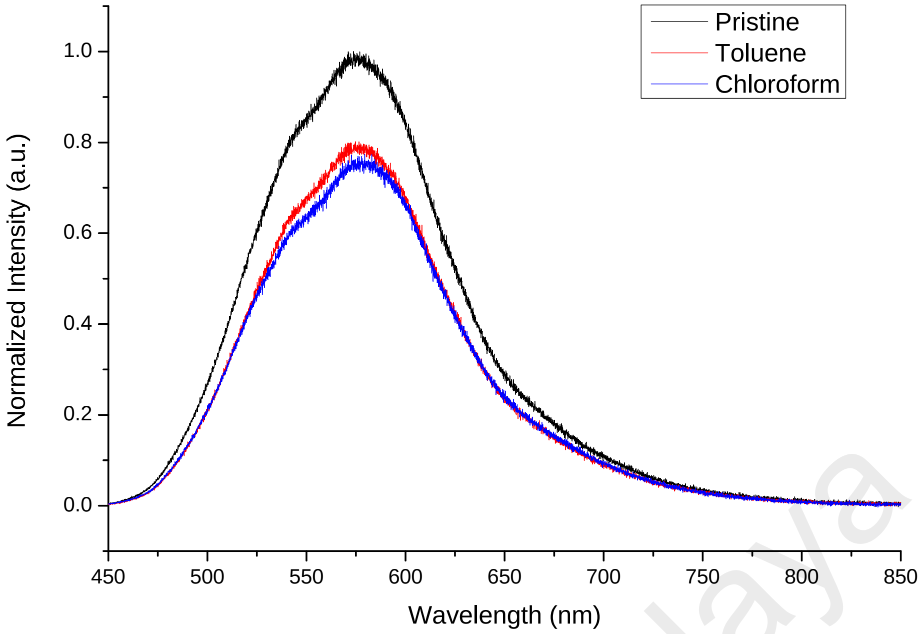

Figure 4.17: Photoluminescence (PL) properties of the untreated and treated NiTsPc incorporated with Alq3(NiTsPc/Alq3).

We have demonstrated that surface morphological analysis of disordered organic semiconductor required multiple approaches in order to extract useful information. While the power spectral analysis may be simpler to be interpreted when there exist ordered structures, the presence of complex multiscale morphological features would be reflected from the scaling power-law scaling behavior of PSD plots. This information is further analyzed by using the dual parameter model namely the generalized Cauchy process (GCP) that provides the fractal dimension and long range correlation properties of the microstructures. The local regularity of thin films and the space-filling of the micro fibers are described by the fractal dimensions obtained from the GCP method and the grayscale fractal dimension spectrum, respectively. It is noticed that the formation of the elongated microfibers is controlled by types of solvent used. Surface morphology with higher fractal dimension may account for significant increase in the exciton generation at the interface layer.

University of Malaya

CHAPTER 5: DISCUSSION AND CONCLUSION

5.1 Summary of Results

To summarize this work, the calculation of fractal dimensions and other transport related parameters from PSD and GCP are useful as quantitative morphological and developmental descriptors on thin films. PSD approach involves the transformation of spatial microstructure data into spectral domain, where patterns are to be interpreted in terms of harmonics/wavevectors. Thus, localized features in *x*-*y* space will be distributed over wide range of harmonics.

On the other hand, correlation or variogram analysis allows the spatial features to be analyzed as the way they are perceived by human vision, particularly the textures and the two-point image pixel correlation. Moreover, GCP incorporates the rms roughness measure through the fractal dimension determined from the local growth scaling behavior of the semi-variogram when $h \rightarrow 0$.

To conclude the comparison between GCP and PSD approaches, the potential application of dual parameter stochastic surface model, namely the generalized Cauchy process has been demonstrated for describing complex surface morphologies. Conventional approaches such as the spatial indicator based on root mean squared of height fluctuation or the Fourier based power spectral density provides limited information on localized features. The generalized Cauchy process on the other hand, provides dual description of fractal and long-range correlation properties simultaneously.

In this study, the local regularity of the thin films is characterized by the fractal dimension, which is shown to corroborate well with the findings based on direct measurement of the surface roughness from the AFM. The fractal dimension is

University of Malaya

relatively higher when the surface is rougher. It is noticed that smoother thin films contributes to lower production of photocurrent density.

As a conclusion, this study has demonstrated that the fractal analysis is competent to quantify the geometry of connectivity for disordered microstructure and the usefulness of generalized Cauchy process (GCP) model to provide further information of texture heterogeneity and its accurate connection to charge mobility based on dual description of fractal and long-range correlation properties. Higher electric conductivity is observed for thin films with higher fractal dimension but also enhanced when there exists spatially correlated morphologies in the form of network enhances charge transport at interfaces. The latter remark is justified using the correlation parameter $\beta < 1$ obtained from the GCP model. The correlation exponent β changes with increase of surface roughness, which suggests that a larger β has a smaller fractional dimension and thus a smoother surface, as proven by this study.

At the same time, the local regularity of thin films and the coverage of micro fibers are described by the fractal spectrum to optimize the characterization of fractal dimension. It is noticed that the formation of the elongated micro fibers is controlled by types of solvent used and the total solvent treatment duration. In both analysis, a surface morphology with higher fractal dimension is demonstrating a significant increase in the exciton generation at the interface layer. Thus, the second objective of this study to relate fractal parameters to carrier transport properties has been achieved.

In this study, the calculation of fractal dimensions seem to be very useful as quantitative morphological and developmental descriptors on thin films. However, the understanding of the drawbacks of the approaches is important in order to achieve higher accuracy of the fractal parameters estimation. As mentioned earlier, conventional approaches such as the spatial indicator based on root mean squared of height fluctuation or the Fourier based power spectral density provides limited information on

University of Malaya

localized features. The accuracy of PSD functions depends on the scan length, sampling distance and the measurement artifacts of the AFM measurements that provides limited range of spatial frequencies for the roughness values. To resolve these limitations, the measurement should be done by selecting a few cropped sections at different spatial frequency ranges from the same image, which are partially overlapping each other. For example, in this work, five sampling images of same size (400 × 400 pixels) have been selected from each parent image and processed for PSD functions separately. The results are then combined and averaged for higher accuracy.

Box counting method is limited by its bound of box size. The sample image is limited to scan size of $M \times M$ only, with pixels of $2^m \times 2^n$. Computing the fractal dimension of a sample image with arbitrary scan size of $M \times N$ by using box counting method will give rise to inaccurate estimation. There are plenty of works have suggested improved methods to resolve this problem (Hong et al., 2014; Li et al., 2009; Liu et al., 2014).

There are a few important factors that should be considered for getting high accuracy of empirical variogram, such as sample image size, lag range, and bin interval. A bigger sample image size contributes more sampling data on variogram, which decreases the sampling interval. The prediction and estimation will be more precise if the sampling interval is smaller. The empirical variogram is possibly flat as if the sampling interval is larger than the correlation range, which leads to fail prediction. Moreover, lack of sampling data increases the difficulty in choosing the right model for reliable estimation.

Choosing the correct bin interval and lag distance are crucial too, in order to include the short-range or long-range variations for predictions. If the lag range is small and the bin interval is narrow, the empirical variogram performs 'noise' due to overload of estimation points. If the lag range and the bin interval increases, there will be lacking of

University of Malaya

estimation points on the empirical variogram. Therefore, the selection of suitable lag range and bin width is particularly important and should be sensibly judged.

As a conclusion, the initial objectives of this research work have been achieved. The geometrical features of microstructure morphologies in disordered organics solar cell has been successfully studied by using fractal methods. The device performance based on microstructure morphological features has been quantified by relating the fractal dimension to the photocurrent density that produced under different experimental conditions.

5.2 Limitation of Study

The percolation theory can be applied to the analysis of carrier mobility in an organic material (Vakhshouri et al., 2013), but the significant influence of a fractal-percolative network that affects the carrier transport in an organic thin film need to be further discussed (Grover et al., 2012).

In spite of the fact that many have studied the Einstein's diffusion coefficients (Grassberger, 1999; Matsutani et al., 2012) on the charge diffusion phenomenon in the active layer to calculate the photocurrent, J_{sc}, with the known parameters such as diffusivity, D_n, and the electron concentration, Δn (Sze, 1985). However, there are still lack of study to relate efficiently the topology geometry of the active layer with the percolating systems to predict precisely the amount of photocurrent that have an clear effect on the comprehensive conductivity of a photovoltaic cell.

5.3 Future Work

Further work can be carried out to determine the percolation threshold of the system by using Fourier-analyzed method to resolve Random Resistor Network (RRN), that diametrically quantified the transport exponent for the active layer. In many study, the

University of Malaya

RRN method remains to be the most qualitative and effective approach to characterize the randomness of internal topology of a composite with higher precision (Kalnaus et al., 2011). It suggested that there is profound connection between the probability distribution of random walks and the nodes voltages on disordered network. In other words, a spatial disorder resistor network has current-carrying properties. RRN method has been extensively used to resolve the complex disordered network with irregular microstructure pattern through reliable models such as Monte Carlo model (Laosiritaworn, 2009), Direct Matrix Solution, Potts Model, Fourier Transform (Redner, n.d.), and Effective Medium Theory (EMT) (Schlicht & Ilgenfritz, 1996). For example, this popular RRN model is analyzed for arbitrary dimension of the lattice, $I_i = \sum_j g_{ij}(V_i - V_j)$, where g_{ij} is the conductance of link ij, and the sum runs over all links ij. This equation states that the current flowing into a node by an external current source equals the current flowing out of the node along the adjoining resistors.

As mentioned before, above percolation criticality, the propagation of the charge carriers across the module is fast and in tremendous amount. At this stage, the interconnected clusters form a continuous percolating path with chemical distance, l which is separated by geometrical distance, r. The chemical distance, l, reveals the length of the shortest path between two sites of cluster for transporting electrons, while the geometrical distance represents the displacement corresponding to the starting and the ending points of hopping. In some cases there is possibility to have more than one chemical path, which consisted of percolative bonds carrying the electric current, often referred as elastic backbone of the cluster. For future work, the current approach can be extended to study other types of organic materials and the computation of the percolation transport exponent, chemical length, geometrical distance and the precise hopping length should be investigated to describe the mechanical properties of an active layer.

University of Malaya

REFERENCES

Aarão Reis, F. D. A. (2006). Roughness fluctuations, roughness exponents and the universality class of ballistic deposition. *Physica A: Statistical Mechanics and Its Applications*, *364*, 190–196.

Ayres, C., Bowlin, G. L., Henderson, S. C., Taylor, L., Shultz, J., Alexander, J., Simpson, D. G. (2006). Modulation of anisotropy in electrospun tissue-engineering scaffolds: Analysis of fiber alignment by the fast Fourier transform. *Biomaterials*, *27*(32), 5524–34.

Azzarello, E., Mugnai, S., Pandolfi, C., Masi, E., Marone, E., & Mancuso, S. (2009). Comparing image (fractal analysis) and electrochemical (impedance spectroscopy and electrolyte leakage) techniques for the assessment of the freezing tolerance in olive. *Trees - Structure and Function*, *23*(1), 159–167.

Bagde, M.N., Raina, A. K., Chakraborty, A. K., & Jethwa, J. L. (2002). Rock mass characterization by fractal dimension. *Engineering Geology*, *63*(1-2), 141–155.

Balaguer-Beser, A., Ruiz, L. A., Hermosilla, T., & Recio, J. A. (2013). Using semivariogram indices to analyse heterogeneity in spatial patterns in remotely sensed images. *Computers & Geosciences*, *50*, 115–127.

Barnes, R. (2012). Variogram tutorial. Golden Software Inc. Retrieved from http://www.goldensoftware.com/variogramTutorial.pdf/

Ben Dkhil, S., Bourguiga, R., Davenas, J., & Cornu, D. (2012). Silicon nanowires in polymer nanocomposites for photovoltaic hybrid thin films. *Materials Chemistry and Physics*, *132*(2-3), 284–291.

Bharathi Mohan, D., & Sunandana, C. S. (2013). Optical studies of structurally disordered Ag(Sn)I thin films. *Thin Solid Films*, *534*, 192–197.

Biancolini, M. E., Brutti, C., Paparo, G., & Zanini, A. (2006). Fatigue cracks nucleation on steel, acoustic emission and fractal analysis. *International Journal of Fatigue*, *28*(12), 1820–1825.

Blakesley, J. C., Keivanidis, P. E., Campoy-Quiles, M., Newman, C. R., Jin, Y., Speller, R., Stavrinou, P. (2007). Organic semiconductor devices for X-ray imaging. *Nuclear Instruments and Methods in Physics Research Section A: Accelerators, Spectrometers, Detectors and Associated Equipment*, *580*(1), 774–777.

Bojović, B., Miljković, Z., & Babić, B. (2008). Fractal analysis of AFM images of worn-out contact lens inner surface. *FME Transactions*, *36*, 175–180.

Brinker, C. J., & Dunphy, D. R. (2006). Morphological control of surfactant-templated metal oxide films. *Current Opinion in Colloid & Interface Science*, *11*(2-3), 126–132.

Buchko, C. J., Kozloff, K. M., & Martin, D. C. (2001). Surface characterization of porous, biocompatible protein polymer thin films. *Biomaterials*, *22*(11), 1289–1300.

University of Malaya

Buczkowski, S., Hildgen, P., & Cartilier, L. (1998). Measurements of fractal dimension by box-counting: A critical analysis of data scatter. *Physica A: Statistical Mechanics and Its Applications*, *252*(1-2), 23–34.

Bui, V. T., Lee, H. S., Choi, J. H., & Choi, H. S. (2015). Highly ordered and robust honeycomb films with tunable pore sizes fabricated via UV crosslinking after applying improved phase separation. *Polymer*, *74*, 46–53.

Bunde, A., & Dieterich, W. (2000). Percolation in composites. *Journal of Electroceramics, 5*(2), 81–92.

Cabrera-Tobar, A., Bullich-Massagué, E., Aragüés-Peñalba, M., & Gomis-Bellmunt, O. (2016). Topologies for large scale photovoltaic power plants. *Renewable and Sustainable Energy Reviews*, *59*, 309–319.

Cen, W., Liu, D., & Mao, B. (2012). Conductivity exponent in three-dimensional percolation by diffusion based on molecular trajectory algorithm and blind-ant rules. *Physica A: Statistical Mechanics and Its Applications*, *391*(5), 1909–1918.

Cheng, J., Zhao, M., Yuan, X., Zhao, L., Huang, D., & Zhou, S. (2004). The percolation properties of fractal aggregation. *Physica A: Statistical Mechanics and Its Applications*, *343*, 335–342.

Dalla Rosa, J., Cooper, M., Darboux, F., & Medeiros, J. C. (2012). Soil roughness evolution in different tillage systems under simulated rainfall using a semivariogram-based index. *Soil and Tillage Research*, *124*, 226–232.

Dang, M.T., Hirsch, L., Wantz, G., Wuest, J.D. (2013). Controlling the morphology and performance of bulk heterojunctions in solar cells. *Chemical Reviews, 113*(5) 3734–3765.

Dani, A., & Ogale, A. A. (1997). Percolation in short-fiber composites: Cluster statistics and critical exponents. *Composites Science and Technology*, *57*(9-10), 1355–1361.

Dani, A., & Ogale, A. A. (1996). Electrical percolation behavior of short-fiber composites: Experimental characterization and modelling. *Composites Science and Technology*, *56*, 911–920.

Dash, P., Mallick, P., Rath, H., Tripathi, a., Prakash, J., Avasthi, D. K., Mishra, N. C. (2009). Surface roughness and power spectral density study of SHI irradiated ultra-thin gold films. *Applied Surface Science*, *256*(2), 558–561.

Domenici, F., Fasolato, C., Mazzi, E., De Angelis, L., Brasili, F., Mura, F., Bordi, F. (2016). Engineering microscale two-dimensional gold nanoparticle cluster arrays for advanced Raman sensing: An AFM study. *Colloids and Surfaces A: Physicochemical and Engineering Aspects*, *498*, 168–175.

Dougherty, G., & Henebry, G. M. (2002). Lacunarity analysis of spatial pattern in CT images of vertebral trabecular bone for assessing osteoporosis. *Medical Engineering & Physics*, *24*(2), 129–38.

University of Malaya

Erickson, N. C., & Holmes, R. J. (2010). Highly efficient, single-layer organic light-emitting devices based on a graded-composition emissive layer. *Applied Physics Letters*, *97*(8), 083308.

Evans, D. R., Kwak, H. S., Giesen, D. J., Goldberg, A., Halls, M. D., & Oh-E, M. (2016). Estimation of charge carrier mobility in amorphous organic materials using percolation corrected random-walk model. *Organic Electronics: Physics, Materials, Applications*, *29*, 50–56.

Fakir, M. S. (2013). Preparation and characterization of nickel (II) phthalocyanine tetrasulfonic acid tetrasodium salt for organic solar cells (Master dissertation). University of Malaya, Malaysia.

Fares, B., Dubois, C., Gautier, B., Dupuy, J. C., Cayrel, F., & Gaudin, G. (2006). AFM study of the SIMS beam induced roughness in monocrystalline silicon in presence of initial surface or bulk defects of nanometric size. *Applied Surface Science*, *252*(19), 6448–6451.

Filby, A., Plaschke, M., & Geckeis, H. (2012). AFM force spectroscopy study of carboxylated latex colloids interacting with mineral surfaces. *Colloids and Surfaces A: Physicochemical and Engineering Aspects*, *414*, 400–414.

Florindo, J. B., & Bruno, O. M. (2012). Fractal descriptors based on Fourier spectrum applied to texture analysis. *Physica A: Statistical Mechanics and Its Applications*, *391*(20), 4909–4922.

Freitas, J. N. De, Korala, L., Reynolds, L. X., Haque, S. A., & Brock, S. L. (2012). Electronic supplementary information connecting the (quantum) dots: Towards hybrid photovoltaic devices based on chalcogenide gels. *Physical Chemistry Chemical Physics*, *14*(43), 15180–15184.

Friedrichs, J., Taubenberger, A., Franz, C. M., & Muller, D. J. (2007). Cellular remodelling of individual collagen fibrils visualized by time-lapse AFM. *Journal of Molecular Biology*, *372*(3), 594–607.

Furustig, J., Dobryden, I., Almqvist, A., Almqvist, N., & Larsson, R. (2016). The measurement of wear using AFM and wear interpretation using a contact mechanics coupled wear model. *Wear*, *350-351*, 74–81.

Galdikas, A. (2008). Study of nanoclusters growth at initial stages of ultrathin film deposition by kinetic modelling. *Applied Surface Science*, *254*(13), 3964–3970.

Garcia-Belmonte, G. (2003). Effect of electrode morphology on the diffusion length of the doping process of electronically conducting polypyrrole films. *Electrochemistry Communications*, *5*(3), 236–240.

Gavrila, R., Dinescu, A., & Mardare, D. (2007). A power spectral density study of thin films morphology based on AFM profiling. *Romanian Journal of Information Science and Technology*, *10*(3), 291–300.

Geest, A. G., Hurst, K. E., Bronstein, N. D., Lehman, J. H., & Lusk, M. T. (2010). Theoretical

University of Malaya

and experimental evidence of the role of electromagnetic resonance in the cleaning of nanotubes. *Physical Review, 81*(115440).

Gneiting, T., & Schlather, M. (2001). Stochastic models which separate fractal dimension and Hurst effect. *Society for Industrial and Applied Mathematics Review*, *46*(2), 269–282.

Goetz, S. M., Erlen, C. M., Grothe, H., Wolf, B., Lugli, P., & Scarpa, G. (2009). Organic field-effect transistors for biosensing applications. *Organic Electronics*, *10*(4), 573–580.

Grassberger, P. (1999). Conductivity exponent and backbone dimension in 2-d percolation. *Physica A: Statistical Mechanics and Its Applications*, *262*(3-4), 251–263.

Grover, R., Srivastava, R., Kamalasanan, M. N., & Mehta, D. S. (2012). Percolation dominated electron transport in Tetracyanoquinodimethane mixed 4,7-diphenyl-1,10-phenanthroline thin films. *Organic Electronics*, *13*(12), 3074–3078.

He, Z., Xiao, B., Liu, F., Wu, H., Yang, Y., Xiao, S., Cao, & Y. (2015). Single-junction polymer solar cells with high efficiency and photovoltage. *Nature Photonics*, *9*, 174–179.

Hong, D., Pan, Z., & Wu, X. (2014). Improved differential box counting with multi-scale and multi-direction: A new palmprint recognition method. *Optik - International Journal for Light and Electron Optics*, *125*(15), 4154–4160.

Hoppe, H. (2004). Efficiency relationship in organic bulk heterojunction plastic solar cells (Doctor dissertation). University Johannes Kepler Linz, Austria.

Huang, C. P., Chaparro, L. F., & Vallejo, L. E. (1997). Fractal dimension of profiles and surfaces using fuzzy morphological coverings. *Engineering Geology*, *48*(3-4), 245–253.

Hunt, A. G. (2001). Applications of percolation theory to porous media with distributed local conductances. *Advances in Water Resources*, *24*(3-4), 279–307.

Itoh, T., & Yamauchi, N. (2007). Surface morphology characterization of pentacene thin film and its substrate with under-layers by power spectral density using fast Fourier transform algorithms. *Applied Surface Science*, *253*(14), 6196–6202.

Jakobsson, F., Crispin, X., & Berggren, M. (2009). Prediction of the current versus voltage behavior of devices based on organic semiconductor guest–host systems. *Organic Electronics*, *10*(1), 95–106.

Jayalalitha, G., & Uthayakumar, R. (2009). Recognition of Cervical Cancer Based on Fractal Dimension. *2009 International Conference on Advances in Recent Technologies in Communication and Computing*, 532–536.

Jeong, E. G., Han, Y. C., Im, H. G., Bae, B. S., & Choi, K. C. (2016). Highly reliable hybrid nano-stratified moisture barrier for encapsulating flexible OLEDs. *Organic Electronics*, *33*, 150–155.

Jung, B., Kim, K., Kim, J., Kim, S., Kim, E., & Kim, W. (2014). Inter-diffused ordered bulk

University of Malaya

heterojunction organic photovoltaics: optimized morphology for efficient exciton dissociation and charge transport. *Solar Energy Materials and Solar Cells*, *120*, 675–684.

Kalnaus, S., Sabau, A. S., Newman, S., Tenhaeff, W. E., Daniel, C., & Dudney, N. J. (2011). Effective conductivity of particulate polymer composite electrolytes using random resistor network method. *Solid State Ionics*, *199-200*, 44–53.

Kalpakjian, S., Schmid, S. (2008). *Manufacturing Processes for Engineering Materials* (5th ed.). Pearson Education. Retrieved from https://www3.nd.edu/

Karan, S., & Mallik, B. (2008). Power spectral density analysis and photoconducting behavior in copper(II) phthalocyanine nanostructured thin films. *Physical Chemistry Chemical Physics : PCCP*, *10*(45), 6751–61.

Kardar, M., Parisi, G. (1989). Dynamic scaling of growing interfaces. *Physical Review Letters*, *56*(9), 889–892.

Karoussi, O., Skovbjerg, L. L., Hassenkam, T., Stipp, S. L. S., & Hamouda, A. A. (2008). AFM study of calcite surface exposed to stearic and heptanoic acids. *Colloids and Surfaces A: Physicochemical and Engineering Aspects*, *325*(3), 107–114.

Kasap, S., and Capper, P. (2006). *Molecular Electronics*. *Springer Handbook of Electronics and Photonic Materials*. New York, NY: Springer Science.

Kerry, R., & Oliver, M. a. (2011). Soil geomorphology: Identifying relations between the scale of spatial variation and soil processes using the variogram. *Geomorphology*, *130*(1-2), 40–54.

King, P. R., Buldyrev, S. V, Dokholyan, N. V, & Havlin, S. (2002). Using percolation theory to predict oil field performance, *Physica A, 314*, 103–108.

Kong, Y. L., Muniandy, S. V., Fakir, M. S., & Sulaiman, K. (2014). Morphological image interpretation of organic nickel(II) phthalocyanine-tetrasulfonic acid tetrasodium film using fractal analysis. *Applied Surface Science*, *301*, 363–368.

Kulesza, S., & Bramowicz, M. (2014). A comparative study of correlation methods for determination of fractal parameters in surface characterization. *Applied Surface Science*, *293*, 196–201.

Kumaresan, P., Vegiraju, S., Ezhumalai, Y., Yau, S. L., Kim, C., Lee, W. H., & Chen, M. C. (2014). Fused-thiophene based materials for organic photovoltaics and dye-sensitized solar cells. *Polymers, 6*(10), 2645–2669.

Kwan, S. J. (2012). Development of erosion fractal-based interpolation method of river morphology. *Journal of the Korean Water Resources Association*, *45*(9), 943–957.

Kwon, W., & Rhee, S. W. (2011). High performance quasi-solid-state dye-sensitized solar cells based on poly(lactic acid-co-glycolic acid). *Journal of Power Sources*, *196*(23), 10532–10537.

University of Malaya

Laosiritaworn, Y. (2009). Monte Carlo simulation on thickness dependence of hysteresis properties in Ising thin-films. *Thin Solid Films*, *517*(17), 5189–5191.

Lazouskaya, V., Jin, Y., & Or, D. (2006). Interfacial interactions and colloid retention under steady flows in a capillary channel. *Journal of Colloid and Interface Science*, *303*(1), 171–84.

Lee, C. K., & Lee, S. L. (1995). Effects of the heterogeneous surface geometry on the selectivity behavior of a multi-step reaction. *Surface Science*, *339*(1-2), 171–181.

Lee, L. H., Tambasco, M., Otsuka, S., Wright, A., Klimowicz, A., Petrillo, S., Bebb, D. G. (2014). Digital differentiation of non-small cell carcinomas of the lung by the fractal dimension of their epithelial architecture. *Micron*, *67*, 125–131.

Leuenberger, H., & Ineichen, L. (1997). Percolation theory and physics of compression. *European Journal of Pharmaceutics and Biopharmaceutics, 44*, 269–272.

Li, C., Duan, L., Li, H., & Qiu, Y. (2013). Percolative charge transport in a co-evaporated organic molecular mixture. *Organic Electronics*, *14*(12), 3312–3317.

Li, G., Yao, Y., Yang, H., Shrotriya, V., Yang, G., Yang, Y. (2007). "Solvent annealing" effect in polymer solar cells based on poly(3-hexylthiophene) and methanofullerenes. *Advanced Functional Materials*, *17*, 1636-1644.

Li, J., Du, Q., & Sun, C. (2009). An improved box-counting method for image fractal dimension estimation. *Pattern Recognition*, *42*(11), 2460–2469.

Liu, Y., Chen, L., Wang, H., Jiang, L., Zhang, Y., Zhao, J., Song, Y. (2014). An improved differential box-counting method to estimate fractal dimensions of gray-level images. *Journal of Visual Communication and Image Representation*, *25*(5), 1102–1111.

Long, M., & Peng, F. (2013). A box-counting method with adaptable box height for measuring the fractal feature of images. *Radioengineering*, *22*(1), 208–213.

Lopes, R., & Betrouni, N. (2009). Fractal and multifractal analysis: A review. *Medical Image Analysis*, *13*(4), 634–49.

Louise Meyer, R., Zhou, X., Tang, L., Arpanaei, A., Kingshott, P., & Besenbacher, F. (2010). Immobilisation of living bacteria for AFM imaging under physiological conditions. *Ultramicroscopy*, *110*(11), 1349–1357.

Maldonado, F., & Stashans, A. (2016). DFT modelling of hydrogen sulphide adsorption on α-Cr2O3 (0001) surface. *Surface Science*, *647*, 78–83.

Malek, M. F., Sahdan, M. Z., Mamat, M. H., Musa, M. Z., Khusaimi, Z., Husairi, S. S., Rusop, M. (2013). A novel fabrication of MEH-PPV/Al:ZnO nanorod arrays based ordered bulk heterojunction hybrid solar cells. *Applied Surface Science*, *275*, 75–83.

Mandelbrot, B. B. (1982). The Fractal Geometry of Nature. *Freeman, San Francisco, CA*.

University of Malaya

Mandelbrot, B. B. (1967). How long is the coast of Britain? Statistical self-similarity and fractional dimension. *Science, 156,* 636–638.

Manor, A., Katz, E. a., Tromholt, T., Hirsch, B., & Krebs, F. C. (2011). Origin of size effect on efficiency of organic photovoltaics. *Journal of Applied Physics*, *109*(074508), 1–9.

Mashiah, A., Wolach, O., Sandbank, J., Uziel, O., Raanani, P., & Lahav, M. (2008). Lymphoma and leukemia cells possess fractal dimensions that correlate with their biological features. *Acta Haematologica*, *119*(3), 142–50.

Matsutani, S., Shimosako, Y., & Wang, Y. (2012). Fractal structure of equipotential curves on a continuum percolation model. *Physica A: Statistical Mechanics and Its Applications*, *391*(23), 5802–5809.

Mendez-Vilas, A., Bruque, J. M., & Gonzalez-Martin, M. L. (2007). Sensitivity of surface roughness parameters to changes in the density of scanning points in multi-scale AFM studies. Application to a biomaterial surface. *Ultramicroscopy*, *107*(8), 617–625.

Meyer, S., Blaschek, M., Duttmann, R., & Ludwig, R. (2015). Improved hydrological model parametrization for climate change impact assessment under data scarcity: The potential of field monitoring techniques and geostatistics. *Science of The Total Environment, 543,* 906-923.

Monemdjou, A., Ghodsi, F. E., & Mazloom, J. (2014). The effects of surface morphology on optical and electrical properties of nanostructured AZO thin films: Fractal and phase imaging analysis. *Superlattices and Microstructures*, *74*, 19–33.

Moulé, A. J. (2010). Power from plastic. *Current Opinion in Solid State and Materials Science*, *14*(6), 123–130.

Muniandy, S. V, & Stanslas, J. (2008). Modelling of chromatin morphologies in breast cancer cells undergoing apoptosis using generalized Cauchy field. *Computerized Medical Imaging and Graphics : The Official Journal of the Computerized Medical Imaging Society*, *32*(7), 631–7.

Norton, J. E. (2009). Molecular understanding of organic solar cells: Introduction. *Accounts of Chemical Research*, *42*(11), 1691–1699.

Oliver, M. a., & Webster, R. (2014). A tutorial guide to geostatistics: Computing and modelling variograms and kriging. *Catena*, *113*, 56–69.

Oyarzún, D. P., Linarez Pérez, O. E., López Teijelo, M., Zúñiga, C., Jeraldo, E., Geraldo, D. A., & Arratia-Perez, R. (2016). Atomic force microscopy (AFM) and 3D confocal microscopy as alternative techniques for the morphological characterization of anodic TiO_2 nanoporous layers. *Materials Letters*, *165*, 67–70.

Paiva, T., & Aarão Reis, F. D. A. (2007). Height and roughness distributions in thin films with Kardar-Parisi-Zhang scaling. *Surface Science*, *601*(2), 419–424.

University of Malaya

Pea, M., Maiolo, L., Giovine, E., Rinaldi, A., Araneo, R., & Notargiacomo, A. (2016). Electrical characterization of FIB processed metal layers for reliable conductive-AFM on ZnO microstructures. *Applied Surface Science*, *371*, 83–90.

Qian, X., Wang, T., & Yan, D. (2013). Transparent organic thin-film transistors based on high quality polycrystalline rubrene film as active layers. *Organic Electronics*, *14*(4), 1052–1056.

Raguso, G., Ancona, A., Chieppa, L., L'abbate, S., Pepe, M. L., Mangieri, F., Rangayyan, R. M. (2010). Application of fractal analysis to mammography. *Annual International Conference of the IEEE Engineering in Medicine and Biology Society. IEEE Engineering in Medicine and Biology Society. Conference*, *2010*, 3182–5.

Rangayyan, R. M., Oloumi, F., & Nguyen, T. M. (2010). Fractal analysis of contours of breast masses in mammograms via the power spectra of their signatures. *Annual International Conference of the IEEE Engineering in Medicine and Biology Society. IEEE Engineering in Medicine and Biology Society. Conference*, *2010*, 6737–40.

Rao, P., Schiff, E., Tsybeskov, L., & Fauchet, P. (2002). Photocarrier drift-mobility measurements and electron localization in nanoporous silicon. *Chemical Physics*, *284*(1-2), 129–138.

Raoufi, D. (2010). Fractal analyses of ITO thin films: A study based on power spectral density. *Physica B: Condensed Matter*, *405*(1), 451–455.

Raoufi, D., Kiasatpour, A., Fallah, H. R., & Rozatian, A. S. H. (2007). Surface characterization and microstructure of ITO thin films at different annealing temperatures. *Applied Surface Science*, *253*(23), 9085–9090.

Redner, S. (2007). Fractal and Multifractal Scaling of Electrical Conduction in Random Resistor Networks Definition of the Subject. Boston University, USA.

Rinaldo, A., Rodriguez-Iturbe, I., Rigon, R., Ijjasz-Vasquez, E., & Bras, R. L. (1993). Self-organized fractal river networks. *Physical Review Letters*, *70*(6), 822–825.

Roko, R. O., Daemen, J. J. K., & Myers, D. E. (1997). Variogram characterization of joint surface morphology and asperity deformation during shearing. *International Journal of Rock Mechanics and Mining Sciences*, *34*(1), 71–84.

Ruderer, M. A., & Müller-Buschbaum, P. (2011). Morphology of polymer-based bulk heterojunction films for organic photovoltaics. *Soft Matter*, *7*(12), 5482.

Sadeghi, B., Madani, N., & Carranza, E. J. M. (2015). Combination of geostatistical simulation and fractal modelling for mineral resource classification. *Journal of Geochemical Exploration*, *149*, 59–73.

Sahoo, N. K., Thakur, S., & Tokas, R. B. (2006). Fractals and superstructures in gadolinia thin film morphology: Influence of process variables on their characteristic parameters. *Thin Solid Films*, *503*(1-2), 85–95.

University of Malaya

Schlicht, L., & Ilgenfritz, G. (1996). Simulation of diffusion in 2D heterogeneous systems: Comparison with effective medium and percolation theories. *Physica A*, *227*, 239–247.

Schroeder, M. (1992). *Fractals, Chaos, Power Laws: Minutes from an Infinite Paradise*. New York, NY: W. H. Freeman and Company.

Senthilkumar, M., Sahoo, N. K., Thakur, S., & Tokas, R. B. (2005). Characterization of microroughness parameters in gadolinium oxide thin films: A study based on extended power spectral density analyses. *Applied Surface Science*, *252*(5), 1608–1619.

Sergeyev, Y. D. (2016). The exact (up to infinitesimals) infinite perimeter of the Koch snowflake and its finite area. *Communications in Nonlinear Science and Numerical Simulation*, *31*(1-3), 21–29.

Servaites, J. D., Ratner, M. a., & Marks, T. J. (2011). Organic solar cells: A new look at traditional models. *Energy & Environmental Science*, *4*(11), 4410–4422.

Sheng, X., Daems, N., Geboes, B., Kurttepeli, M., Bals, S., Breugelmans, T., Pescarmona, P. P. (2015). N-doped ordered mesoporous carbons prepared by a two-step nanocasting strategy as highly active and selective electrocatalysts for the reduction of O2 to H2O2. *Applied Catalysis B: Environmental*, *176-177*, 212–224.

Siegmund, C., & Leuenberger, H. (1999). Percolation theory, conductivity and dissolution of hydrophilic suppository bases (PEG systems). *International Journal of Pharmaceutics*, *189*(2), 187–96.

Simonetti, O., Giraudet, L., & Bugnot, D. (2014). Effective mobility in amorphous organic transistors: Influence of the width of the density of states. *Organic Electronics: Physics, Materials, Applications*, *15*(1), 35–39.

Someya, T., Sekitani, T., Iba, S., Kato, Y., Kawaguchi, H., and Sakurai, T. (2004). A large-area, flexible pressure sensor matrix with organic field-effect transistors for artificial skin applications. *Proceedings of the National Academy of Sciences of the United States of America PNAS, 101* (27), 9966–9970.

Stam, C. J., & Reijneveld, J. C. (2007). Graph theoretical analysis of complex networks in the brain. *Nonlinear Biomedical Physics*, *1*(1), 3–21.

Stauffer, D., A. Aharony. (1994). *Introduction to Percolation Theory* (2nd ed.). Philadelphia, PA: Taylor & Francis Inc.

Švanda, J., Siegel, J., Švorčík, V., & Lyutakov, O. (2016). AFM study of excimer laser patterning of block-copolymer: Creation of ordered hierarchical, hybrid, or recessed structures. *Applied Surface Science*, *371*, 203–212.

Sze, S. M. (1985). *Semiconductor Devices, Physics and Technology* (2nd ed.). New York. NY: John Wiley & Sons, Inc.

Tada, K., Harada, H., Onoda, M., Nakayama, H., & Yoshino, K. (1999). Percolation in carrier

University of Malaya

transport in FET with dye doped conducting polymers. *Synthetic Metals*, *102*(1-3), 981.

Ţălu, Ş., Patra, N., & Salerno, M. (2015). Micromorphological characterization of polymer-oxide nanocomposite thin films by atomic force microscopy and fractal geometry analysis. *Progress in Organic Coatings*, *89*, 50–56.

Tambasco, M., Eliasziw, M., & Magliocco, A. M. (2010). Morphologic complexity of epithelial architecture for predicting invasive breast cancer survival. *Journal of Translational Medicine*, *8*(1), 140–157.

Timbó, C., da Rosa, L. a. R., Gonçalves, M., & Duarte, S. B. (2009). Computational cancer cells identification by fractal dimension analysis. *Computer Physics Communications*, *180*(6), 850–853.

Vakhshouri, K., Kesava, S. V., Kozub, D. R., & Gomez, E. D. (2013). Characterization of the mesoscopic structure in the photoactive layer of organic solar cells: A focused review. *Materials Letters*, *90*, 97–102.

Valencia-Lazcano, A. A., Alonso-Rasgado, T., & Bayat, A. (2013). Characterisation of breast implant surfaces and correlation with fibroblast adhesion. *Journal of the Mechanical Behavior of Biomedical Materials*, *21*, 133–148.

Vengadesh, P., Muniandy, S. V., & Majid, W. H. A. (2009). Fractal morphological analysis of Bacteriorhodopsin (bR) layers deposited onto indium tin oxide (ITO) electrodes. *Materials Science and Engineering C*, *29*(5), 1621–1626.

Vilmercati, P., Cvetko, D., Cossaro, A., & Morgante, A. (2009). Heterostructured organic interfaces probed by resonant photoemission. *Surface Science*, *603*(10-12), 1542–1556.

Viville, P., Thoelen, O., Beauvois, S., Lazzaroni, R., Lambin, G., Bredas, J. L., Laude, L. (1995). Thin films of polymer blends: Surface treatment and theoretical modelling. *Applied Surface Science*, *86*(1-4), 411–416.

Vogel, M., Strotmann, J., Johnev, B., Lux-Steiner, M. C., & Fostiropoulos, K. (2006). Influence of nanoscale morphology in small molecule organic solar cells. *Thin Solid Films*, *511-512*, 367–370.

Voss, S., Zimmermann, B., & Zimmermann, A. (2016). Detecting spatial structures in throughfall data: The effect of extent, sample size, sampling design, and variogram estimation method. *Journal of Hydrology*, *540*, 527–537.

Wang, D. C., Chen, K. Y., Tsai, C. H., Chen, G. Y., & Chen, C. H. (2011). AFM membrane roughness as a probe to identify oxidative stress-induced cellular apoptosis. *Journal of Biomechanics*, *44*(16), 2790–2794.

Wang, Y., & Xu, K. W. (2004). Characterization of surface morphology of copper tungsten thin film by surface fractal geometry and resistivity. *Thin Solid Films*, *468*(1-2), 310–315.

Wang, Z., Zhang, C., Gao, R., Chen, D., Tang, S., Zhang, J., Hao, Y. (2014). Improvement of

University of Malaya

transparent silver thin film anodes for organic solar cells with a decreased percolation threshold of silver. *Solar Energy Materials and Solar Cells*, *127*, 193–200.

Widmer, J., Fischer, J., Tress, W., Leo, K., & Riede, M. (2013). Electric potential mapping by thickness variation: A new method for model-free mobility determination in organic semiconductor thin films. *Organic Electronics*, *14*(12), 3460–3471.

Williams, S. S., Hampton, M. J., Gowrishankar, V., Ding, I. K., Templeton, J. L., Samulski, E. T., McGehee, M. D. (2008). Nanostructured titania-polymer photovoltaic devices made using PFPE-based nanomolding techniques. *Chemistry of Materials*, *20*(16), 5229–5234.

Xiong, J., Yang, B., Yuan, J., Fan, L., Hu, X., Xie, H., Yang, J. (2015). Efficient organic photovoltaics using solution-processed, annealing-free TiO_2 nanocrystalline particles as an interface modification layer. *Organic Electronics*, *17*, 253–261.

Xue, K., Chen, B., Han, G., Duan, Y., Chen, P., Yang, Y., Zhao, Y. (2015). Efficient simplified orange and white phosphorescent organic light-emitting devices with reduced efficiency roll-off. *Organic Electronics: Physics, Materials, Applications*, *22*, 122–126.

Yambem, S. D., Liao, K. S., & Curran, S. a. (2012). Enhancing current density using vertically oriented organic photovoltaics. *Solar Energy Materials and Solar Cells*, *101*, 227–231.

Yan, Y. D., Hu, Z. J., Liu, W. T., & Zhao, X. S. (2015). Effects of scratching parameters on fabrication of polymer nanostructures in atomic force microscope tapping mode. *Procedia CIRP*, *28*, 100–105.

Yang, C., Yi, Y., & Li, Y. R. (2010). Modelling and simulation of reaction mechanisms in early growth of STO thin films from ab initio calculations. *Computational Materials Science*, *49*(4), 845–849.

Yasuda, T., Kuwabara, J., Han, L., & Kanbara, T. (2015). Improved power conversion efficiency of bulk-heterojunction organic photovoltaic cells using neat C70 as an effective acceptor for an amorphous π-conjugated polymer. *Organic Electronics*, *25*, 99–104.

Yi, I., Nishi, R., Sugimoto, Y., & Morita, S. (2007). Non-contact AFM observation of the $(\sqrt{3}\times\sqrt{3})$ to (3×3) phase transition on Sn/Ge(111) and Sn/Si(111) surfaces. *Applied Surface Science*, *253*(6), 3072–3076.

Yimer, Y. Y., Bobbert, P. a., & Coehoorn, R. (2009). Charge transport in disordered organic host–guest systems: Effects of carrier density and electric field. *Synthetic Metals*, *159*(21–22), 2399–2401.

Yin, J., D'Haese, C., & Nysten, B. (2015). Surface electrical properties of stainless steel fibres: An AFM-based study. *Applied Surface Science*, *330*, 65–73.

Young, T.-F., & Fang, H.-J. (2000). DC conductive percolation of 2-D fractal random network. *Physica A: Statistical Mechanics and Its Applications*, *281*(1–4), 276–281.

Yu, J., & Tan, J. (2009). Object density-based image segmentation and its applications in

University of Malaya

biomedical image analysis. *Computer Methods and Programs in Biomedicine*, *96*(3), 193–204.

Zabat, M., Harba, R., & Damme, H. V. (2015). Fractal analysis of surface roughness of montmorillonite clay self-supported films: Effects of exchanged cations and of mechanical tensile stress. *Colloids and Surfaces A: Physicochemical and Engineering Aspects*, *486*, 38–44.

Zhang, J., & Liu, Z. (1998). Study of the relationship between fractal dimension and viscosity ratio for viscous fingering with a modified DLA model. *Journal of Petroleum Science and Engineering*, *21*(1-2), 123–128.

Zorzi, P. D., Barbizzi, S., Belli, M., Barbina, M., Fajgelj, A., Jacimovic, R., Van der Perk, M. (2008). Estimation of uncertainty arising from different soil sampling devices: The use of variogram parameters. *Chemosphere*, *70*(5), 745–752.

University of Malaya

LIST OF PUBLICATIONS

Journals *(ISI-Cited Publication)*

Y. L. Kong, S. V. Muniandy, M. S. Fakir, and K. Sulaiman (2014). Morphological image interpretation of organic nickel(II) phthalocyanine-tetrasulfonic acid tetrasodium film using fractal analysis. *Applied Surface Science, 301,* 363–368.

Y. L. Kong, S. V. Muniandy, K. Sulaiman and M. S. Fakir (2017). Random fractal surface analysis of disordered organic thin films. *Thin Solid Films, 623,* 147–156.

Proceedings *(ISI-Cited Publication)*

Y. L. Kong, S. V. Muniandy, M. S. Fakir, and K. Sulaiman (2014). Percolation Network Model for Studying Enhanced Carrier Transport in Organic Photovoltaic (OPV) Material. *Advanced Materials Research, 895,* 407-410.

Y. L. Kong, S. V. Muniandy, and K. Sulaiman (2015). Evaluation of Charge Transport In A Percolating Network of Disordered Organic Thin Films. *AIP Conference Proceedings, 1657,* 100001.

Proceedings

Y. L. Kong, S. V. Muniandy, M. S. Fakir, and K. Sulaiman (2013). Image Interpretation of Phthalocyanine Tetrasulfonic Acid Tetrasodium (TsNiPc) Thin Film Using Fractal Analysis. *Solar Energy Materials, Solar Cells & Solar Energy Applications*, 241-246.

University of Malaya